Dynamic modelling of platinum degradation in polymer electrolyte fuel cells

by

Heather A. Baroody

B.Sc., University of Colorado at Denver, 2011

Thesis Submitted in Partial Fulfillment of the
Requirements for the Degree of
Doctor of Philosophy

in the
Department of Chemistry
Faculty of Science

SIMON FRASER UNIVERSITY
Fall 2018

Approval

Name:	**Heather A. Baroody**
Degree:	**Doctor of Philosophy (Chemistry)**
Title:	**Dynamic modelling of platinum degradation in polymer electrolyte fuel cells**
Examining Committee:	**Chair:** Charles J. Walsby Associate Professor

Michael Eikerling
Senior Supervisor
Professor _____

Byron D. Gates
Supervisor
Associate Professor _____

Krzysztof Starosta
Supervisor
Associate Professor _____

Gary W. Leach
Internal Examiner
Professor _____

Viola I. Birss
External Examiner
Professor
Department of Chemistry
University of Calgary _____

Date Defended: **December 10, 2018**

Abstract

Platinum stability in the catalyst layer is vital to the lifetime of polymer electrolyte fuel cells. This thesis uses physical-mathematical modelling to provide a deeper understanding of platinum degradation. Dissolution, a dominant degradation mechanism under fuel cell operating conditions, is shown to be strongly linked to oxide formation, growth, and reduction. However, since a consistent model that explains this link does not exist, the goal is to understand the platinum oxide processes and relate these to platinum degradation.

In the first part, a physical-statistical model of Pt degradation is presented that encompasses the main particle-level degradation pathways namely dissolution, redeposition, coagulation, and detachment. A systematic algorithm is developed to process experimental inputs and generate outputs on kinetic rate parameters. Once the complete parameter space is explored using Monte Carlo techniques, an optimization routine is run to refine the results. In this way, unique, unambiguous rate parameters pertinent to different degradation mechanisms under various operating protocols have been extracted. It is shown that dissolution/redeposition increase with increasing upper potential cycling limit; particle detachment increases with increasing surface area of the carbon support, whereas dissolution is independent of the carbon support type.

Then a platinum oxide growth and reduction model is developed that implements interfacial exchange processes between platinum and oxygen atoms, as well as transport mechanism of oxygen vacancies through diffusion and field migration. A quasi-steady state model of oxide formation, growth, and reduction is developed. Oxide growth is seen to be sensitive to oxygen ion vacancy at the metal-oxide interface and the rate of platinum ion extraction across the interface.

The tools this thesis presents provide better understanding to the underlying relations of platinum degradation that can be used to enhance the lifetime of fuel cells. For example, reliable assessments of the prominent degradation mechanism under various operating conditions can be evaluated to set priorities for materials research.

Keywords: platinum degradation, oxide growth, oxide reduction, fuel cell

Acknowledgements

My husband, Ben, for uprooting and supporting my craziness throughout graduate school and the constant, “I promise it’s going to get better...” moments. The unwavering support of my parents for always believing in me even when I didn’t. My supervisor, Michael Eikerling, for showing me how to be a respected scientist, always having an open door for meaningful discussions, his endless patience, and never letting me take short cuts because he recognized potential beyond what I thought was possible. Drew Stolar for enlightening me to the world of industry and encouraging thoughtful and productive analysis. My supervisory committee members, Byron Gates and Krzysztof Starosta, for their time and useful insight. Tasleem Muzaffar for always being there for a sanity check or to translate Michael’s handwriting, as well as the entire Eikerling Research group past and present. Steve Rinaldo for sending me on the right trajectory for a successful PhD career including introducing me to LaTeX from the beginning. Thomas Kadyk for sharing knowledge through MATLAB code, thoughtful discussions, and always making time to give relevant input. Lastly, I would not have made it without my friends that helped me balance my work with play.

Table of Contents

Approval ii

Abstract iii

Acknowledgements v

Table of Contents vi

List of Tables ix

List of Figures x

List of Acronymns xiv

List of Symbols xvii

1 Introduction 1

1.1 Motivation 1

1.2 Fuel Cells 2

1.2.1 How Fuel Cells Work 4

1.2.2 Platinum Shortcomings 7

1.2.3 Importance of Modelling 8

1.3 Objectives 8

1.4 Outline 9

2 Literature Review 10

2.1 Catalyst Degradation 10

2.2 The Connection of Dissolution to Oxide Growth and Reduction . . . 14

2.3 Oxide Growth 16

2.4 Oxide Reduction 21

3 Modelling-Based Data Treatment and Analytics of Catalyst Degradation in Polymer Electrolyte Fuel Cells 23
3.1 Introduction . . . 23
3.2 Methodology . . . 24
3.2.1 Model Equations . . . 24
3.2.2 Algorithm Formulation . . . 28
3.3 Results and Discussion . . . 31
3.3.1 Experimental Data Set . . . 31
3.3.2 Algorithm Implementation . . . 32
3.3.3 Model Evaluation . . . 34
3.4 Summary of Results . . . 42

4 Modelling Oxide Formation, Growth, and Reduction of Platinum 44
4.1 Introduction . . . 44
4.2 Phenomenology of Oxide Formation, Growth, and Reduction . . . 45
4.3 Model Structure . . . 49
4.4 Model Equations . . . 50
4.4.1 Interfacial Kinetic Functions . . . 52
4.4.2 Flux Boundary Conditions . . . 54
4.4.3 Potential Boundary Conditions . . . 56
4.5 Nondimensionalization . . . 56
4.6 Summary . . . 59

5 Quasi-Steady State Solution and Results for Oxide Formation and Growth 60
5.1 Introduction . . . 60
5.2 Model Equation Modifications . . . 61
5.2.1 Non-dimensionalization . . . 62
5.3 Model Solution . . . 63
5.4 Adding Dimensions . . . 64
5.5 Parametric Analysis . . . 67
5.6 Comparison with Experimental Data . . . 69
5.7 Summary and Outlook . . . 74

6 Quasi-Steady State Solution and Results for Oxide Reduction 76
6.1 Introduction . . . 76
6.2 Model Equation Modifications for the Steady State Limit . . . 77

6.3 Model Solution 78
6.3.1 Parametric Analysis 79
6.3.2 Comparison to Experimental Data 82
6.4 Transient Solution 85
6.5 Summary and Outlook 88

7 Conclusion **89**
7.1 Overview of Main Results 89
7.2 Significant Contributions 91
7.3 Future Research Paths 92

Bibliography **94**

Appendix A Supporting Information **106**

Appendix B Platinum Degradation Code for Chapter 3 **110**
B.1 The Monte Carlo Simulation for STAGE I 110
B.2 The Optimization Routine for STAGE II 113
B.3 Files 116
B.3.1 degradation_pitm.m 116
B.3.2 degradation_help_pitm.m 117
B.3.3 degradation_parameters_pitm.m 118

Appendix C Platinum Oxide Growth and Reduction Code for Chapter 4 **120**
C.1 Main 120
C.2 Files 122
C.2.1 soln_to_a.m 122
C.2.2 fullOxideModel_parameters.m 122

List of Tables

Table 3.1 Experimental parameters 32

Table 5.1 Table of general parameter values for Section 5.5. 68
Table 5.2 Table of parameter values for Figure 5.7 70
Table 5.3 Table of parameter values for Figure 5.8 71
Table 5.4 Table of parameter values for Figure 5.9 73
Table 5.5 Table of parameter values for Figure 5.10 73

Table 6.1 Table of general parameter values for Section 6.3.1. 84
Table 6.2 Table of general parameter values for model comparison to experimental data for Figure 6.9. 86

Table A.1 Comparison of start values obtained at STAGE I vs. optimized values after STAGE II for Low Surface Area Carbon (LSAC) that correlates to Figure 3.3. [*] indicates parameters of extended experimental data set shown in Figure 3.4. 107
Table A.2 Comparison of start values obtained in STAGE I vs. optimized values after STAGE II for Medium Surface Area Carbon (MSAC) that correlates to Figure 3.6. [*] is the model results only including the dissolution/redeposition mechanism. 108
Table A.3 Comparison of start values obtained in STAGE I vs. optimized values after STAGE II for High Surface Area Carbon (HSAC) that correlates to Figure 3.8. 109

List of Figures

Figure 1.1 Photos taken July of 2017 at the Science Museum in London during a conference trip. The first fuel cell developed by Francis Thomas Bacon and used by NASA on the Gemini and Apollo manned space programs in the 1960s (right). 4

Figure 1.2 Schematic of typical Polymer Electrolyte Fuel Cell 5

Figure 1.3 Illustration of the morphology of the Anode Catalyst Layer (ACL) and Cathode Catalyst Layer (CCL) from a section of the Proton Exchange Membrane Fuel Cell including the Microporous Layer (MPL) and Proton Exchange Membrane (PEM). 6

Figure 2.1 Examples of Accelerated Stress Test protocols: a.) triangular wave and b.) square wave. 11

Figure 2.2 Illustration of processes involved in the catalyst degradation mechanisms of platinum in polymer electrolyte fuel cells. . . . 11

Figure 2.3 Unfolded cyclic voltammetry scan of platinum polycrystalline (black line) [1] overlaid with dissolution profile (blue line) from [2], labeled with the designated regions. Note: this is not exactly to scale, just intended to be an illustration to aide understanding. 15

Figure 3.1 Flowchart for algorithm employed in degradation analytics. . . 29

Figure 3.2 Goodness of fit function values (Equation 3.14) for the random sets of parameters sampled with the Monte Carlo method plotted vs. k_{dis} and R_0 for MSAC at 1.0 V_{RHE}. Grey points on the basal plane correspond to projections of the data points with goodness of fit values below the threshold of 3%. 33

Figure 3.3 Model (line) and experimental data (circles) for Low Surface Area Carbon (LSAC) at different ϕ_{UPL}: 1.0 V_{RHE} - purple; 1.1 V_{RHE} - red; 1.2 V_{RHE} - blue; 1.3 V_{RHE} - cyan after full parametric optimization according to Figure 3.1. 34

Figure 3.4 Model (line) and experimental data (circles) for Low Surface Area Carbon (LSAC) after full optimization of parameters at $\phi_{\mathrm{UPL}} = 1.2\ \mathrm{V_{RHE}}$ for the additional set of experimental data that included intermediate values of mean radius and PITM; parameters are shown in Table A.1 in the row labelled with a [*]. 35

Figure 3.5 Optimized best fit model results for k_{dis} (circles), k_{cgl} (diamonds), and k_{det} (squares) for LSAC at 80° C from Table A.1 in the Supporting Information. 37

Figure 3.6 Model (line) and experimental data (circles) for Medium Surface Area Carbon (MSAC) after full optimization according to the algorithm in Figure 3.1 at varying ϕ_{UPL}: 0.9 $\mathrm{V_{RHE}}$ - black; 1.0 $\mathrm{V_{RHE}}$ - purple; 1.1 $\mathrm{V_{RHE}}$ - red; 1.2 $\mathrm{V_{RHE}}$ - blue; 1.3 $\mathrm{V_{RHE}}$ - cyan. A reduced model only considering the dissolution/redeposition mechanism was applied to 0.9 $\mathrm{V_{RHE}}$ with the parameters reported in Table A.2 for the row labeled with a [*]. 38

Figure 3.7 Optimized model results for k_{dis} (circles), k_{cgl} (diamonds), and k_{det} (squares) for MSAC at 80° C from Table A.2 in the Supporting Information. 39

Figure 3.8 Model (line) and experimental data (circles) for High Surface Area Carbon (HSAC) after full optimization with the algorithm in Figure 3.1 at upper potential limit of 1.2 $\mathrm{V_{RHE}}$ with the parameters reported in Table A.3. 40

Figure 3.9 Comparison of the trends in catalyst dissolution rate (purple circles), the rate of detachment (blue squares), and the rate of coagulation (red diamonds) for Low Surface Area Carbon (LSAC), Medium Surface Area Carbon (MSAC), and High Surface Area Carbon (HSAC) at an upper potential cycling limit equal to 1.2 $\mathrm{V_{RHE}}$. 41

Figure 3.10 Mechanistic breakdown for LSAC at ϕ_{UPL} of a.) 1.0 $\mathrm{V_{RHE}}$ and b.) 1.3 $\mathrm{V_{RHE}}$. 41

Figure 3.11 Mechanistic breakdown for MSAC at ϕ_{UPL} of a.) 1.0 $\mathrm{V_{RHE}}$ and b.) 1.3 $\mathrm{V_{RHE}}$. 42

Figure 4.1 Schematic of Pt oxide growth; a.) Oxygen formation on surface; b.) PtO layer formation c.) Bilayer structure of PtO (yellow) and PtO_2 (light blue) with oxygen ion vacancies shown; . . . 46

Figure 4.2 General schematic of the oxide reduction process: a.) defect creation; b.) diffusion; c.) Pt filling; d.) Pt dissolution 47
Figure 4.3 Illustration of the boundary condition and oxide growth and reduction processes. 48
Figure 4.4 Species equations for growth, reduction, and dissolution 49
Figure 4.5 General schematic of the potential profile across the layers and boundary values. The dashed red line symbolized the potential distribution across the oxide layer which is not necessarily linear but will be determined using Eq. 4.3. 52
Figure 4.6 The interfacial kinetic function (f_{1f}) as a function of the normalized oxygen ion vacancy density at the M-O interface at varying Γ values. 53
Figure 4.7 The interfacial kinetic function (f_{1r}) as a function of the normalized oxygen ion vacancy density at the M-O interface at varying Γ values. 54

Figure 5.1 Oxygen ion vacancy density at the M-O interface as oxide layer thickness, λ, is increased at varying C_0 values. 64
Figure 5.2 Oxygen ion vacancy density at the M-O interface as a function of Φ a.) $\lambda = 0.5$; b.) $\Gamma = 1$. 65
Figure 5.3 Parametric dependence of oxide growth upon varying the rate constant, a.) k_1 across the M-O interface, and b.) k_2 across the O-E interface. 67
Figure 5.4 Parametric analysis of oxide growth upon varying a.) the non-dimensional parameter, Φ that includes the potential difference across the layer, and b.) the geometric parameter, ϵ, that relates to the density of the oxide layer. 68
Figure 5.5 Effect of varying, C_0, the oxygen ion vacancy density at the metal boundary required to promote oxide growth. 69
Figure 5.6 Dependence of oxide growth on Γ. 70
Figure 5.7 Model results applied to experimental data a.) reported at 1.4V from Imai *et al.* [3] and b.) from Fromhold *et al.* [4]. Parameters used are found in Table 5.2. 71

Figure 5.8 Model results applied to experimental data reported from Furuya *et al.* [5] for a.) 298 K and b.) 333 K at varying potentials: purple - 1.5V_{SHE}; blue - 1.3 V_{SHE}; cyan - 1.1 V_{SHE}. The model parameters are in Table 5.3. 71
Figure 5.9 Model results applied to experimental data of the oxidation of polycrystalline (pc) [purple], (110) [blue], and (112) [cyan] iron surfaces at 100° C from Graham *et al.* [6]. The parameters for the model are listed in Table 5.4. The model was scaled to the start of the experimental data similar to above. 73
Figure 5.10 Model results applied to experimental data of the oxidation of β-$Ni(OH)_2$ using experimental results from Ref. [7]. The parameters for the model are listed in Table 5.5. 74

Figure 6.1 Oxygen vacancy concentration across the oxide layer as thickness is decreased. Parameters used are listed in Table 6.1. . . . 79
Figure 6.2 Oxygen vacancy concentration across the oxide layer as k_{2r} is increased. Parameters are listed in Table 6.1. 80
Figure 6.3 Oxygen vacancy concentration at the M-O interface as a.) k_{1r} and b.) k_{2r} is increased. Parameters are listed in Table 6.1. . . 81
Figure 6.4 Oxygen vacancy concentration at the M-O interface as γ is increased. Parameters are listed in Table 6.1. 81
Figure 6.5 Parametric analysis of oxide layer thickness during reduction as a function of τ for a.) varied k_{1f} and b.) k_{1r}. Parameters are listed in Table 6.1. 82
Figure 6.6 Parametric analysis of oxide layer thickness during reduction as a function of τ for a.) varied k_{2f} and b.) k_{2r}. Parameters are listed in Table 6.1. 83
Figure 6.7 Parametric analysis of oxide layer thickness during reduction as a function of τ for a.) varied $\Delta\phi$ and b.) γ. Parameters are listed in Table 6.1. 83
Figure 6.8 Parametric analysis of oxide layer thickness during reduction as a function of τ for varied C_0. Parameters are listed in Table 6.1. 84
Figure 6.9 Model results applied to experimental data reported from a.) Ref. [8] and b.) Ref. [9]. The model parameters are listed in Table 6.2. 85

Acronyms

ACL	Anode Catalyst Layer	5, 6
AFC	Alkaline Fuel Cell	4
AFM	Atomic Force Microscopy	13
AST	Accelerated Stress Test	10, 11, 13, 45
BEV	Battery Electric Vehicle	2, 3
CCL	Cathode Catalyst Layer	5, 6, 8, 26, 27
DMFC	Direct Methanol Fuel Cell	4
DOE	United States Department of Energy	7, 31
ECSA	Electrochemically Active Surface Area	5, 6, 10, 12, 23, 24, 27, 28, 39, 42
EDS	Energy-Dispersive X-ray Spectroscopy	31
FCV	Fuel Cell Vehicle	2–4, 7, 10
GDL	Gas Diffusion Layer	5
GGM	Generalized Growth Model	21, 75

HSAC	High Surface Area Carbon	7, 31, 32, 34, 36, 37, 39–41, 93, 98
ICEV	Internal Combustion Engine Vehicle	2, 3
ICPMS	Inductively Coupled Plasma Mass Spectromter	14, 15
IL-TEM	Identical Location Transmission Electron Microscopy	11
LPL	Lower Potential Limit	14, 15, 45
LSAC	Low Surface Area Carbon	6, 7, 31, 32, 34–37, 39, 41, 91, 93, 96
M-O	Metal-Oxide	45, 47, 51–56, 62, 64–66, 68, 69, 73, 75, 79–83, 88, 89, 92
MEA	Membrane Electrode Assembly	31
MPL	Microporous Layer	5, 6
MSAC	Medium Surface Area Carbon	6, 7, 31, 32, 34, 36–39, 41, 42, 91, 93, 97
NHE	Normal Hydrogen Electrode	18
O-E	Oxide-Electrolyte	46, 47, 54–56, 62, 66, 68, 79–81, 89
ORR	Oxygen Reduction Reaction	5, 12, 14

PDM	Point Defect Model	16, 20, 21, 75
PEFC	Polymer Electrolyte Fuel Cell	4, 5
PEM	Proton Exchange Membrane	5, 6, 26
PEMFC	Proton Exchange Membrane Fuel Cell	6
PITM	Platinum-in-the-Membrane	13, 24–28, 31, 42
PM	Particulate Matter	1
PRD	Particle Radius Distribution	13, 24, 25, 32, 37
Pt	Platinum	17–19
SEM	Scanning Electron Microscopy	31
SHE	Standard Hydrogen Electrode	72
SOFC	Solid Oxide Fuel Cell	4
STEM	Scanning Transmission Electron Microscopy	18
TEAM	Transmission Electron Aberration-Corrected Microscopy	18
TEM	Transmission Electron Microscopy	18
UPL	Upper Potential Limit	14, 15, 24, 25, 36, 47, 91
XPS	X-ray photoelectron spectroscopy	73

Nomenclature

C	Oxygen ion vacancy concentration, mol cm^{-3}	65, 67, 73
$\tilde{C}$	Nondimensionalize oxygen ion vacancy concentration	80, 81
χ_e^2	Error fuction	27
C_0	Oxide vacancy density needed to promote oxide growth, mol cm^{-3}	58, 65, 67–74, 85, 87
$\bar{C}_{\mathbf{Pt}}$	Average platinum concentration, mol m^{-3}	25
$C_{\mathbf{Pt}}^{\mathbf{ref}}$	Reference concentration, mol m^{-3}	25
D	Diffusion coefficient, cm^2 s^{-1}	69, 71, 72, 74, 85, 87
ϵ	Expansion factor, mol cm^{-3}.	67–69, 71–74, 85, 87
F	Faraday's constant, 9.6485$\times 10^4$ C mol^{-1}	52, 62
f_{1f}	Forward functional at x = 0	69
f_N	Particle radius distribution function	25
Γ	Nondimensionalize γ	53–55, 58, 65, 71
$\gamma_{\mathbf{Pt}}$	Surface tension of Pt, J m^{-2}	25, 33
γ	Phenomenological parameter to quantify the sensitivity of the dependence of platinum extraction on the amount of oxide coverage, cm^3 mol^{-1}	58, 69, 71, 72, 74, 81–85, 87
J	Flux	62

κ_r	Thickness reduction rate constant, m s^{-1}	52, 58
κ	Thickness growth rate constant, m s^{-1}	52, 58, 63
k_{1f}	Forward reaction rate at x = 0, mol m^{-2} s^{-1}	68, 69, 71–74, 81, 83, 85, 87
k_{1r}	Reverse reaction rate at x = 0, mol m^{-2} s^{-1}	81–83, 85–87
k_{2f}	Forward reaction rate at x = L, mol m^{-2} s^{-1}	68, 69, 71, 72, 74, 80, 84, 85, 87
k_{2r}	Reverse reaction rate at x = L, mol m^{-2} s^{-1}	80–85, 87
$k_{\mathbf{det}}$	Detachment rate constant, s^{-1}	25, 27, 28, 31, 36, 37, 39
$k_{\mathbf{dis}}$	Dissolution rate constant, mol m^{-2} s^{-1}	25, 27, 28, 31, 33, 36, 37, 39
$k_{\mathbf{pitm}}$	Rate of PITM loss, s^{-1}	26–28, 31, 36
$k_{\mathbf{cgl}}$	Coagulation rate constant, s^{-1}	25, 27, 28, 31, 36, 37, 39
$k_{\mathbf{rdp}}$	Redeposition rate constant, m^{-2} s^{-1}	25, 27, 28, 31, 36
L_0	Reference thickness, cm	57, 69, 71, 72, 74, 85, 87
L	Oxide thickness, cm	16
λ	Oxide thickness, monolayers	57, 65, 68, 80, 81
$L_{\mathbf{CCL}}$	Cathode catalyst layer thickness, μm	27, 31, 32
$l_{\mathbf{CCL}}$	Cathode catalyst layer thickness normalized to initial thickness	27, 31, 36

M_N	dimensionless Pt mass moment of the normalized particle radius distribution function	26
$M_{\mathbf{Pt}}$	molecular weight of Pt, 195.084 g mol^{-1}	26
$M_{\mathbf{pitm}}$	dimensionless Pt mass moment associated with the formation of Pt in the membrane	36
m_V	Pt mass loading per unit volume, g m^{-3}	26
Φ	Dimensionless potential difference across the oxide	65, 68, 69
$\phi_{\mathbf{UPL}}$	potential cycling upper potential limit, V	24, 30–36, 38, 39, 41, 42, 90, 91, 96–98
ϕ	Potential, V	68
$\Delta\phi$	Potential difference across the oxide layer (ϕ_L-ϕ_0), V	69, 71, 72, 74, 83–85, 87
R	Gas constant, 8.3145 J mol^{-1} K^{-1}	52, 62
$\bar{r}_N$	Dimensionless mean radius moment of the normalized particle radius distribution function	31, 34, 36
R_0	Characteristic radius, nm	28, 30, 31, 33
$\rho_{\mathbf{Pt}}$	Density of platinum, mol cm^{-3}	26
S_N	Normalized electrochemically active surface area	34, 36
T	Temperature, K	69, 71, 72, 74, 85, 87
t	Time, s	16
τ	Dimensionless time	57, 80, 83–85
$V_{\mathbf{m}}$	Molar volume of Pt	25

$\mathbf{V_{RHE}}$	Volts relative to the reversible hydrogen electrode	10–15, 24, 30–36, 38–42, 73, 91, 96–98
x	Position	52, 62
ξ	Dimensionless position	57, 80
z	Electrons transferred	52, 62

Chapter 1

Introduction

1.1 Motivation

Undeniably the world's demand for power is growing and will continue to increase. There was nearly a 20% increase from 2006 to 2016 in the total world primary energy consumption according to the *BP statistical Review of World Energy 2017* of which, in 2016, over 85% of the energy used was fuelled by oil, natural gas, or coal [10]. The continued increase in energy consumption is due to many factors including an ever increasing population and an increase in per capita energy use that is linked to economic growth, as well as greater accessibility to electrical power in remote and developing areas [11]. It is important to understand the implications of our energy-hungry society to manage and control our usage. It is well-established that energy consumption is directly connected with greenhouse gas emissions, carbon dioxide being the largest influence on climate change caused by increased energy consumption in different regions of the world [12].

Despite persistent albeit naive political and social rhetoric denying the severity of global climate change, it is undoubtedly and highly researched that humans play a significant role in the steady trend of rising terrestrial temperatures. Detriments that are less discussed on a public stage compared to climate change, but equally important are human and environmental health effects from air pollution and ocean acidification. Humans have literally changed the chemistry of the oceans with the CO_2 uptake [13]. Not only does this affect the $CaCO_3$ levels critical to the strength and life of crustaceans and coral reefs, but it impacts the sea life that cannot survive in an acidic environment [13]. The leading contributors to the global disease burden is ambient air pollution; exposure to Particulate Matter (PM) with aerodynamic

diameter of less than 2-5 μm caused 4.2 million deaths worldwide in 2015, roughly 7.6% of deaths globally [14].

The focus of this thesis is not to discuss the potential collapse of human civilization but it is meaningful to understand the severity of the energy crisis to motivate the importance of this work. Road transportation contributed 16.9% of the total global CO_2 emission in 2012 [15]. As of 2013, 8.2% of greenhouse gases were attributed to passenger cars with an estimate to double by 2050 with the current growth of global car sales [15]. Although this is not the origin of the majority of CO_2 emissions, it is a significant amount and a direct way that every individual could help combat the global energy and climate change crises. There were nearly 65 million cars sold in 2014 [15]; imagine if everyone of those vehicles were replaced with a zero-emission vehicle. This would also show a collective dedication to the importance of slowing the rapid temperature rise encouraging other sectors to follow a sustainable energy route.

The two zero-emission consumer vehicles currently in production are Battery Electric Vehicles (BEVs) and Fuel Cell Vehicles (FCVs). Zero-emission vehicle refers to zero pollutant tailpipe emissions [16]. Vehicles can never be 100% emission free due to materials, manufacturing process, and recycling, but reducing emissions during the life of the vehicle is valuble. BEVs have a much richer history with mature battery technology driving it as compared to FCVs. The first mass-produced hybrid-electric vehicle was in 1997 in Japan when Toyota released the Prius whereas the release of the first retail fuel cell vehicle did not happen until 2008 with the Honda FCX Clarity [17]. Both, BEVs and FCVs have advantages and disadvantages and will continue to need technological advancements but it is not a matter of BEVs *or* FCVs, but BEVs *and* FCVs. In evaluating the technological prospects of both technologies, the main differentiating factors are range and recharging time, as well as an overall compatibility with an energy supply infrastructure. It makes more sense to have a BEV in the city if the driving time and range is short with a high density of charging stations. A FCV is more practical when driving long distances and needing quick refilling times. In the 1930s the electric car lost the battle to the Internal Combustion Engine Vehicle (ICEV) due to affordability and simplicity; the world can no longer afford to solely look at price and simplicity but sustainability and longevity must be a factor.

1.2 Fuel Cells

A fuel cell is an electrochemical device that converts chemical energy in the form of a fuel, e.g. hydrogen, directly into electrical energy. There is still debate whether it

was Christian Friedrich Schonbein or Sir William Robert Grove who was the first to discover the principle of a fuel cell around 1839 but both independently showed that a voltage could be measured from an electrochemical reaction of hydrogen and oxygen [17]. It was not until 1893 that Friedrich Wilhelm Ostwald experimentally determined the interconnection of the components of a fuel cell including electrode, electrolyte, oxidizing and reducing agents, anions, and cations [17]. Fuel cells are appealing because they are efficient and environmentally friendly.

Comparing the theoretical efficiencies, applying the ratio of Gibbs free energy and reaction enthalpy ($\Delta G/\Delta H$), a H_2/O_2 fuel cell operating under standard conditions achieves an ideal thermodynamic efficiency of 83%, which is excellent compared to the maximum efficiency of an Internal Combustion Engine Vehicle (ICEV) of less than 40%, but that does not account for other losses such as heat [18]. Unlike ICEVs, FCVs are not limited by the Carnot cycle. However, the vehicle is only as efficient and clean as the fuel source. Hydrogen can be produced using several methods namely through renewable energy via water electrolysis, natural gas using steam reforming, or coal through gasification [19]. Taking into consideration the hydrogen production process, the total fuel-to-electricity conversion efficiency for the FCV is about 55%, which is lower than a BEV [19], but overall it is clear that fuel cell vehicles are an efficient means of energy.

Perhaps in today's political climate, the biggest driver of the fuel cell market is the fact they are zero-emission provided the hydrogen is sourced from renewables. Government regulations and subsides are increasing globally to help slow the rapid rise in the temperature and reverse the poisoning of air. Death and illness due to poor air quality is an enormous financial burden on governments motivating an increase in resources dedicated to renewable energy.

The applications for fuel cells span from portable devices to stationary back-up power with the focus of this thesis on the transportation sector. There are many fuel cells in operation across the globe with the demand increasing at a rapid rate. The first operational fuel cell was developed by Francis Thomas Bacon and adopted by NASA in the 1960s for the Gemini and Apollo manned space programs; the fuel cell is on display at the Science Museum in London shown in Figure 1.1. Fuel cells are ideal in space because they can generate electricity and drinking water in enclosed areas. Many indoor warehouses employ fuel cell powered fork lifts for the fact they can run indoors without producing toxic fumes; other technologies that employ fuel cells include drones and stationary power stations [20, 21, 22, 23, 24, 25]. As of 2016,

Figure 1.1: Photos taken July of 2017 at the Science Museum in London during a conference trip. The first fuel cell developed by Francis Thomas Bacon and used by NASA on the Gemini and Apollo manned space programs in the 1960s (right).

Hyundai and Toyota have a commercially available FCVs [26] with the Honda Clarity available for lease in California.

Despite the positive momentum fuel cells have received over the past decade, there are many challenges that remain before FCVs are seen abundantly on roadways and in the average person's garage. A major hurdle holding back full-commercialization of FCVs is the hydrogen fill station infrastructure; the motivation to purchase a vehicle that cannot be conveniently filled is very low. A discussion of the hydrogen-fill station dilemma is beyond the scope of this thesis, but shows it will take a combined effort across many disciplines and sectors including political, commercial, and consumer-related interests to hurdle the challenges of FCVs. Another major challenge forcing the average consumer out of the fuel cell market is cost and durability. To understand the obstacles that remain internally in the fuel cell, the way they work is discussed briefly.

1.2.1 How Fuel Cells Work

There are many works in the literature that review the progress of the fuel cell and detail the processes; for the purposes of this thesis, just a brief overview is presented [17, 18, 24, 25, 27]. A fuel cell is an energy conversion device. There are many types of fuel cells that use various fuels and structures including but not limited to Solid Oxide Fuel Cell (SOFC), Direct Methanol Fuel Cell (DMFC), Alkaline Fuel Cell (AFC), and Polymer Electrolyte Fuel Cell (PEFC). A diagram of a PEFC is shown in Figure 1.2.

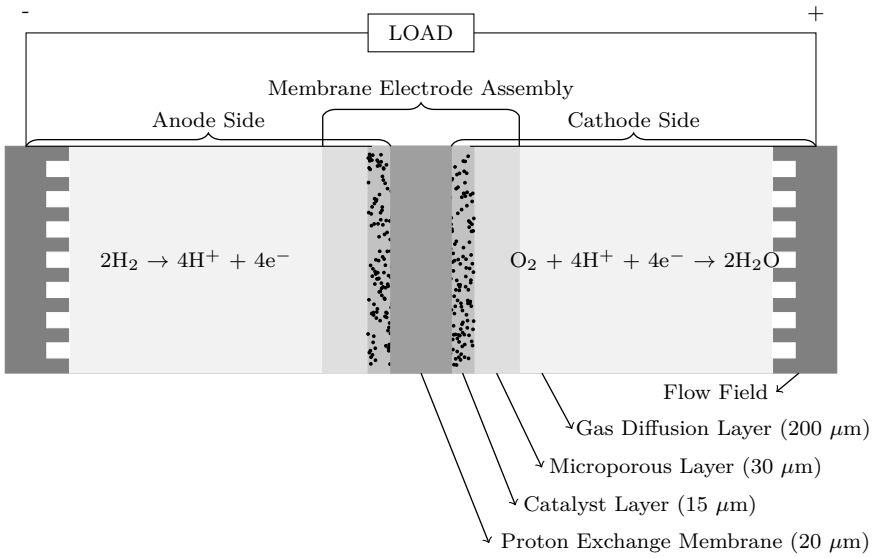

Figure 1.2: Schematic of typical Polymer Electrolyte Fuel Cell

Hydrogen (H_2), usually in the form of a gas, is fed into the anode side flow field where it is dispersed in the Gas Diffusion Layer (GDL) crossing the Microporous Layer (MPL) into the Anode Catalyst Layer (ACL) where the H_2 is oxidized. The H_2 is split into protons that cross the Proton Exchange Membrane (PEM) and electrons, which are redirected around an external circuit to create a current which powers the device. The reaction that occurs at the ACL is

$$2H_2 \rightarrow 4e^- + 4H^+. \tag{1.1}$$

The electrons are recombined with the protons and oxygen from air to complete the reaction at the Cathode Catalyst Layer (CCL) in the Oxygen Reduction Reaction (ORR),

$$O_2 + 4H^+ + 4e^- \rightarrow 2H_2O. \tag{1.2}$$

The current state-of-the-art catalyst layers in operational fuel cells use platinum nanoparticles decorated on carbon agglomerates as illustrated in Figure 1.3 [28]. The structure of the components in the catalyst layer plays an integral role in fuel cell design in order to optimize efficiency, durability, and power density of the fuel cell. It is essential for the catalyst support to be an excellent electron conductor to limit ohmic losses, as well as be highly porous. The porosity affords a maximum amount of surface area for the platinum nanoparticles to bind, creating a high Electrochem-

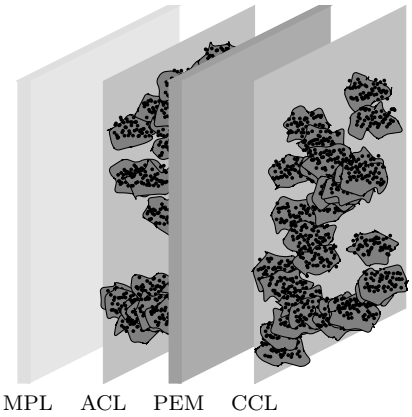

Figure 1.3: Illustration of the morphology of the Anode Catalyst Layer (ACL) and Cathode Catalyst Layer (CCL) from a section of the Proton Exchange Membrane Fuel Cell including the Microporous Layer (MPL) and Proton Exchange Membrane (PEM).

ically Active Surface Area (ECSA) while allowing for water and/or ionomer contact required for oxygen and proton transport. The overall reaction is

$$2H_2 + O_2 \rightarrow 2H_2O. \tag{1.3}$$

Portions of the catalyst layer are under-utilized because they are missing one or multiple key components of the catalyst layers namely the catalyst, catalyst support, and/or water/ionomer. Thus, many different support structures have been explored in order to increase the effectiveness and overall platinum utilization.

The degree of the catalytic activity and durability of the support material comes from the electronic character and geometric effects [29]. The ideal catalyst support would have: (i) a surface area that widely disperses the platinum particles while preserving the particle shape and size; (ii) an ideal porosity that is large enough for the platinum particles and ionomer to be dispersed but small enough to maintain the high surface area; (iii) be corrosion resistant, which relates to the degree of carbon oxidation; and (iv) hydrophilic channels and gas channels [29, 30]. Graphitization is used in the fabrication of carbon supports to obtain ideal porous morphologies and surface terminations where the degree of graphitization is determined by the process temperature [29, 31]; although the graphitic content is not homogenous and differs from the surface to the bulk [32]. Relative surface areas can be used to distinguish between different carbon supports, such as Low Surface Area Carbon (LSAC),

Medium Surface Area Carbon (MSAC), High Surface Area Carbon (HSAC), although there is no explicit industry standard defining the levels. LSAC has a high degree of graphitic content resulting in a very low micropore volume with the least amount of anchoring sites for Pt, e.g. multi-walled carbon nanotubes, Denka black, or Vulcan [33, 34, 35]. HSAC has the least number of graphitic walls, yielding well-dispersed Pt nanoparticles due to the large number of anchor sites, which results in increased kinetic performances, but is more prone to corrosion because of the number of surface sites [33, 36]; examples are Ketjen EC600JD or Black Pearls 2000 [29, 35]. The morphology of MSAC samples falls somewhere in between LSAC and HSAC samples [33, 35].

Although several metals and metal alloys can be used as a catalyst, there is a balance between the binding energy of reaction intermediates such as O_{ad} and OH_{ad}, and the catalyst activity. The effectiveness of different metals as catalyst can be predicted by the Sabatier principle [37]. Pure platinum is the best pure metal catalyst in terms of the oxygen reduction activity since its binding energy of O_{ad} and OH_{ad} is near the optimal value at which these species bind strongly enough to initiate the reaction, but weakly enough for the products to be released [38]. Moreover, platinum is more corrosion-resistant compared to the other potential catalysts in the harsh environment of the fuel cell with high acidity and high temperatures. Although platinum is the best catalyst in practice, it is a large contributor to the delay of commercialization of FCVs.

1.2.2 Platinum Shortcomings

The two largest issues delaying the commercialization of FCV are cost and lifetime attributed to platinum as a catalyst. Despite a valiant effort of research throughout recent decades to reduce the loading and increase the stability of platinum, the essential DOE benchmarks have not yet been met [39]. The catalyst layer accounts for 80% of the total cost of the fuel cell stack [40]. Current state-of-the art fuel cell stacks contain between 22 to 38 g of platinum per vehicle equating to about $1,500 USD, which is well above the DOE target of less than 10 g of platinum per vehicle or 0.125 g/kW for platinum-specific power density [22, 41]. The current lifetime of a FCV is less than 3500 hrs with a DOE target of 5500 hrs [18]. Thus, to increase affordability of FCVs, the platinum loading on the catalyst layers must be further reduced and the stability of the platinum that is deposited must be increased to improve the lifetime.

Understanding the underlying reasons for the degradation of the platinum in the CCL is the main focus of this thesis. It is essential to know the parametric effects of degradation mechanisms, in order to develop mitigation techniques.

1.2.3 Importance of Modelling

Whether building a stadium or designing a program, modelling is an essential component to nearly every industry. The importance of modelling can be broken down to two core elements: understanding and prediction. Models are used to simplify reality in order to better understand a system or process and convey the information in a meaningful way, such as supporting design criteria, understanding the necessity of individual components, and optimize operation protocols to name a few. Models with accurate predictive capabilities span from aiding the development of warranty information to determining the price of insurance to predicting the likelihood of your child having a disease proving the importance of a quality model. It is important to understand the gravity of a quality model, because a poor model can have detrimental consequences.

The goal of this thesis is to use physical-mathematical modelling to explain and give insight into the degradation phenomena prevalent throughout the literature. Observational analysis is useful to a point, but a full mechanistic understanding and precise quantification of different degradation mechanisms demands comprehensive physical-mathematical models. Understanding the underlying physical relations and model-based analysis of experimental data will lead to strategic design criteria essential to prolong the lifetime of the fuel cell [42]. Modelling effects, such as degradation of various carbon support types, degradation pathways, degradation mechanisms, can also save time and resources by limiting the expenses for experimental test materials and efforts.

1.3 Objectives

The primary objective of this thesis is to contribute to a better understanding of platinum degradation in fuel cells. This is achieved by expanding previous literature models on platinum degradation in order to resolve ambiguities, developing a refined model of interfacial kinetics of oxide formation, growth and reduction on platinum, and linking the degradation model to the model of oxide formation, growth, and reduction.

1.4 Outline

- Chapter 2 outlines the significant milestones in the literature pertaining to this thesis.
- Chapter 3 analyzes and expands upon an existing model of platinum degradation.
- A model of oxide formation, growth, and reduction is presented in Chapter 4. The model developed considers the kinetic reactions at the interfaces of the metal and oxide layer to promote growth and reduction.
- The model presented in Chapter 4 is solved for the case of oxide formation and growth in Chapter 5 and the results are compared to a wide range of experimental data.
- In Chapter 6 the model of oxide formation is expanded to include platinum oxide reduction phenomena.
- Chapter 7 ties the models together and discusses the future implications for the work presented. The outlook is discussed for expanding the presented models further.

Chapter 2

Literature Review

2.1 Catalyst Degradation

The platinum degradation problem has gained traction in recent literature studies. Accelerated Stress Tests (ASTs) are a useful way to simulate long-term effects on fuel cells and estimate lifetime in a laboratory environment in a manageable time period. During start up of a FCV, the cathode potential can reach up to 1.4 V_{RHE} [35, 43] and an automotive stack will see around 30,000 detrimental start-up events [43]. For platinum degradation in a catalyst layer, the AST is commonly performed by applying an electrical potential at varying protocols; some examples are: (i) potentiostatic tests, which hold the potential at a constant value and (ii) potentiodynamic tests, which cycle the potential at different wave shapes, as shown in Figure 2.1, such as triangular wave, which applies a potential to the electrode that increases and decreases at a set scan rate, square wave, or a combination of square or triangular waves. These tests can provide valuable information on electrode processes, quantify ECSA, and distinguish adsorption of different species. Origins of degradation in catalyst layers have been studied by distinguishing between mechanical, chemical, and electrochemical roots [44, 45]. A strong relationship is seen between applied electrode potential and the degradation rate and mechanism [33, 46, 2, 47, 48].

There are four main degradation pathways that decrease the amount of the ECSA in the catalyst layer resulting in power loss consisting of dissolution and redeposition, coagulation, and detachment, as shown in Figure 2.2 [42, 44, 49, 50, 51]. Dissolution is an atomistic loss of particle mass, shrinking the size of the particle. Redeposition occurs when there are dissolved metal ions in the electrolyte that redeposit on particles still attached to the support. The combination of particle shrinkage from dissolution and growth from redeposition, a process known as Ostwald-ripening [52], causes an

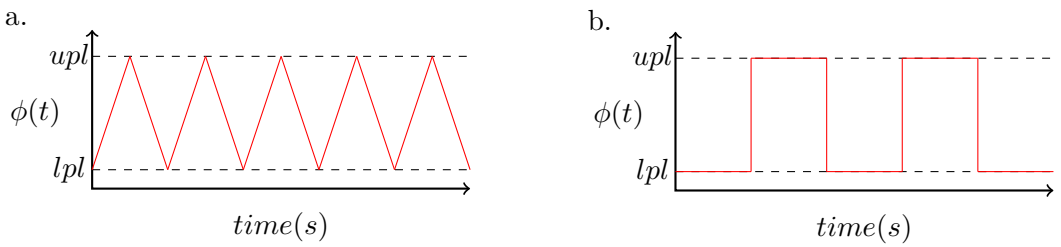

Figure 2.1: Examples of Accelerated Stress Test protocols: a.) triangular wave and b.) square wave.

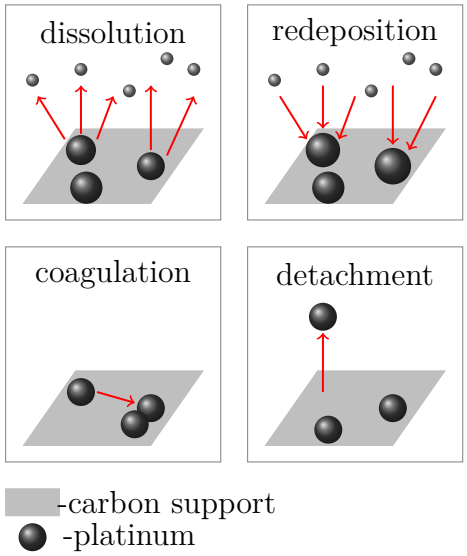

Figure 2.2: Illustration of processes involved in the catalyst degradation mechanisms of platinum in polymer electrolyte fuel cells.

overall surface area loss. At the same total mass, many small particles have a higher surface area compared to larger sized particles. Coagulation is the merging of two particles whereas detachment is the full release of a particle from the support usually attributed to support degradation such as carbon oxidation in the case of a carbon support. Different AST protocols impact the rate and mechanism of degradation leading to key insights into the platinum degradation phenomenon [47, 1].

In Ref. [53], Mayrhofer *et al.* performed accelerated aging tests by cycling a catalyst layer, made of carbon support decorated with platinum nanoparticles, similar to one found in a fuel cell, between 0.4 V_{RHE} to 1.4 V_{RHE} at 1.0 V/s for four hours. Individual nanoparticles were tracked visually using Identical Location Transmission Electron Microscopy (IL-TEM) during the test. The images showed clear platinum degradation that was attributed to the dissolution and detachment mechanism; no

signs of redeposition or coagulation were seen [53]. Ref. [54] showed that Pt dissolution increases significantly by increasing the upper potential limit from 1.0 to 1.4 V_{SHE}, but the ECSA was not seen to change significantly. From this the authors concluded that coagulation played a greater role than Oswald ripening in the coarsening process [54].

One of the most comprehensive studies of platinum dissolution in acidic media are from Refs. [46] and [2]. To gain insight into understanding platinum dissolution, the Mayhofer group used an electrochemical flow cell system connected to an inductively coupled plasma mass spectrometer to monitor platinum dissolution as a function of potential [46, 2]. Platinum dissolution was below the detection limit when cycling with an upper potential limit lower than 0.9 V_{RHE}. However, as the upper potential was increased above 1.0 V_{RHE}, the total amount of platinum in solution increased. The dissolution profiles showed that the majority of the dissolution occurs during the cathodic scan and was strongly dependent on the upper potential limit [46, 2], whereas there was significantly less dissolution that occurred in the anodic scan and was independent of the upper potential limit. The difference in quantity of platinum dissolved associated with scan direction is attributed to the platinum oxide growth and reduction and will be discussed in detail in the following section.

Along with testing protocols, catalyst particle size and shape are seen to exhibit an effect on the degradation process [42, 55, 56, 57]. Ref. [55] analyzed the particle size effect of the platinum in a catalyst layer under potentiostatic and potentiodynamic conditions to study the degradation phenomena. Potentiodynamic conditions showed significantly more degradation compared to potentiostatic operation under the same conditions. Dissolution increased for all particle sizes as the electrode potential was increased but overall smaller particles dissolved faster and to a larger degree than larger particles [55]. There is a balance between being small enough to have a high ECSA and large enough to be stable. The ideal platinum particle size is 3-5 nm, showing the best compromise of high stability and activity [42, 57, 58]. Although the sizes ranging 1-5 nm in diameter did not have a significant impact on specific activity, catalyst layers with a large fraction of particles smaller than 2 nm in diameter were seen to have much less stability compared to catalyst layers with average diameters of 3-5 nm [42]. In Ref. [57] platinum nanoparticles as small as 2 nm, provided they were highly dispersed and of uniform size, were seen to be quite durable and the ORR activity was also seen to be independent of particle size. Platinum nanoparticles that have more under-coordinated edge and corner sites result in faster degradation rates; for instance, particles around 2 nm diameter with a cubo-octahedral shape

consist of more than 50% under-coordinated edge and corner sites resulting in rapid degradation compared to larger particles [42]. Another study is Ref. [56] in which Atomic Force Microscopy (AFM) revealed that tetrahedral platinum nanoparticles commence dissolution at the apex of the particle rapidly at the beginning of the cycle whereas cubic nanoparticles dissolved gradually and showed higher durability.

On the topic of particle size, a pristine catalyst layer begins with an initial Particle Radius Distribution (PRD), but as the AST proceeds there is a clear change in the PRD revealing the extent of degradation [50, 59, 60, 61]. The shift to larger particles is attributed to redeposition and coagulation mechanisms. Platinum mass loss from the support is attributed to dissolution or detachment. Platinum dissolved in the electrolyte is available to be redeposited, but may also migrate into the membrane forming the so-called Platinum-in-the-Membrane (PITM). Platinum ions are pushed into the membrane to form the PITM band by crossover oxygen, but cease when they meet crossover hydrogen [62].

Models have been developed to gain a deeper insight into the underlying degradation relations that experiment alone cannot unfold. For instance, a model is necessary to understand the mechanistic breakdown at specific potentials and times. A steady-state model of Pt dissolution was developed in Ref. [63]. This model was expanded to include potential cycling in Ref. [64]. Ref. [52] focused on nonmonotonic dynamics of degradation processes. The model evaluated the evolution of the PRD based on Ostwald ripening. It was shown that the rate of redeposition is proportional to the mass loading of the catalyst and inversely proportional to the thickness of the catalyst layer [52]. Ref. [65] assessed the coagulation and detachment mechanisms individually. All four mechanisms shown in Figure 2.2 were incorporated and evaluated individually in Ref. [66], and solved in coupled form in Ref. [47].

Dissolution is a dominant degradation mechanism contributing a significant amount of platinum loss in the potential range of an operating fuel cell [65]. It was also shown that there is a significant increase in the rate of platinum dissolution while cycling when increasing the upper potential limit from 0.9 V_{RHE} to 1.2 V_{RHE} [66]. Ref. [44] claims that electrochemical dissolution prevails below 4 nm while chemical dissolution dominates in bulk-like metal, whereas Ref. [67] shows particles below 4 nm dissolve via direct electrochemical processes while larger particles form an oxide.

Despite the strong efforts, details of the mechanism are still not fully resolved. It is clear that platinum oxidation and reduction play a strong role in platinum dissolution proving it is imperative to understand the former before being able to have a full understanding of the latter.

2.2 The Connection of Dissolution to Oxide Growth and Reduction

Cyclic voltammetry is an electrochemical technique that applies a voltage at a fixed scan rate, e.g. 0.1 V s^{-1}, from a set Lower Potential Limit (LPL) to a set Upper Potential Limit (UPL) and then reverses the polarization back to the LPL and records the corresponding current; this methods corresponds to a triangular wave form as discussed and shown in Figure 2.1. The peaks on the voltammetry scans correlate to the surface science of the electrode. A typical platinum polycrystalline cyclic voltammetry scan is shown in Figure 2.3 but has been unfolded, i.e., usually the cathodic scan is shown below the anodic scan resulting in a cycle. The region where the electrode is free of adsorbents, known as the double layer charging region, is seen where there are no peaks during the anodic scan between 0.4 and 0.8 V_{RHE}. A peak begins to form just after 0.8 V_{RHE} which represents the onset of platinum oxide formation [68]. The higher the UPL and/or the slower the scan rate, the thicker the oxide layer becomes. Oxygen evolution occurs at higher potentials above 1.39 V_{RHE} [69, 70, 71]. Once the potential is reversed, there is a delay seen before the reduction of the oxide layer commences followed by hydrogen adsorption. The hydrogen is desorbed once the electrode potential is reversed again and the potential is increasing.

Figure 2.3 compares a dissolution profile to one cycle of an unfolded cyclic voltammetry scan to shows that dissolution is directly correlated to platinum oxide growth and reduction. There is a relationship to the quantity of platinum dissolved and the upper potential limit while cycling [2]. The blue curve in Figure 2.3 is a dissolution profile of one cycle collected by Topalov *et al.* in Ref. [2] with a UPL of around 1.8 V_{RHE}. The study used Inductively Coupled Plasma Mass Spectromter (ICPMS) coupled directly to an electrochemical flow cell shows that as the UPL is increased, the amount of platinum dissolved does not exceed about 25 pg cm^{-2} s^{-1} during the oxide growth regime beginning just after 1.0 V_{RHE} and holding steady to higher UPLs (the first peak of the blue curve in Figure 2.3) whereas during the reduction of the oxide (the second peak of the blue curve in Figure 2.3), the dissolution amount continues to increase as potential is increased and is roughly 250 pg cm^{-2} s^{-1} at 1.8 V_{RHE} [2]. Platinum dissolution is not seen to increase after about 1.0 V_{RHE} because the oxide layer creates a passivating effect protecting the electrode from degradation but also blocking active sites for the ORR. If the electrode is not cycled below the initiation potential of oxide reduction, that is, if there is still a passive layer present, no dissolution is detected [46]. Ref. [46] showed an electrode can be cycled without significant

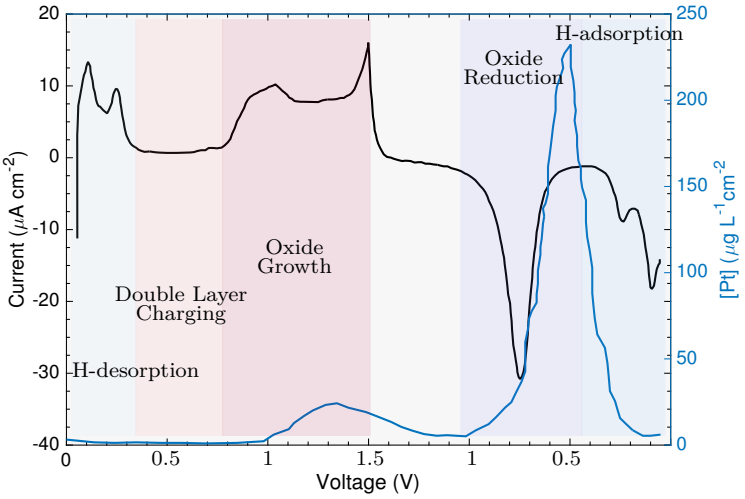

Figure 2.3: Unfolded cyclic voltammetry scan of platinum polycrystalline (black line) [1] overlaid with dissolution profile (blue line) from [2], labeled with the designated regions. Note: this is not exactly to scale, just intended to be an illustration to aide understanding.

platinum dissolution provided the LPL does not drop below around 1.1 V_{RHE} as to not reduce the passivating layer.

Lopes *et al.* also showed that the dissolution primarily takes place during the reduction of the platinum oxide [72, 73]. It was found that the rate of dissolution during the positive-going sweep (oxide formation) was small and considered a faradaic process and not closely related to the oxide formation kinetics, whereas the rate of dissolution during the negative-going scan (oxide reduction) was large and controlled by the positive potential limit as well as the scan rate [73]. ICPMS was also used but this time it was coupled to a stationary probe rotating disk electrode to measure dissolution rates of surface atoms to show the specific effect on the dissolution related to various Pt(hkl) surfaces. Pt(110) was seen to have nearly ten times more platinum ions dissolved in solution compared to Pt(100), which has slightly more than Pt(111) in one cycle with an UPL of just above 1.0 V_{RHE}. Nearly all the dissolution for all three Pt surfaces were collected during the reduction scan [72].

One explanation for the reason that the greatest amount of dissolution is seen during the reduction scan is that during reduction, if the oxygen ions escape faster than the Pt ions return to the metal, under-coordinated platinum atoms will remain that are prone to dissolution [46, 74]. Significant cycling through the reduction regime will

also cause roughening of the electrode surface making it more susceptible to degradation. This direct correlation motivates the necessity to fully understand platinum oxide growth and reduction in order to master the degradation of platinum in fuel cells. Oxide growth and reduction have been studied intensely over the last several decades and it is important to highlight the milestones published.

2.3 Oxide Growth

Oxide growth is an inevitable process that can be both beneficial and detrimental. On the one hand, oxides can create a passivating layer that protects the metal, while on the other hand it can limit the catalytic activity [75] and corrode the electrode upon reduction. Understanding oxide growth on metals spans an impressive history with an expansive range of topics from modeling general metal oxide growth to specific metals and utilizing various experimental techniques to quantify the growth laws [76, 77, 78, 79, 80, 81]. In 1923, Pilling and Bedworth [80] published one of the first articles discussing the oxidation of metals and outlining the hypothesis that the flux of oxygen is inversely proportional to the length of the path of diffusion, or, in this case, the thickness of the oxide layer.

$$\frac{dW}{dt} \propto \frac{1}{L} \tag{2.1}$$

where W is the quantity of oxygen bound by oxide layer formation, L is the thickness of the oxide layer, and t is time. It is assumed that all of the oxygen that diffuses across the oxide layer contributes to the increase in thickness, $W \propto L$ which leads to,

$$W^2 = At \tag{2.2}$$

where A is a rate constant. This results in a parabolic growth law which is seen as a common formula for many other metal oxide theories. In their paper, Pilling and Bedworth looked at oxidation of metals at high temperature. They determined the extent of oxidation by heating a metal spiral, holding the temperature constant, quickly removing and cooling, and determining the change in mass [80]. This technique, although effective, was highly prone to impurities. The parabolic growth law proves to be a good approximation for metal oxidation at sufficiently high temperatures and for sufficiently thick films [76].

Wagner's pioneering work of metal oxide theory paved the way for many well-known theories of oxide growth such as the Carbera-Mott model [76] and the Point De-

fect Model (PDM)[79]. Wagner's theory expanded on the model proposed by Pillings and Bedworth by incorporating charged particles into the model and using the Nernst-Planck equation to describe their transport. Wagner's theory correlates well with experimental data at sufficiently thick oxide films but is limited because it only describes the effect of species migration in the bulk without interface effects, thus the oxide must be thick enough that there are no or very limited influences from the charged interfaces.

In the middle of the 20$^{\text{th}}$ century, Mott developed another hypothesis to explain the formation of protective films at low temperatures [82]. The hypothesis was based on the phenomenon that a strong electric field develops in the oxide due to the oxide ions formed from the adsorbed oxygen atoms on the surface. These very strong fields induce migration of ions that thus build the oxide layer without much help from temperature. Mott explained that electrons can pass the film easily, while a very strong field is required for ions to penetrate it. This results in a logarithmic growth law of the type

$$\frac{1}{L} = A - B\ln(t). \tag{2.3}$$

A couple of years later, in 1949, Cabrera joined Mott and together they developed the well-know Cabrera-Mott model [76]. The model expanded on Mott's hypothesis. Due to the strong field, every ion which escapes from the metal will be pulled across the film, thus the rate of oxidation is determined only by the rate at which ions escape from the metal. The model accounted for the field-dependent activation energy of the Pt extraction process,

$$\frac{dL}{dt} = A\exp\left(-\frac{E}{k_{\text{B}}T}\right)\exp\left(\frac{Q\phi}{k_{\text{B}}T}\right) \tag{2.4}$$

where E is the activation energy for the formation of a metal ion in the oxide, ϕ is the field in the film, k_{B} is the Boltzmann constant, Q is a constant that accounts for the charge on the ion, and T is the temperature. This concept only applies if the film is thin enough for interfacial processes to dominate the growth. Thus, in the thick film regime, the parabolic law is expected to dominate the growth whereas a logarithmic growth law dominates for thin films. The Cabrera-Mott model does not consider specific structures or kinetics of different metals [76].

Validation of oxide growth models through experimental data became increasingly prevalent as technology progressed. As is known, metal oxidation is a function of potential, temperature, and time; in the times of Pilling and Bedworth [80], only the

temperature was varied, as this was the simplest approach to take albeit also being prone to contamination of the oxide layer. To study the effect of potential and time, a current can be applied to a metal and the voltage recorded, or a voltage can be applied and a current is measured. The change in resistance can also be determined. A change on the surface, i.e. different structure or adsorbed ion(s), will result in a change in current, potential, and/or resistance [83]. The difficulty comes when determining the thickness of the oxide layer. Usually this is done by correlating the amount of charge reduced from the surface, which is caused by the oxygen leaving, to the thickness of the oxide layer. For example, the amount of current is measured as the oxide layer is being reduced while cycling the electrode; this current can be related to the amount of oxide. The difficulty is, in order to relate this charge to the oxide layer thickness, the exact structure must be known because different lattice structures can have the same effective charge from the same number of oxygen atoms but different thicknesses due to different densities or atom packing.

A significant hurdle is the size of the oxide layer particularly when discussing platinum; it is essential to have sub-Angstrom resolved microscopy, for which, within the last decade, there has been a huge leap with TEM, STEM, and TEAM. The biggest challenge for these measurements is that the sample must be in a vacuum. This poses a problem because the oxide must be removed from the electrolyte and the potential source prior to measurement, which may cause the oxide layer to undergo structural changes [84]. There are also challenges in distinguishing oxygen atoms from platinum due to the fact that lighter atoms deflect electrons less than heavier atoms, which means that only the platinum ions show up on an image [85]. Despite the significant challenges, there has been upstanding studies throughout the literature.

Schuldiner and Roe pioneered work in 1963 to determine the double layer capacitance and the number of hydrogen and oxygen atoms on the Pt surface using a charging curve [70]. A charging curve uses a galvanostat to hold the current constant while recording the voltage of the electrode. Changes in the voltage are associated with different reactions happening on the surface. Schuldiner and Roe determined a series of events that occur on the Pt anode from the distinct four regions seen on their charging curve. They designated the regions as hydrogen ionization region (0 to 0.55 V_{NHE}), double layer charging region (0.55 to 0.88 V_{NHE}), oxygen atom adsorption region (0.88 to 1.76 V_{NHE}), and molecular oxygen evolution region (1.76+ V_{NHE}) [70]. Understanding surface chemistry was still in its early stages when Schuldiner and Roe wrote their paper, thus focusing on measuring active surface area, double layer capacitance, and the number of hydrogen and oxygen atoms and not specifically

on the oxidation processes but their work proved the importance of understanding surface chemistry.

Feldberg *et al.* also published an article in 1963 discussing the formation and dissolution of a Pt oxide film [86]. Charging curves were used for the experimental work; they also proposed an explanation of the mechanism and kinetics of the oxide film processes. Concern was expressed in reproducibility due to the high probability of impurities in the solution. To determine the kinetics, Feldberg *et al.* [86] modified the conventional electrochemical rate equation, i.e., they used a modified Butler-Volmer equation. The model showed consistent logarithmic plots of surface oxidation with experimental data, but it was only tested to below 500 seconds.

Vetter and Schultze published a series of articles that gave the most detailed analysis of the kinetics of the electrochemical formation and reduction of oxide layers on platinum to date in 1972 [87, 88]. Details in the articles include the place exchange mechanism, charging curves using galvanostatic pulse measurements, and a kinetic model of oxide layer formation. It is noted that the oxygen atoms are first chemisorbed from the electrolyte solution and then the oxygen atoms are exchanged for Pt atoms, which is the rate determining step, then a thicker layer is formed; this is still the widely accepted theory today [87, 88]. The oxide coverage was determined by calculating the ratio of hydrogen adsorption charge to cathodic charge of oxide reduction [87]. Vetter and Schultze developed their model in a similar manner of Feldberg *et al.* [86]. Some shortcomings include, the experiment was not performed to very long times, impurities are likely to be involved on the surface between charging and discharging, and degradation could occur between runs.

Another experimental method to show multiple mechanisms occurring during the oxidation process was presented by Shibata in Ref. [83] in 1977. Shibata measured resistance data as a function of the total amount of oxide. They showed that there are clearly two regions of the resistance vs coverage curve; first there is no resistance seen up to 2 mC cm^{-2} of oxide and then a resistance is seen that increases linearly with the total amount of oxide [83]. Shibata attributed this change in resistance to a bilayer structure of oxide on Pt, which they called α to the first oxide layer and β to the second layer. The bilayer structure has become a widely accepted idea but is usually designated as a Pt-O layer and an α-PtO_2 layer [89] according to the specific oxide lattice structures.

Angerstein-Kozlowska *et al.* used linear potential sweep voltammetry to show that the pseudocapacitance is not constant with increasing potential, as earlier studies had suggested [90]. Linear sweep voltammetry is a common method used to study electro-

chemical surface effects by sweeping the potential linearly with time while recording a current. One variation to the linear sweep method is cyclic voltammetry where the applied potential is reversed and swept back to the initial starting point. Cycling the voltage and recording the current allows for much more in depth electrochemical studies. Now the potentiodynamic case of the surface effects could be studied, not just the potentiostatic case.

The development of oxide growth models has not slowed in recent years. Macdonald developed the PDM which incorporated some of the structural aspects of the oxide layer including the bilayer structure that is commonly seen in metal oxides [79]. The PDM defined the mechanisms at each interface and developed a growth model that included reaction kinetics and incorporates pH and current; the model is not specific to platinum, and does not account for different electrode structures. Dissolution of the film is also discussed, but the mechanism of reduction of the oxide layer is not. The PDM has a strong foundation and is widely referred to. The growth law developed by Macdonald and others that built upon it follows a direct logarithmic dependence.

Conway wrote a comprehensive review of electrochemical oxide film formation, in which the oxidation process specific to platinum was presented [77]. Conway showed that there is a better basis for a direct logarithmic growth law for platinum oxidation compared to an inverse logarithmic one [91]. Conway emphasized the importance of incorporating the surface electrochemistry into the model. A common trend is to use an empirical approach when developing a growth law, first looking at the trend of the experiment and then developing a model that "fits" best.

Oxide growth is a very complex process. Simply assigning inverse logarithmic, direct logarithmic, or parabolic growth and building the theory around it falls short of encompassing the full growth process. A few common shortcomings are seen across the oxide growth models in the literature. Many models and experiments do not show the trend at very high times, e.g. above 10000 seconds. None of the growth laws discussed show any growth limit. Sun *et al.* [69] modified the PDM by including a linear term (C) to account for dissolution of the metal. This allows the oxide to achieve a steady state thickness [69],

$$\frac{dL}{dt} = Ae^{aV-bL} - C. \tag{2.5}$$

Sun's model implies that to achieve a steady state thickness, dissolution must also occur.

The experimental data of platinum oxide growth from Topalov *et al.* [2] shows that at a potential hold, there is an initial spike in platinum dissolution as the oxide layer first begins to form then the dissolution drops to nearly undetectable limits as time progresses until the oxide layer is reduced, at which point the majority of dissolution occurs dependent on the thickness of the oxide layer [2]. There is no indication that there is any dissolution as the oxide grows beyond the initial spike which is inconsistent with Sun's hypothesis. Also, there is no experimental data that shows a clear steady state condition on the surface but instead a significant slowing of the oxide growth. This leads to the assumption that the levelling off of the oxide growth is the result of a migration rate approaching zero, but never ceasing until the oxide is reduced.

Marcus's group at Chime Paris Tech has recently developed a so-called Generalized Growth Model (GGM) to describe oxide film growth on metals and alloys [78, 81]. Unlike the PDM, the GGM does not assume a potential drop at the oxide/film interface nor that the electric field in the oxide remain constant as the oxide layer grows. The model describes the oxide growth by defining two cases; i) the growth controlled by migration of charged species through the oxide layer; and ii) the growth controlled by injection of charged species at the metal/oxide interface. In the first case, the Nernst-Planck relation is employed [81]. Cabrera-Mott kinetics are applied for the second case based on an equation describing the probability of a cation escaping the metal; this is assumed to only occur in the presence of a very strong electric field, as obtained for a thin oxide film. The dissolution of the oxide film is also considered in the GGM. Similar to the PDM, the oxide film will be stable when the growth rate is equal to the dissolution rate. To solve the model, Marcus *et al.* defined equations to explain every probable reaction to aid oxide growth and combined them. The numerical simulation is presented in a separate paper by Leistner *et al.* [78]. The model shows relatively good agreement, but only a narrow set of experimental data was compared.

2.4 Oxide Reduction

Studies of oxide reduction are not as prevalent throughout literature as oxide growth. However, several methods have been used to explore the reduction phenomena including potentiostatic measurements [92], galvanostatic pulse measurements [88], spectroscopy [8, 9, 93, 94], and computations with DFT [75]. The reduction process is dependent on the properties of the oxide layer and in turn the oxide formation con-

ditions of the layer [88, 93]. A thicker layer and/or a layer that has been aged, resulting in more homogeneity, will require a higher overpotential in order to be reduced [88, 95]. The thickness of the layer will also dictate the degree of the irreversibility of the growth process; below a certain coverage, θ, the platinum atoms can easily return to their original site [93] and the oxide layer will be reduced uniformly [88]. However, a thicker oxide layer will show greater irreversibility, reorganization, and disorder [93, 94]. At coverages above $\theta = 1$, the reduction process will be non-uniform and begin at edge defects [88]. The reduction process will proceed electrochemically [92]. Refs. [96] and [97] showed evidence that the 2D film is first reduced beneath the oxide layer. This is supported by the fact that the majority of the dissolved Pt in solution after the reduction is Pt(II), which is the oxidation state of platinum in the Pt-O layer, and not Pt(IV) found in the Pt-O_2 layer on top, even at high upper potential limits [51]. Once the reduction commences, the process proceeds significantly faster compared to the oxidation process [8]. Most of the platinum will return to the bulk Pt layer in a disordered fashion; the further the platinum in the oxide layer is away from the bulk layer, the harder it will be to return to its original position [98].

Despite the ongoing research, there are still ambiguities that need to be resolved in oxide reduction. For instance, it is unclear at which interface the electron transfer occurs [93]. Although the exact kinetics of oxide reduction is still undetermined, the general consensus is a two-step reduction from PtO to PtOH and from PtOH to Pt [75, 8, 99], which can be described as a pseudo-first-order one-step reaction [9]. Ref. [100] described a general Fickian transport model that assumed that subsurface oxygen ions diffuse through lattice vacancies created in the reduction process that is coupled with oxygen removal at the surface. Ref. [88] stated that reduction proceeds through the transport of oxygen vacancies. In Ref. [66] Rinaldo and Eikerling developed a kinetic model that captures the dynamics of formation and reduction of chemisorbed oxygen at lower potentials.

First we present a modelling-based analysis of platinum degradation. This motivates the development of an oxide formation, growth, and reduction model developed in Chapter 4. In Chapter 5 we solve the steady-state oxide formation and growth limit and in Chapter 6 we expand the model to include platinum oxide reduction.

Chapter 3

Modelling-Based Data Treatment and Analytics of Catalyst Degradation in Polymer Electrolyte Fuel Cells

H. Baroody, D. Stolar, M. Eikerling, Electrochimicia Acta, 283: 1006-1016, 2018. https://doi.org/10.1016/j.electacta.2018.06.108

Material from this publication is used in this chapter with permission from Elsevier.

Author Contribution: ME supervised the original research. HB worked directly with DS to expand a previously developed degradation model and apply it to Ballard data. This prompted the need for HB and DS to develop the systematic algorithm. HB performed the extensive data analysis. HB and ME wrote the manuscript. DS and ME reviewed the work.

3.1 Introduction

This chapter presents a method for modeling-based treatment and analytics of experimental data to determine kinetic parameters for specific degradation mechanisms. The parameters allow for useful insight for industry including in view of materials selection, electrode design, and setting operating conditions. Experimental data monitored and analyzed include the ECSA, thickness reduction, average particle size,

amount of PITM, and PRD. The model expands on the models discussed at the end of Section 2.1 [47, 63, 64, 65, 66]. A modelling framework was developed that used a continuity equation to describe the propagation of the PRD. It accounts for all four degradation mechanisms illustrated in Figure 2.2. The results allowed the temporal evolution of particle number density, mean radius, mass active platinum, concentration of platinum ions in solution and ECSA to be calculated and compared to experimental data at different cycling protocols [66]. From the analysis in Ref [66], mechanisms were evaluated separately and it was found that the dissolution and re-deposition mechanism could explain the surface-area loss data under all conditions (UPL = 0.9 and 1.2 V_{RHE}) whereas coagulation and detachment were only seen to correlate to the data at 1.2 V_{RHE} [66]. The four mechanisms were coupled in Ref. [47] where individual mechanistic contributions were shown for different UPL under different cycling conditions.

Several issues arose which demanded us to refine the fully coupled model. The three main issues in Ref. [47] include: (i) results of the fitting are sensitive to input parameters, i.e., altering the starting values that should in principle be arbitrary, leads to different kinetic parameters; (ii) the values of kinetic rate parameters are not consistent with single mechanism models or literature results; and (iii) at high upper potential limit (ϕ_{UPL}) (1.2 V_{SHE}) the model overpredicts the PRD shift.

This work aims to resolve the ambiguities in the coupled degradation model and reconcile the inconsistencies identified in Ref. [47]. To achieve this several tasks are implemented: (i) the previous model is expanded to account for the effluence of Pt ions into the polymer electrolyte membrane, a sink of platinum mass so far not previously considered in the model; (ii) we devise an algorithmic procedure for fitting of experimental data and parameter extraction; and (iii) consider more diverse data sets.

3.2 Methodology

3.2.1 Model Equations

The bulk of the model equations were first developed in the decoupled model defined in Refs. [52, 63, 64, 65, 66]. Here, we will review the formalism and explain how the impact of PITM is added to it. To account for the evolution of the particle radius distribution, $f_N(r,t)$, normalized to the total number of particles in the initial distribution, the continuity equation used with contributions from each mechanism

was developed from theories of Wagner, Lifshitz and Slyozov [52] and is indicated below,

$$\frac{\partial f_N(r,t)}{\partial t} = -\underbrace{\frac{\partial}{\partial r}\left[f_N(r,t)\frac{dr}{dt}\right]}_{\text{dissolution/redepostion}} + \underbrace{J^+ - J^-}_{\text{coagulation}} - \underbrace{k_{det} f_N(r,t)}_{\text{detachment}}. \tag{3.1}$$

where f_N(r,t) is the PRD function, which is a function of particle radius, r, and time, t. The detachment mechanism contribution has a rate constant k_{det} (s^{-1}). The $f_N(r,t)$ contribution from coagulation derived from the Smoluchowski equation,

$$J^+ = \frac{1}{2} k_{cgl} \int_{0+}^{r} \frac{r^2}{(r^3 - \tilde{r}^3)^{2/3}} f_N\left((r^3 - \tilde{r}^3)^{1/3}, t\right) f_N(\tilde{r}, t) d\tilde{r} \tag{3.2}$$

$$J^- = k_{cgl} \int_{0+}^{r} f_N(r,t) f_N(\tilde{r}, t) d\tilde{r}. \tag{3.3}$$

where k_{cgl} (s^{-1}) is the coagulation rate constant and $\tilde{r}$ is the radius of the merging particle. To account for dissolution and redeposition, the rate of radius change for individual particles is given as,

$$\frac{dr}{dt} = V_m k_{rdp} \bar{C}_{Pt}(t) \exp\left(-\frac{R_0}{r}\right) - V_m k_{dis} C_{Pt}^{ref} \exp\left(\frac{R_0}{r}\right), \tag{3.4}$$

where the characteristic radius is defined as,

$$R_0 = \frac{V_m \gamma_{Pt}}{RT}, \tag{3.5}$$

where R is the ideal gas constant, T temperature, and the rate constants are k_{dis} (m s^{-1}) for dissolution and k_{rdp} (m s^{-1}) for redeposition. Equation 3.4 was derived from Talapin *et al* [101]. The averaged molar concentration of dissolved platinum in solution is $\bar{C}_{\text{Pt}}$, V_{m} is the molar volume of platinum, $C_{\text{Pt}}^{\text{ref}}$ the reference concentration of Pt for the electrolyte in contact with the Pt/C electrode, and γ_{Pt}, the surface tension of platinum. We assume a constant surface tension. It was discussed in Ref [65] that although surface tension will change as the surface changes, e.g. due to the growth of an oxide layer, the variation is negligible when comparing to the nearly 2000 times increase in the dissolution rate constant from an Upper Potential Limit (UPL) of 0.9 V_{RHE} to 1.2 V_{RHE}.

The overall mass balance of platinum was modified from the previous model to account for PITM. Incorporating PITM alters several model equations. Platinum that is dissolved in solution not only is available to redeposit as before but could

also be lost to the membrane. This is added to the total mass balance equation, as well as the mass moment associated with PITM and dissolution. The total amount of PITM is determined using the rate of formation of PITM (k_{pitm}) and the $\bar{C}_{Pt}$ difference between the CCL and the membrane, where the concentration is assumed to be zero. The rate of change in the normalized Pt mass moment associated with PITM formation (M_{pitm}) is,

$$\frac{dM_{\text{pitm}}}{dt} = \frac{k_{\text{pitm}}\bar{C}_{Pt}M_{\text{Pt}}}{\frac{4}{3}\pi\rho_{\text{Pt}}\int_{0+}^{\infty} r^3 f_N(r,0)dr}. \tag{3.6}$$

where k_{pitm} ($\text{m}^3\ \text{s}^{-1}$) is an effective rate constant, derived from considering diffusion of Pt ions or ion complexes into the Proton Exchange Membrane (PEM). M_{Pt} is the atomic weight of platinum and ρ_{Pt} is the density of platinum. The mass loss from dissolution is,

$$\frac{dM_{\text{dis}}}{dt} = \frac{4\pi\rho_{\text{Pt}}\int_{0+}^{\infty} r^2 f_N(r,t)\frac{dr}{dt}dr}{\frac{4}{3}\pi\rho_{\text{Pt}}\int_{0+}^{\infty} r^3 f_N(r,0)dr} \tag{3.7}$$

where the rate of particle radius change due to dissolution and redeposition in the support phase is given by dr/dt as shown in Equation 3.4. The rate of change in concentration of dissolved Pt ion complexes in the catalyst layer electrolyte is,

$$\frac{d\bar{C}_{Pt}}{dt} = -I_{\text{v}}\frac{m_v}{M_{Pt}}\left(\frac{dM_{\text{dis}}}{dt} + \frac{dM_{\text{pitm}}}{dt}\right), \tag{3.8}$$

where I_{v} is the water volume fraction in the catalyst layer and m_V the platinum mass loading per unit volume. Using the full solution to Equation 3.1 allows for temporal moments to be determined. These equations were developed in Ref. [52]. The temporal evolution of the normalized moments of the distribution of platinum particles on the support include mean radius,

$$\bar{r}_N(t) = \frac{\int_{0+}^{\infty} r f_N(r,t)dr}{\int_{0+}^{\infty} f_N(r,t)dr}\frac{\int_{0+}^{\infty} f_N(r,0)dr}{\int_{0+}^{\infty} r f_N(r,0)dr}, \tag{3.9}$$

surface area,

$$S_N(t) = \frac{\int_{0+}^{\infty} r^2 f_N(r,t)dr}{\int_{0+}^{\infty} r^2 f_N(r,0)dr}, \tag{3.10}$$

and mass,

$$M_N(t) = \frac{\int_{0+}^{\infty} r^3 f_N(r,t)dr}{\int_{0+}^{\infty} r^3 f_N(r,0)dr}. \tag{3.11}$$

For a given set of rate constants (k_{dis}, k_{rdp}, k_{cgl}, k_{det}, k_{pitm}), Equation 3.1 is solved for $f_N(r,t)$, using Equations 3.2 to 3.5. Having obtained $f_N(r,t)$, $\bar{r}_N(t)$, $S_N(t)$, and $M_N(t)$ can be calculated with Equations 3.9 to 3.11. The mass of the total dissolved Pt and of PITM can be obtained by integrating Equations 3.6 and 3.7 over time. We assume that the Pt loss via the detachment mechanism can be attributed to carbon corrosion. The mass of platinum due to detachment can be obtained from the overall mass balance equation,

$$M_{\mathrm{det}} = 1 - M_N - M_{\mathrm{pitm}} - \bar{C}_{Pt}\frac{m_v}{M_{\mathrm{Pt}}}, \tag{3.12}$$

where all the masses are normalized to M_{Pt}. For simplicity, we assume a simple linear relation between the normalized thickness change, Δl_{CCL}, and M_{det},

$$M_{\mathrm{det}} = \Delta l_{\mathrm{CCL}}(t) = 1 - \frac{L_{\mathrm{CCL}}(t)}{L_{\mathrm{CCL}}} \tag{3.13}$$

where L_{CCL} is the thickness of the cathode catalyst layer.

Equations established in this section describe how experimentally observable changes in mean particle radius, ECSA, PITM, and L_{CCL} can be calculated in the model, once the solution for $f_N(r,t)$ has been found. These equations thus establish the link between macroscopic observables for structure and composition of the CCL and the kinetics of microscopic degradation processes.

To apply the model directly to experimental data, we define the goodness of fit as,

$$\begin{aligned}\chi_e^2 = W_{\mathrm{e}} \sum_{i\in S_e} \left(\frac{(x_{\mathrm{e,i}} - \bar{x}_{\mathrm{e,i}})}{h_{\mathrm{e}}}\right)^2 + W_{\mathrm{r}} \sum_{i\in S_r} \left(\frac{(x_{\mathrm{r,i}} - \bar{x}_{\mathrm{r,i}})}{h_{\mathrm{r}}}\right)^2 \\ + W_{\mathrm{p}} \sum_{i\in S_p} \left(\frac{(x_{\mathrm{p,i}} - \bar{x}_{\mathrm{p,i}})}{h_{\mathrm{p}}}\right)^2 + W_{\mathrm{d}} \sum_{i\in S_d} \left(\frac{(x_{\mathrm{d,i}} - \bar{x}_{\mathrm{d,i}})}{h_{\mathrm{d}}}\right)^2,\end{aligned} \tag{3.14}$$

where W_{k} denote weights. $\bar{x}_{\mathrm{k}}$ and x_{k} are experimental and model values respectively, and h_{k} is the correlating scaling factor with k designating the data set (e = ECSA, r = mean radius, p = PITM, d = detachment/catalyst thickness); each summation is over all elements i of a given data set S_k. This allows for the ability to simultaneously fit the experimental data. Previous literature studies only considered the goodness of fit in ECSA loss.

3.2.2 Algorithm Formulation

The algorithm implemented in this work is illustrated in Figure 3.1. The goal of the algorithm is to determine a unique solution for the six unknowns (R_0, k_{dis}, k_{rdp}, k_{cgl}, k_{det}, k_{pitm}) for a given experimental data set. The outside columns define the inputs (right column) and outputs (left column) of the model. The middle part details the inner workings of the algorithm. There are two stages: STAGE I involves Monte Carlo sampling of the parameter space to identify input values for STAGE II, where parameter values are optimized using a direct search algorithm.

Monte Carlo Method

As mentioned, one of the goals in refining the model beyond the coupled degradation model implemented in Ref. [47] was to resolve ambiguities. The hope initially was to achieve this simply by adding PITM physics to the model and expand the experimental data set to simultaneously fit mean radius, PITM, thickness loss, and ECSA loss. Unfortunately, it was not that straightforward. Even with the extended data set, there were still not enough constraints with having six free parameters. We needed to devise a strategy to systematically constrain and/or limit the free parameters such that the results were independent of the initial values or ensure that the initial values used were intentionally chosen. The Monte Carlo method is a numerical technique that uses random sampling to obtain meaningful results through statistical analysis. This method was implemented to be able to survey a wide parameter space with multiple dimensions in a manageable time frame.

STAGE I

A Monte Carlo technique is implemented using MATLAB to screen broad ranges of values for each of the six unknown parameters. The full MATLAB code for this approach is provided in Appendix B.1. The model described above is solved using a restricted range of randomly generated parameters for R_0, k_{dis}, k_{rdp}, k_{cgl}, k_{det}, and k_{pitm}. The upper and lower bounds for each parameter were based on literature data from Ref. [66]. This restricted the model parameters to values in a reasonable range. The procedure and values for the random number generator using MATLAB is in Lines 20-33 in Section B.1. For each data set, the model is solved using a modified ordinary differential equation solver and compared to a desired set of experimental values using the goodness of fit analysis, Equation 3.14. To reduce the computation time, I modified MATLAB's ode15s solver to have a time limit to solve one run of

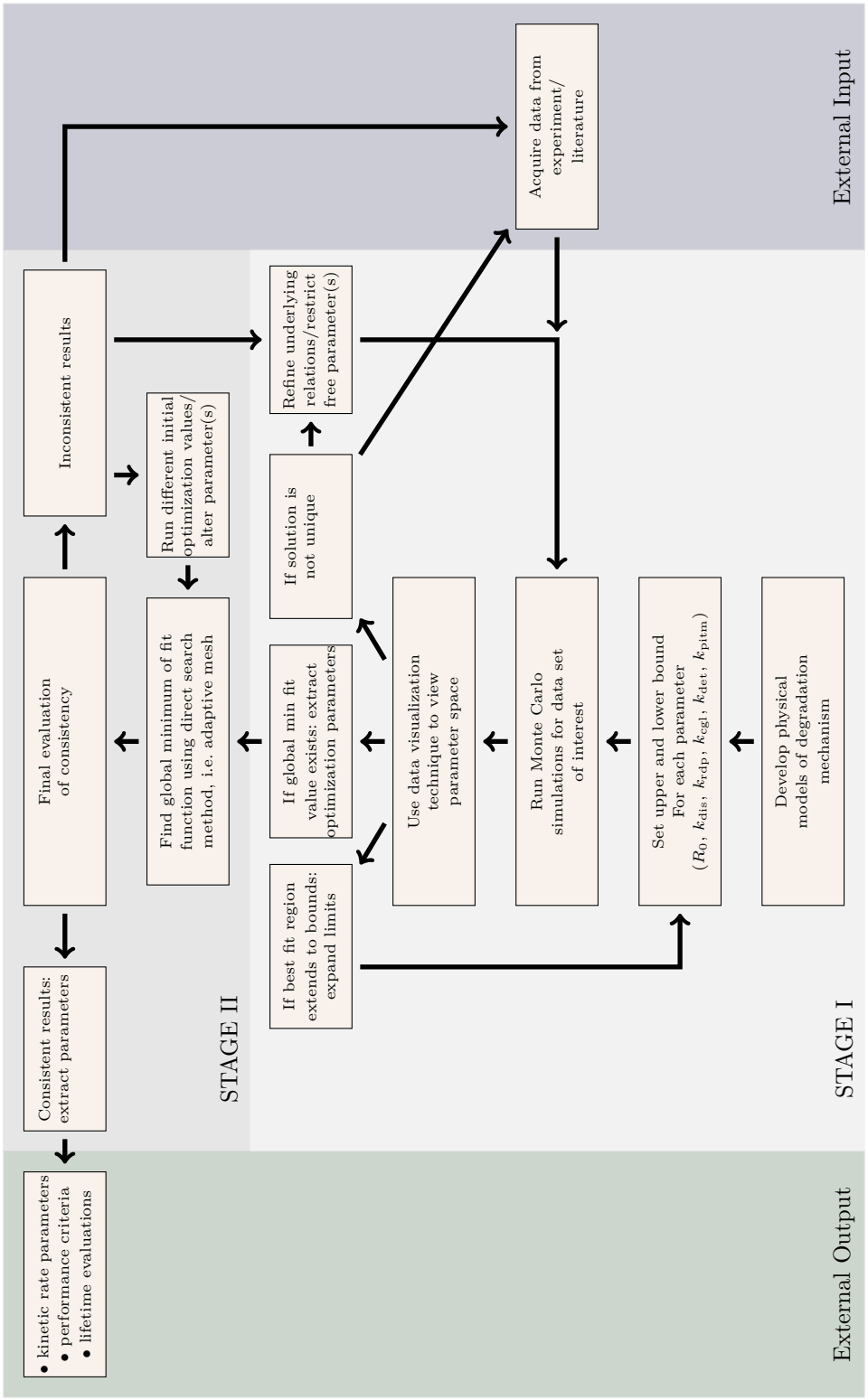

Figure 3.1: Flowchart for algorithm employed in degradation analytics.

the model. Since the primary value of the Monte Carlo procedure is to create a large number of results, if the solver takes exceptionally long on one run, the modified ode solver will end the current run and begin the next parameter set. This process is repeated between five thousand and twenty thousand times. This results in thousands of parameter sets that corresponded to a goodness of fit value; thus the correlation of parameters with the best fit can be visualized. For example, Figure 3.2, shows the relationship of the dissolution rate constant and the characteristic radius, which relates to the surface tension, to the goodness of fit when comparing to MSAC 1.0 V_{RHE} model results. Since there is a known trend, using this visualization a parameter set or area can be pinpointed as a reasonable initial input value. This technique eliminates statistical outliers and identifies the region of a global minimum opposed to local minima. The output of STAGE I is a parameter set for the region around the global minimum, which serves as input for STAGE II of the optimization.

As illustrated in Figure 3.1, our approach prescribes three courses of action if the best fit region is not fully resolved: i) if there is a significant number of best-fit points condensed near a boundary, the limits of parameter ranges must be expanded and the Monte Carlo method must be re-run, ii) more experimental data needs to be accumulated for a better outcome of the Monte-Carlo based analysis or, iii) the underlying modelling framework may require refinement.

STAGE II

Now that we have identified the area of the global minimum, we can use a numerical optimization routine to refine the results. This code is provided in Section B.2 of Appendix B. The extracted parameter set from STAGE I is used as input for the optimization routine. This not only reduces the computational time but refines the results from STAGE I. Unique solutions for the rate constants are obtained with a direct search method that uses the same equation (Equation 3.14) to minimize the mean square deviation between model predictions and experimental data as in STAGE I. The results presented here were all determined using the patternsearch function available in MATLAB and shown in Line 23 of Section B.2. Upon completion of the optimization, the final evaluation of consistency is performed based on literature values and outputs of previous runs. For example, Ref. [66] determined an R_0 value of 10 nm for ϕ_{UPL} near 1.0 V_{RHE}. Thus a narrow region of points around a global minima with associated goodness of fit can be extracted from plots such as in Figure 3.2 and tested for optimization; the six parameters that correlate to a desired single point

from the plot were used as start values for the optimization routine where R_0 was held constant while the other five parameters (k_{dis}, k_{rdp}, k_{cgl}, k_{det}, k_{pitm}) were allowed to vary. Reducing the number of free parameters decreases the computational time. The results are analyzed for goodness of fit to the experimental data set, parametric trends between other model runs, and relativeness to literature values. If the results are consistent, a breakdown of degradation contributions can be conducted. Moreover, predictions can be made on the impact of varying operation conditions and cycles, as well as prospects of various materials modifications and design strategies.

If the final results are inconsistent, several steps can be repeated. The first step would be to rerun the optimization with a different set of start values. The underlying modelling framework could also be modified; one or more of the parameters could be held constant to reduce the dimensions of the model provided there is confidence in the held values. Acquiring more experimental data could also aid in honing a unique parameter set.

3.3 Results and Discussion

3.3.1 Experimental Data Set

Experimental data used in these analyses stem from a comprehensive catalyst degradation study at Ballard Power Systems, published as a DOE report in 2013 [33]. The platinum degradation experiments were performed *in situ* for an operating Membrane Electrode Assembly (MEA); experimental studies explored degradation impacts of different ϕ_{UPL} on performance typical for potential cycling experiments and they evaluated different platinum catalyst supports denoted as: Low Surface Area Carbon (LSAC), Medium Surface Area Carbon (MSAC), High Surface Area Carbon (HSAC) as described above in Section 1.2.1.

Although all three supports had the same Pt loading of 0.4 mg cm^{-2}, the beginning of life particle size distribution varied; LSAC had the highest initial mean Pt particle size. For the majority of the experiments, only the initial and final values of $\bar{r}_N$, PITM, and l_{CCL} reduction were recorded. An additional extended experiment was performed on only LSAC with $\phi_{\text{UPL}} = 1.2$ V$_{\text{RHE}}$ that included intermediate points for $\bar{r}_N$ and PITM. For future studies, more dense data sets for all the ϕ_{UPL} for these important degradation metrics would be desired. PITM was measured using Energy-Dispersive X-ray Spectroscopy (EDS) [33]; Scanning electron microscopy (SEM) was used to determine L_{CCL}; as mentioned, the thickness loss was attributed to carbon corrosion,

Operational / structural parameter	Parameter Values
Upper potential limit (ϕ_{UPL}) ($\mathrm{V_{RHE}}$)	0.9, 1.0, 1.1, 1.2, 1.3
Lower potential limit (ϕ_{LPL}) ($\mathrm{V_{RHE}}$)	0.6
Cycling Profile	Square Wave
Hold times	30 s (ϕ_{LPL}) / 60 s (ϕ_{UPL})
Temperature ($\circ$C)	80
Pressure (psig)	5
Relative Humidity	100
Fuel / oxidant	H_2 4450 sccm 20%O_2/N_2 9000 sccm
Cycle number	0, 50, 700, 2100, 4700
Carbon support type	LSAC: low surface area carbon MSAC: medium surface area carbon HSAC: high surface area carbon
Pt loading (mg $\mathrm{cm^{-2}}$)	0.4

Table 3.1: Experimental parameters

which was assumed to correlate directly to the detachment mechanism. The goodness of fit weights W_{e}, W_{r}, and W_{p} in Equation 3.14 were adjusted such that each point had equal weight, e.g. $W_{\mathrm{e}} = 1/(6 \text{ points})$; W_{d} was set to 0.5 for the single point due to the larger experimental uncertainty in L_{CCL} data.

The initial PRD was not determined in the experimental data set analyzed. However, using the mean radius and standard deviation of the initial particle size, the normalized PRD was calculated for each carbon support type by applying a log-normal distribution,

$$f_N(r,0) = \frac{1}{\sigma\sqrt{2\pi}} \exp\left(-\frac{(\ln x - \mu)^2}{2\sigma^2}\right) \tag{3.15}$$

where $\sigma = 0.314$ and $\mu = 0.944$ for LSAC, $\sigma = 0.460$ and $\mu = 0.612$ for MSAC, and $\sigma = 0.323$ and $\mu = 0.478$ for HSAC. Table 3.1 details the experimental parameters used.

3.3.2 Algorithm Implementation

The degradation data from Ref. [33] were analyzed with the algorithm described in Section 3.2.2 and 3.2.2. Figure 3.2 is an example of the results from STAGE I for MSAC at $\phi_{\mathrm{UPL}} = 1.0$ $\mathrm{V_{RHE}}$. The plot illustrates the goodness of fit as determined in Equation 3.14 of the model to the experimental data, exemplified for the plane

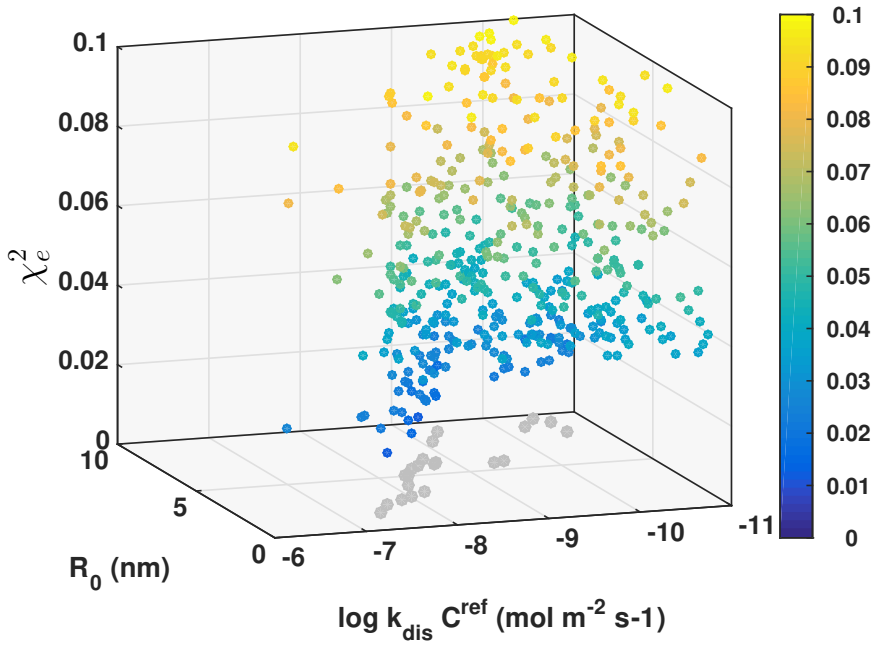

Figure 3.2: Goodness of fit function values (Equation 3.14) for the random sets of parameters sampled with the Monte Carlo method plotted vs. k_{dis} and R_0 for MSAC at 1.0 V_{RHE}. Grey points on the basal plane correspond to projections of the data points with goodness of fit values below the threshold of 3%.

spanned by k_{dis} and R_0. Each point represents a unique parameter set. A correlation between k_{dis} and R_0 is most easily seen in the grey points on the basal plane of Figure 3.2, which corresponds to the data points with the best fit. As seen in Equation 3.5, R_0 is directly proportional to γ_{Pt}. Ideally several model parameters could be determined from independent experiments allowing the free model parameters to be reduced. For instance, knowing the value of γ_{Pt} at specific oxide coverages that correlate to ϕ_{UPL} allows the results to be pinpointed to specific k_{dis} with the best fit value. This work used R_0 values near the reported values corresponding to ϕ_{UPL} in Ref. [65] and [66]. The reader is referred to Ref. [64, 63] for a deeper discussion of surface tension and specific model impacts. It was seen that the radius dependence for the dissolution component of the model equation (Equation 3.1) was relatively stable with changing conditions leading to the assumption that a specific value for surface tension could be used in the model [64]. The corresponding parameter set to any point in Figure 3.2 can be extracted and used as the input for the optimization to minimize the goodness of fit function in STAGE II.

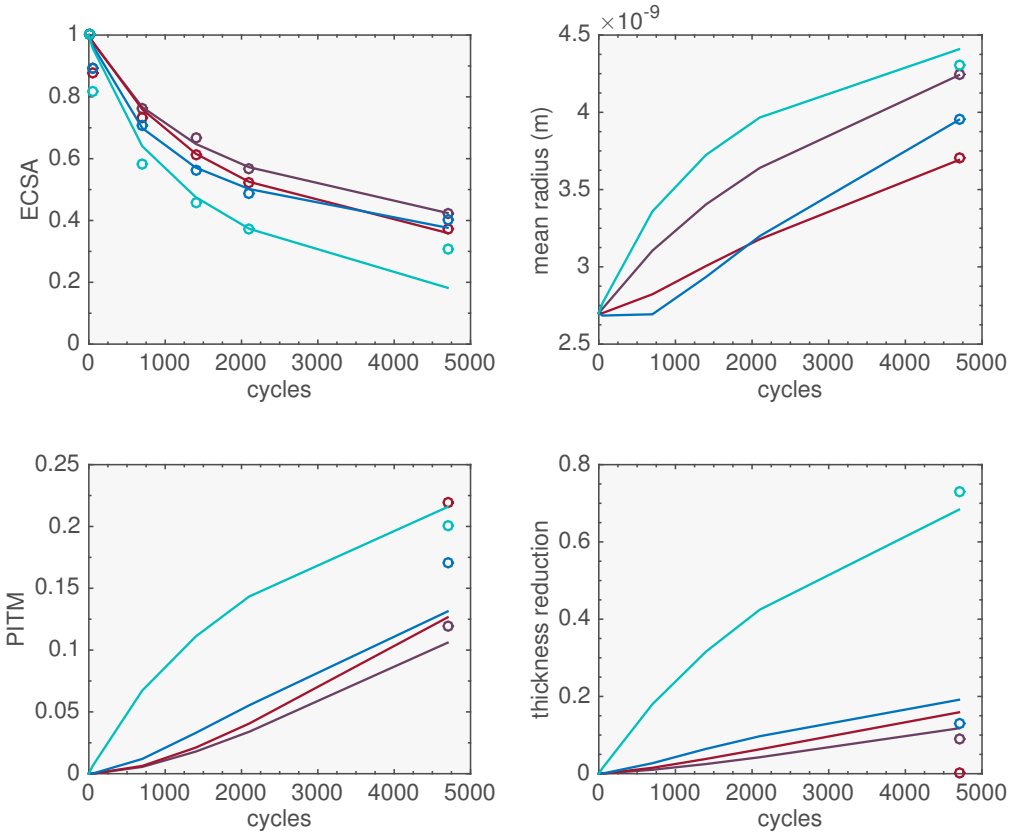

Figure 3.3: Model (line) and experimental data (circles) for Low Surface Area Carbon (LSAC) at different ϕ_{UPL}: 1.0 $\mathrm{V_{RHE}}$ - purple; 1.1 $\mathrm{V_{RHE}}$ - red; 1.2 $\mathrm{V_{RHE}}$ - blue; 1.3 $\mathrm{V_{RHE}}$ - cyan after full parametric optimization according to Figure 3.1.

3.3.3 Model Evaluation

The general expectation across the literature is that overall Pt mass loss due to degradation increases monotonically with ϕ_{UPL} [48, 51, 1, 53, 102, 103]. This model looks to distinguish between the specific mechanisms to further understand the degradation phenomenon. The best-fit results from the model for LSAC, MSAC, and HSAC reproduce experimental data with reasonable accuracy.

For LSAC, there are some unexpected results in the experimental data as seen in Figure 3.3. For instance, there is less S_N loss at $\phi_{\mathrm{UPL}} = 1.2$ $\mathrm{V_{RHE}}$ at 5000 cycles compared to 1.1 $\mathrm{V_{RHE}}$. The experimental results show that the $\bar{r}_N$ after 5000 cycles for $\phi_{\mathrm{UPL}} = 1.0$ $\mathrm{V_{RHE}}$ is nearly equal to that at $\phi_{\mathrm{UPL}} = 1.3$ $\mathrm{V_{RHE}}$ and higher than the $\bar{r}_N$ after 5000 cycles for $\phi_{\mathrm{UPL}} = 1.1$ $\mathrm{V_{RHE}}$ and 1.2 $\mathrm{V_{RHE}}$. Notably, the model

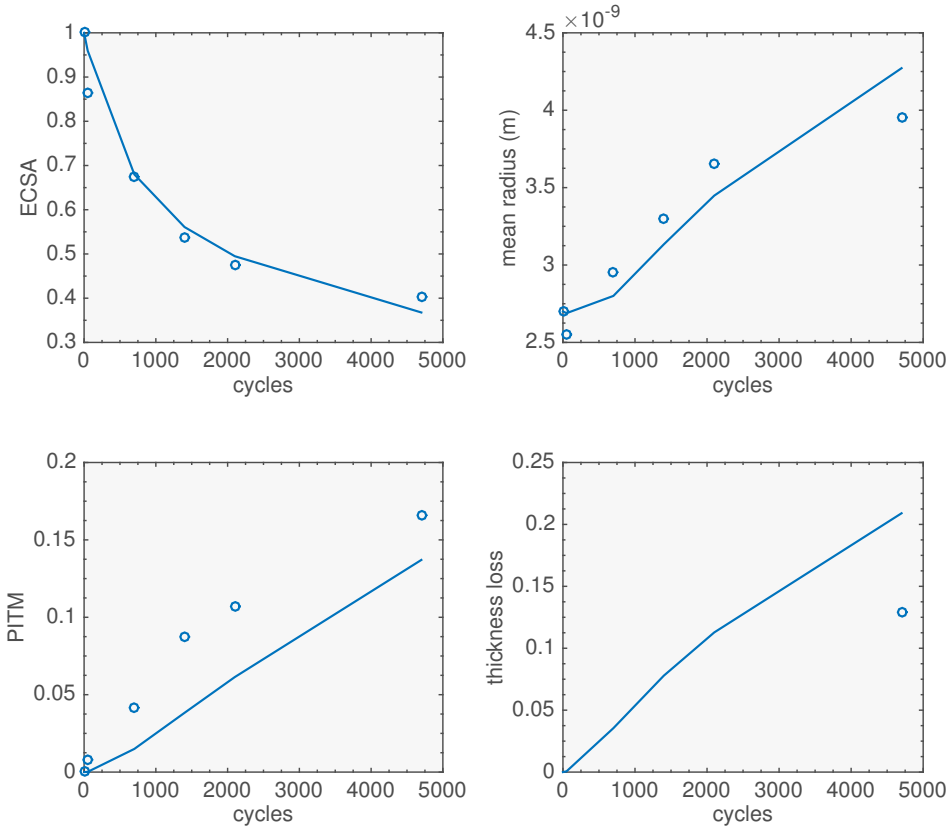

Figure 3.4: Model (line) and experimental data (circles) for Low Surface Area Carbon (LSAC) after full optimization of parameters at $\phi_{\mathrm{UPL}} = 1.2\ \mathrm{V_{RHE}}$ for the additional set of experimental data that included intermediate values of mean radius and PITM; parameters are shown in Table A.1 in the row labelled with a [*].

shows a stable initial $\bar{r}_N$ for $\phi_{\mathrm{UPL}} = 1.2$ $\mathrm{V_{RHE}}$ that exceeds that at $\phi_{\mathrm{UPL}} = 1.1$ $\mathrm{V_{RHE}}$ around 2000 cycles seen in Figure 3.3; this is not seen in the additional experiment performed for $\phi_{\mathrm{UPL}} = 1.2$ $\mathrm{V_{RHE}}$ as shown in Figure 3.4. The model does not capture the increased amount of M_{pitm} reported for $\phi_{\mathrm{UPL}} = 1.1$ $\mathrm{V_{RHE}}$ compared to the other ϕ_{UPL} in the lower left quadrant of Figure 3.3 nor the greater l_{CCL} reduction seen for 1.0 $\mathrm{V_{RHE}}$ compared to 1.1 $\mathrm{V_{RHE}}$; however, it shows expected trends that as the ϕ_{UPL} is increased, M_{pitm} increases and l_{CCL} decreases. More experimental data will be needed to determine if these variations in experimental data are due to experimental artifacts or are reproducible results.

Despite the non-monotonic trends in the experimental data of LSAC, the optimized rate constants do show consistent trends with ϕ_{UPL} displayed in Figure 3.5. The rate constant of detachment, k_{det}, was allowed to vary in STAGE I but during STAGE II the goodness of fit was equal to or less for $\phi_{\mathrm{UPL}} < 1.2$ $\mathrm{V_{RHE}}$ when k_{det} was set to zero; for $\phi_{\mathrm{UPL}} \geq 1.2$ $\mathrm{V_{RHE}}$, a monotonic trend is seen with k_{det}. The dissolution rate constant, k_{dis}, increases until $\phi_{\mathrm{UPL}} = 1.2$ $\mathrm{V_{RHE}}$, above which it exhibits a substantial decrease. Overall at $\phi_{\mathrm{UPL}} = 1.3$ $\mathrm{V_{RHE}}$ the most significant degradation is observed in Figure 3.3, with the greatest decrease in S_N and l_{CCL} and the largest increase in $\bar{r}_N$ and M_{pitm}. Although there is a decrease in k_{dis} and k_{rdp} from $\phi_{\mathrm{UPL}} = 1.2$ $\mathrm{V_{RHE}}$ to 1.3 $\mathrm{V_{RHE}}$, the values of k_{cgl}, k_{det}, and k_{pitm} are significantly increased leading to the highest overall amount of degradation seen. The results of model fitting show an increased k_{cgl}, as seen in Figure 3.5, for $\phi_{\mathrm{UPL}} = 1.0$ $\mathrm{V_{RHE}}$ compared to 1.1 $\mathrm{V_{RHE}}$ and 1.2 $\mathrm{V_{RHE}}$; this non-monotonic trend needs to be further explored with additional data sets.

The experimental data for MSAC in Figure 3.6 show a monotonic trend with increasing ϕ_{UPL}; there is also a higher signal-to-noise ratio which could allow the model to better resolve the data compared to LSAC. The optimized rate constants k_{dis}, k_{cgl}, and k_{det} from the fitting of MSAC data (Figure 3.7) show fairly consistent, monotonic trends with ϕ_{UPL}. Neither the data nor the derived rate constants show monotonic trends for PITM or redeposition. Additional experimental data at intermediate cycle numbers would help resolve ambiguities in the derived rate constants.

Experimental data for HSAC were limited to $\phi_{\mathrm{UPL}} = 1.2$ $\mathrm{V_{RHE}}$. Therefore, parameters could not be compared for different UPLs nor a broad comparison between supports. The best fit solutions and parameter values are shown in Figure 3.8 and in Table A.3 of the supporting information. Figure 3.9 shows the best fit of k_{dis} and k_{det} for the studied carbon support type at $\phi_{\mathrm{UPL}} = 1.2$ $\mathrm{V_{RHE}}$. Generally, k_{dis} exhibits a modest variation across all carbon support types. There is a strong increase in k_{det}

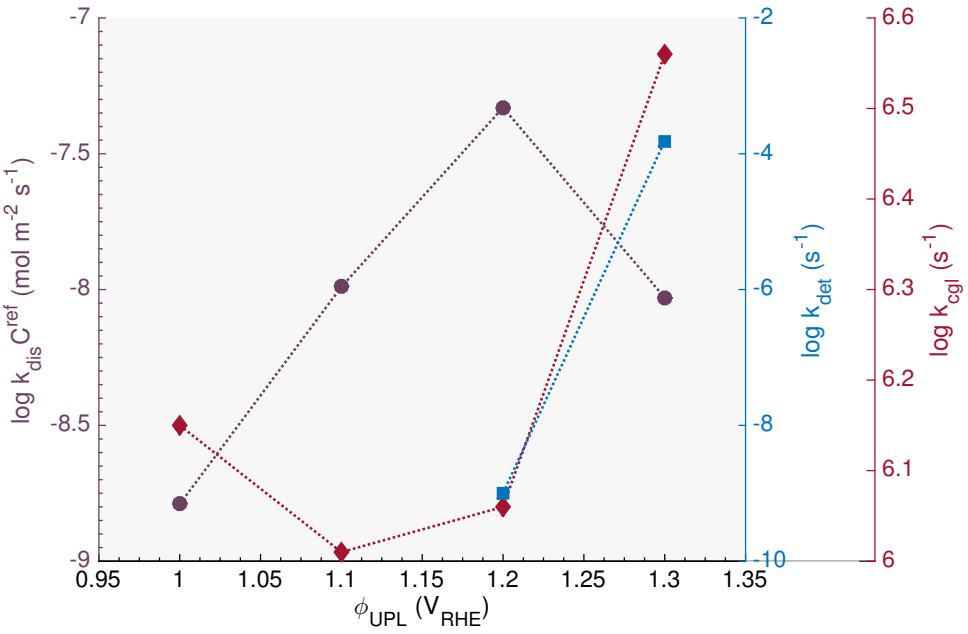

Figure 3.5: Optimized best fit model results for k_{dis} (circles), k_{cgl} (diamonds), and k_{det} (squares) for LSAC at 80° C from Table A.1 in the Supporting Information.

between LSAC and MSAC but not as strong for k_{cgl}. This shows that MSAC is less corrosion resistant compared to LSAC but the Pt particles are still bonding relatively strongly to the support inhibiting the merging of particles. On the other hand, there is a strong increase in between MSAC to HSAC showing that HSAC is neither carbon corrosion resistant nor has strong particle bonding properties relative to LSAC or MSAC.

The relative contribution of the individual degradation mechanism can be compared using an approach developed in Ref. [47]. The impact of each mechanism on the PRD is given by

$$\frac{\partial f_N^{\text{dis}}}{\partial t} = -\frac{\partial}{\partial r}\left[f_N \frac{dr}{dt}\right], \tag{3.16}$$

$$\frac{\partial f_N^{\text{cgl}}}{\partial t} = J^+ - J^-, \tag{3.17}$$

and

$$\frac{\partial f_N^{\text{det}}}{\partial t} = k_{det} f_N. \tag{3.18}$$

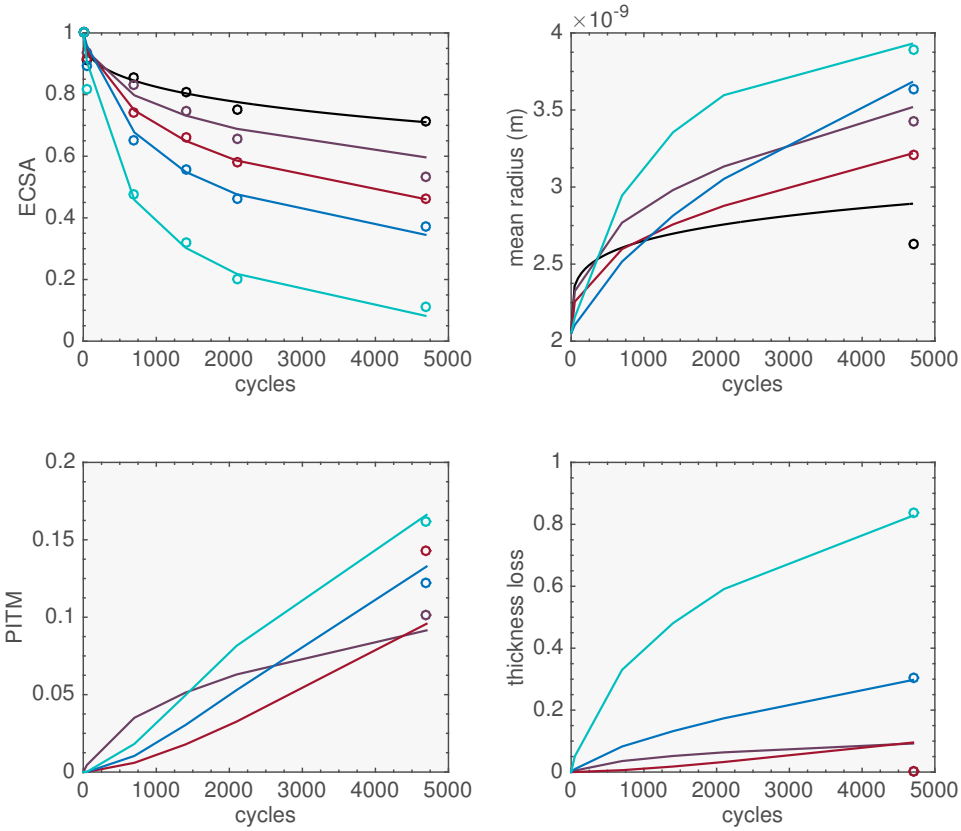

Figure 3.6: Model (line) and experimental data (circles) for Medium Surface Area Carbon (MSAC) after full optimization according to the algorithm in Figure 3.1 at varying ϕ_{UPL}: 0.9 V_{RHE} - black; 1.0 V_{RHE} - purple; 1.1 V_{RHE} - red; 1.2 V_{RHE} - blue; 1.3 V_{RHE} - cyan. A reduced model only considering the dissolution/redeposition mechanism was applied to 0.9 V_{RHE} with the parameters reported in Table A.2 for the row labeled with a [*].

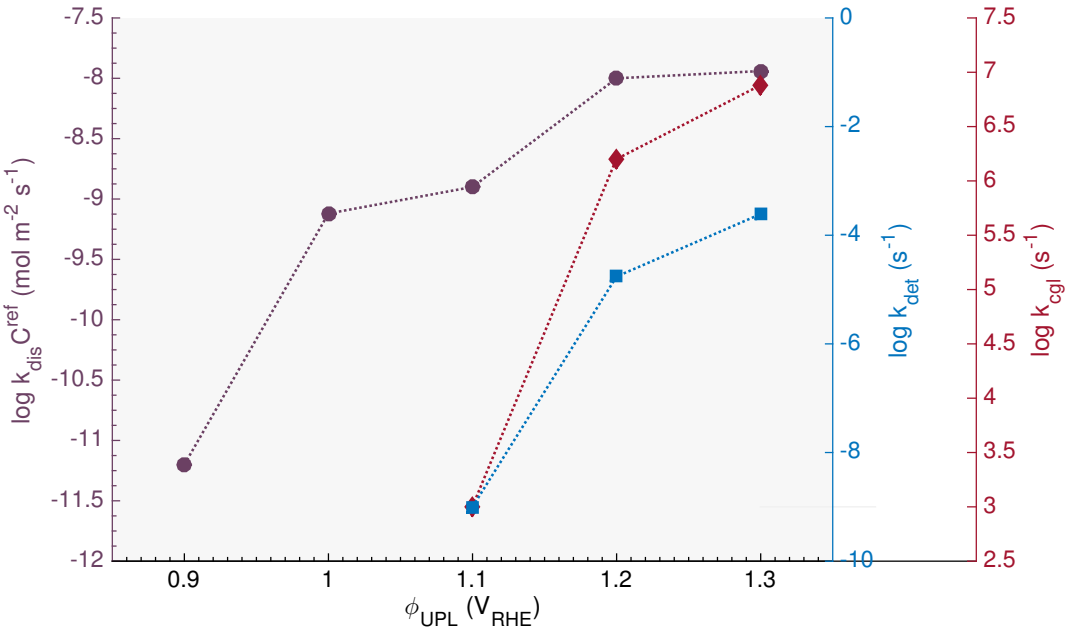

Figure 3.7: Optimized model results for k_{dis} (circles), k_{cgl} (diamonds), and k_{det} (squares) for MSAC at 80° C from Table A.2 in the Supporting Information.

From these, the degradation contributions to ECSA loss from each mechanism can be determined using Equation 3.10.

Figure 3.10 and Figure 3.11 show the breakdown of different mechanistic contributions to the overall ECSA loss at different ϕ_{UPL} for LSAC and MSAC respectively. For LSAC at $\phi_{\text{UPL}} = 1.0$ V_{RHE} dissolution/redeposition/PITM and coagulation are the dominant mechanisms of degradation and coincidentally contribute equivalently. No contribution to ECSA loss is seen with coagulation for MSAC which is consistent with Ref. [66]. Coagulation was reported to be the dominant mechanism in Ref. [47] for one set of initial parameters for both triangle wave and square wave data. There is no contribution from particle detachment for $\phi_{\text{UPL}} = 1.0$ V_{RHE}, which is consistent with the results in Ref. [47] for all four data sets at $\phi_{\text{UPL}} = 0.9$ V_{RHE}. It is a surprising result that LSAC shows contributions from the coagulation mechanism at $\phi_{\text{UPL}} = 1.0$ V_{RHE} but MSAC does not; further experimental data are needed in order to conclude if the structure of the support alone could lead to a reduction of the coagulation mechanism. Since the High Surface Area Carbon (HSAC) data was limited, a mechanistic breakdown could not be performed for comparison.

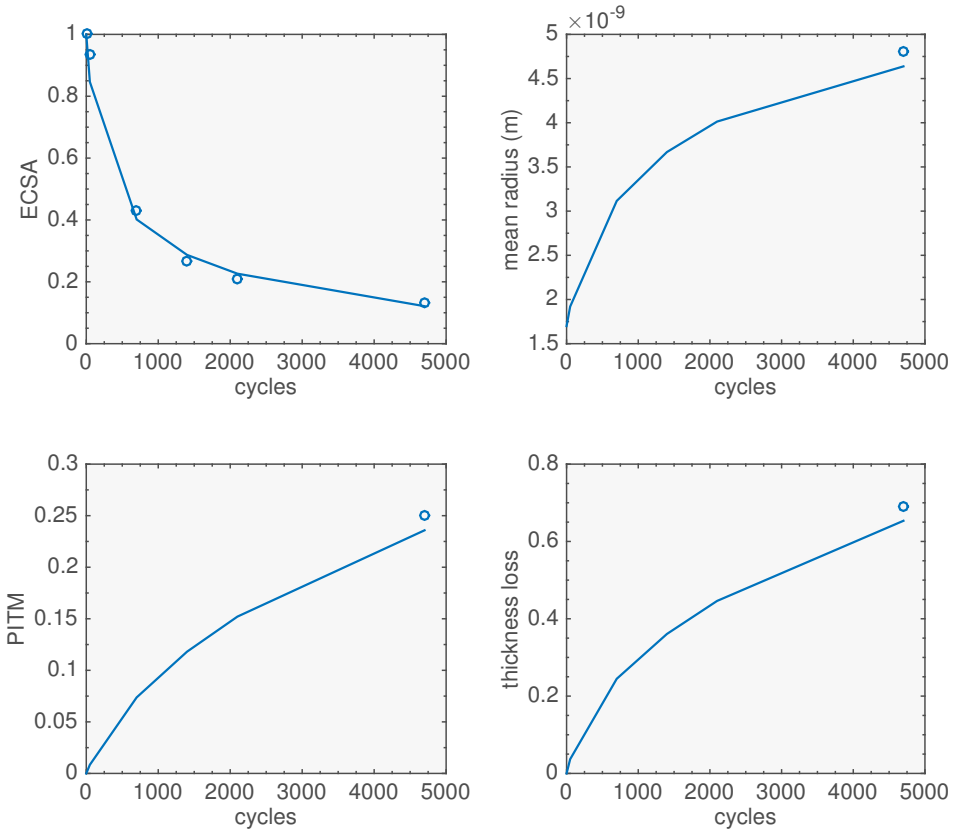

Figure 3.8: Model (line) and experimental data (circles) for High Surface Area Carbon (HSAC) after full optimization with the algorithm in Figure 3.1 at upper potential limit of 1.2 V_{RHE} with the parameters reported in Table A.3.

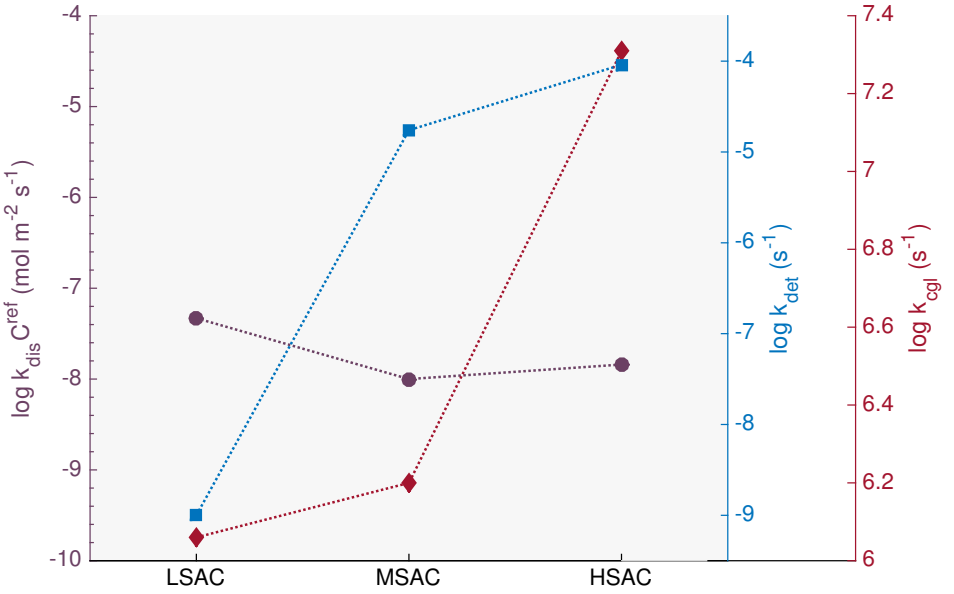

Figure 3.9: Comparison of the trends in catalyst dissolution rate (purple circles), the rate of detachment (blue squares), and the rate of coagulation (red diamonds) for Low Surface Area Carbon (LSAC), Medium Surface Area Carbon (MSAC), and High Surface Area Carbon (HSAC) at an upper potential cycling limit equal to 1.2 V_{RHE}.

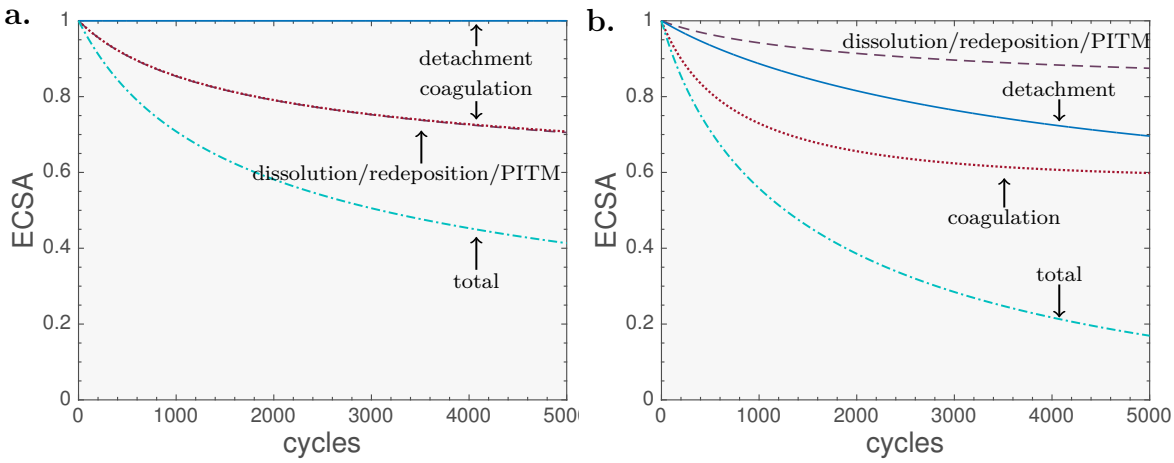

Figure 3.10: Mechanistic breakdown for LSAC at ϕ_{UPL} of a.) 1.0 V_{RHE} and b.) 1.3 V_{RHE}.

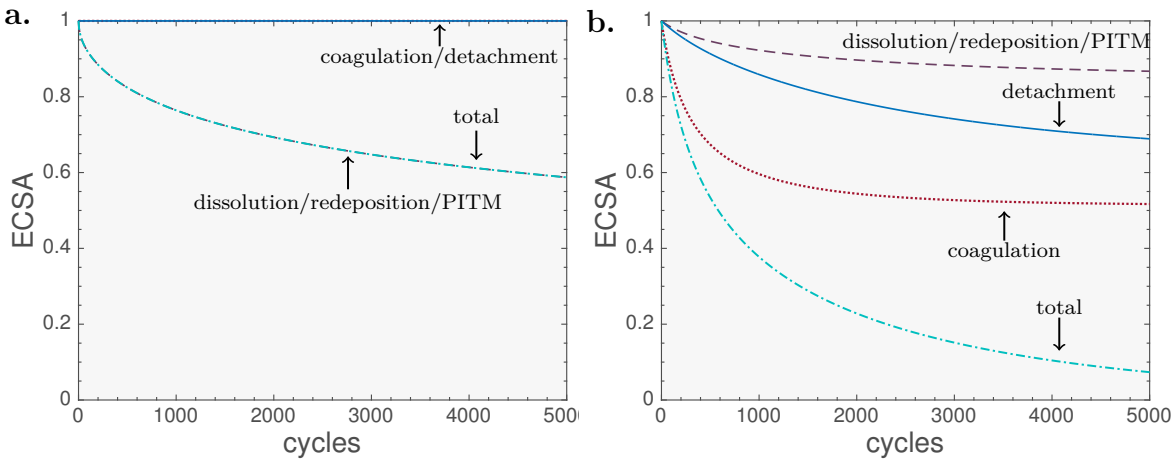

Figure 3.11: Mechanistic breakdown for MSAC at ϕ_{UPL} of a.) 1.0 V_{RHE} and b.) 1.3 V_{RHE}.

3.4 Summary of Results

This chapter presented a step-wise algorithm to analyze catalyst degradation data to extract rate parameters that are essential for detailed mechanistic understanding of platinum degradation. Unique, unambiguous rate parameters for individual mechanisms of degradation have been extracted from experimental data. This was achieved by simultaneously fitting ECSA loss, mean particle radius, PITM loss, and catalyst layer thickness loss. In general, the derived rate constants for dissolution and detachment increase with ϕ_{UPL}. The detachment rate constant increases with the surface area of the carbon support whereas the dissolution rate constant appears to be independent of the support.

Knowing the individual rate constants under various cycling protocols shows the degradation mechanism that dominates at specific conditions, as well as at which point during the cycling the individual mechanism contributes to platinum loss. For instance, detachment was not seen to play a predominant role while cycling the potential below 1.0 V_{RHE} correlating to no carbon corrosion at lower potentials. The understanding gained by the presented model gives catalyst layer manufacturers benchmarks such that catalyst layers can be better optimized, e.g., either designed towards more stable catalyst or more stable supports. Ideally this model will be applied to vast amounts of data to refine the model in order to allow for accurate predictive capabilities.

Now that we have a process to predict degradation rates, we look to understand the underlying relations that cause the degradation. In the next chapters a model of platinum oxide formation, growth, and reduction is presented. The model is first solved for only oxide formation and growth in the quasi steady-state limit then the reduction mechanism is added. Ideally, the dissolution rate constant for this model, will be obtained from the oxide formation, growth, and reduction model that will be discussed in the upcoming chapters, which would reduce the number of free parameter inputs ultimately saving computational time.

Chapter 4

Modelling Oxide Formation, Growth, and Reduction of Platinum

4.1 Introduction

The connection between platinum dissolution and oxide growth and reduction was outlined in Chapter 2 where an overview of the significant literature studies that pertain to these phenomena were discussed. Many factors contribute to the degree of growth and reduction of metal oxides. Some metals, such as iron, will easily oxidize in mild conditions without a protective coating. But even robust metals such as platinum will oxidize under harsh environmental conditions. In a fuel cell, the platinum metal catalyst is exposed to continuously varying potentials, high temperatures, acidic surroundings, and oxygen exposure through both liquid and gas creating an oxidizing environment. This oxidation disrupts the orderly structure of the platinum resulting in enhanced degradation and overall loss in power density and lifetime but there are still debates on the exact reactions causing this loss. In the previous chapter we looked at rates of different degradation mechanisms. Here we take steps at understanding underlying kinetics and processes leading to dissolution. The goal is to be able to use results from the degradation model discussed in the previous chapter as parameter inputs to a model of oxide growth and reduction to predict the degree of platinum degradation attributed to the platinum oxidation and reduction process. First the phenomenology of the oxide growth and reduction process is discussed and then a model is developed and solved.

4.2 Phenomenology of Oxide Formation, Growth, and Reduction

As we saw in Section 2.2, several experimental methods reveal a plethora of information regarding the surface science of platinum oxides. We dive into greater detail regarding the process of the oxide growth and reduction in order to have a solid foundation to build a model on. Here we discuss the oxide growth and reduction resulting from an applied potential as in Figure 2.3. Hydrogen is adsorbed as the potential is decreased from just below 0.5 V_{RHE} to 0 V_{RHE} and then desorbed off the platinum electrode as the applied potential is increased; at around 0.4 V_{RHE}, the surface transitions to the adsorbate-free double layer charging region indicated by the region with no peaks on the cyclic voltammetry scan as highlighted in Figure 2.3. Many AST cycling protocols use a Lower Potential Limit (LPL) in this region to avoid the adsorption and desorption of hydrogen when studying the oxidation process.

The electrode remains clean while the electrode potential is increasing (or decreasing) throughout the double layer charging region until oxygen atoms begin to chemisorb on the surface. Oxygen atoms continue to be attracted to the platinum surface until it becomes energetically favourable for platinum atoms to be dislodged from their metal lattice position at the surface creating a buckling effect [104]. At sufficiently high surface oxygen coverage, this buckling creates a defect that opens a space for an oxygen atom to fill [99, 105, 106]. It is this defect creation process that spawns the oxide growth. The replacement of a surface platinum atom with an oxygen atom in the buckling process is often known as place-exchange. The oxide layer will continue to grow thicker as the applied potential is increased [107]. Initially the oxide layer forms a Pt-O structure but there is evidence at higher potentials of the formation of a bilayer oxide structure [96, 3, 108, 109].

A schematic of the oxidation process is depicted in Figure 4.1. Figure 4.1a illustrates the formation of oxygen adsorbed on the surface of platinum as a potential is applied. Figure 4.1b represents the PtO layer that forms upon chemisorption of a sufficient amount of oxygen to induce the place exchange mechanism and grow the oxide layer. The oxide layer grows into the metal via Pt atom displacement, as well as into the electrolyte via binding of oxygen ions. The formation of PtO_2 is illustrated in Figure 4.1c.

The oxide layer grows thicker through the migration and diffusion of defects in the form of oxygen ion vacancies or Pt interstitials [69]. The growth of the oxide layer is limited by the rate of defect creation at the Metal-Oxide (M-O) interface [4].

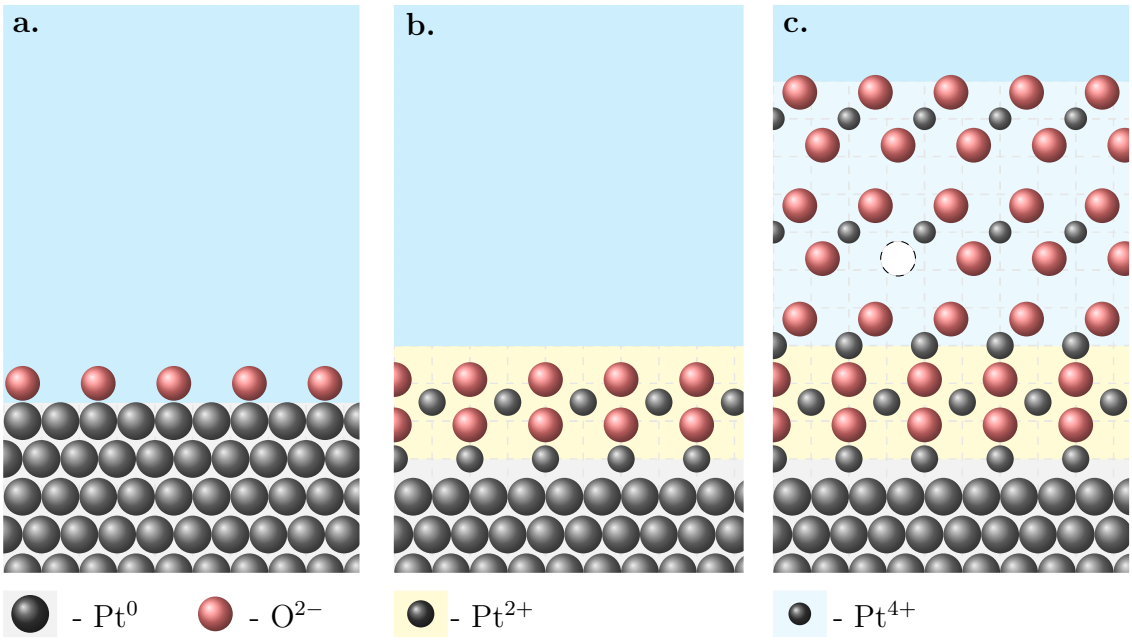

Figure 4.1: Schematic of Pt oxide growth; a.) Oxygen formation on surface; b.) PtO layer formation c.) Bilayer structure of PtO (yellow) and PtO_2 (light blue) with oxygen ion vacancies shown;

The initial Pt-O layer forms as a typical rock salt crystal structure whereas the PtO_2 layer is less defined [110]. The crystalline structures of the oxide relate directly to the semiconducting characteristic of the material and can be determined by calculating the electronic band structure using DFT and ReaxxFF [111, 112]. Both layers are known to exhibit semiconducting properties. Ref. [110] shows evidence that the second layer is α-PtO_2 with the configuration of the CdI_2 crystal structure [110]. In Ref. [112] it is discussed that β-PtO_2 ($CaCI_2$ orthorhombic) had a smaller band gap and was more stable relative to α-PtO_2 (CdI_2). Despite the uncertainty in the exact structure, the PtO_2 layer is seen to grow to several monolayers in thickness, whereas the PtO layer is believed to only grow to an average of two monolayers in the case of Pt(poly); this limit could be different in the case of Pt(hkl) electrodes [68].

One hypothesis for the bilayer structure of PtO and PtO_2 is lattice matching: it is more energetically favourable for Pt oxide to be in the PtO_2 structure but this cannot reside directly on pure Pt metal. Thus an intermediate layer, such as the PtO layer, is needed between the two layers [97]. However, the formation of the PtO layer could also just be a transient phenomenon.

The oxide layer will grow until the potential is negative enough for a chemisorbed oxygen species to release from the oxide layer creating an oxygen vacancy defect

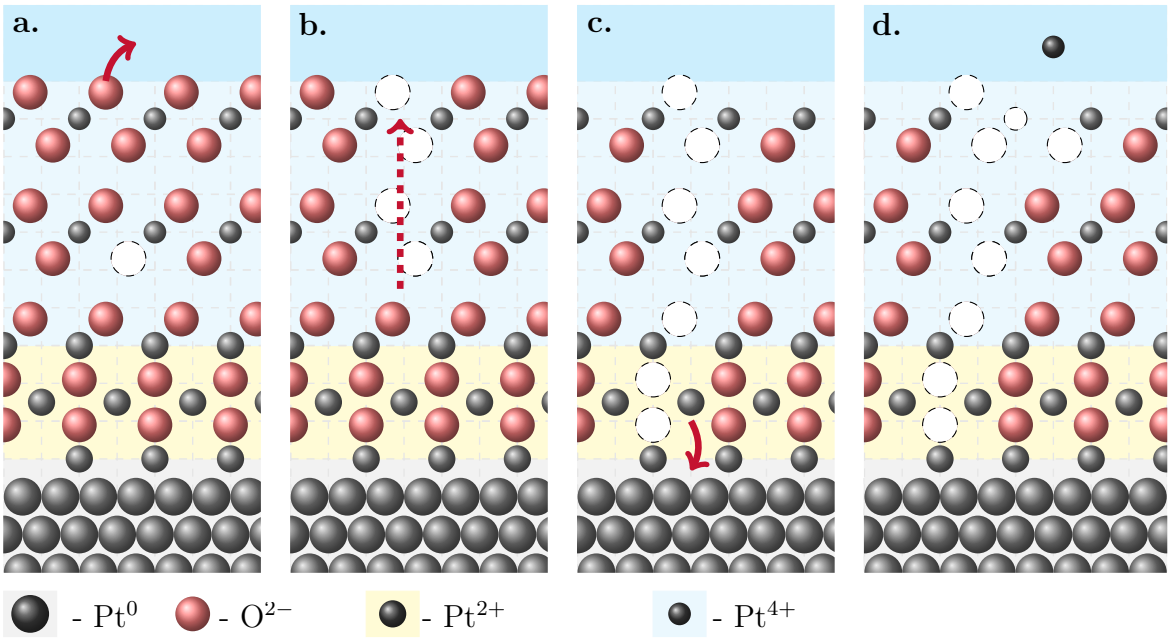

Figure 4.2: General schematic of the oxide reduction process: a.) defect creation; b.) diffusion; c.) Pt filling; d.) Pt dissolution

at the Oxide-Electrolyte (O-E) interface triggering the reduction reaction as shown in Figure 4.2a [113, 114]. The initiation potential of the reduction process depends on the thickness of the oxide layer, which in turn is determined by the UPL, hold times, and/or experimental conditions; the thicker the oxide layer, the lower the potential needed to promote the reduction process [115]. The reduction reaction can only proceed as fast as the vacancies at the surface are created. Then the oxygen atoms can migrate towards the O-E interface and into the electrolyte resulting in the diffusion of oxygen vacancies towards the bulk metal represented in Figure 4.2b. Once an oxygen vacancy has diffused/migrated through the oxide layer to the Metal-Oxide (M-O) interface, a space is made available for a charged Pt atom in the oxide layer to reunite with the metal and be reduced (Figure 4.2c). The rate of the defect creation will determine the nature of the reduction. For example, if the rate is very fast, the oxygen atoms will escape from the oxide layer much faster than the Pt atoms can return to the bulk leaving under-coordinated platinum atoms that are prone to dissolution (Figure 4.2d). On the other hand, if the rate of defect creation is very slow, there may be a uniform healing and thinning of the entire layer.

The model is developed from the general scheme shown in Figure 4.3 and incorporates the mechanisms of oxide layer growth and reduction based on diffusion and

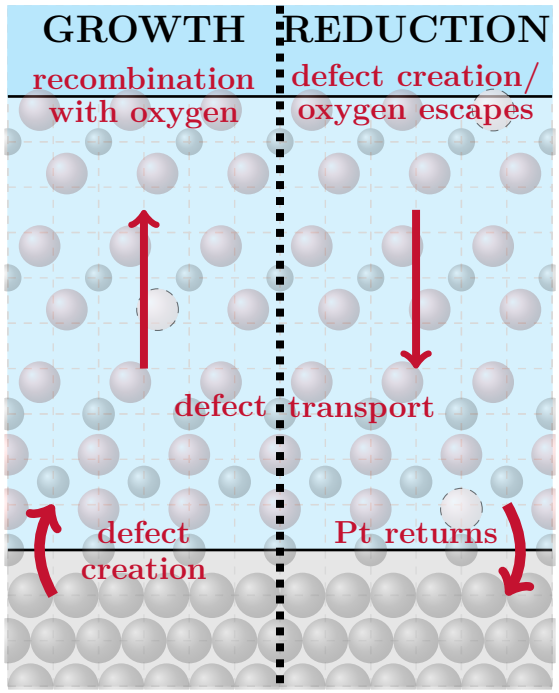

Figure 4.3: Illustration of the boundary condition and oxide growth and reduction processes.

migration of defects. It moreover accounts for the kinetic reactions that occur at the interfaces.

Figure 4.4 shows the corresponding reaction scheme for oxide growth, reduction, and dissolution. The equations incorporate:

1. Oxygen vacancy creation (growth) / annihilation (reduction)
2. Oxygen vacancy annihilation (growth) / creation (reduction)
3. Cation transport through interstitial
4. Dissolution of oxide layer (most significant during reduction - assume negligible during oxide growth due to lack of experimental detection)

Although there are several species transporting across the oxide layer including Pt and O ions, Pt and O defects, and electrons, for modelling purposes, accounting only for the minority species, i.e. the oxygen vacancies, is sufficient. Any movement of oxygen vacancies will result in either a growth or reduction depending on the direction

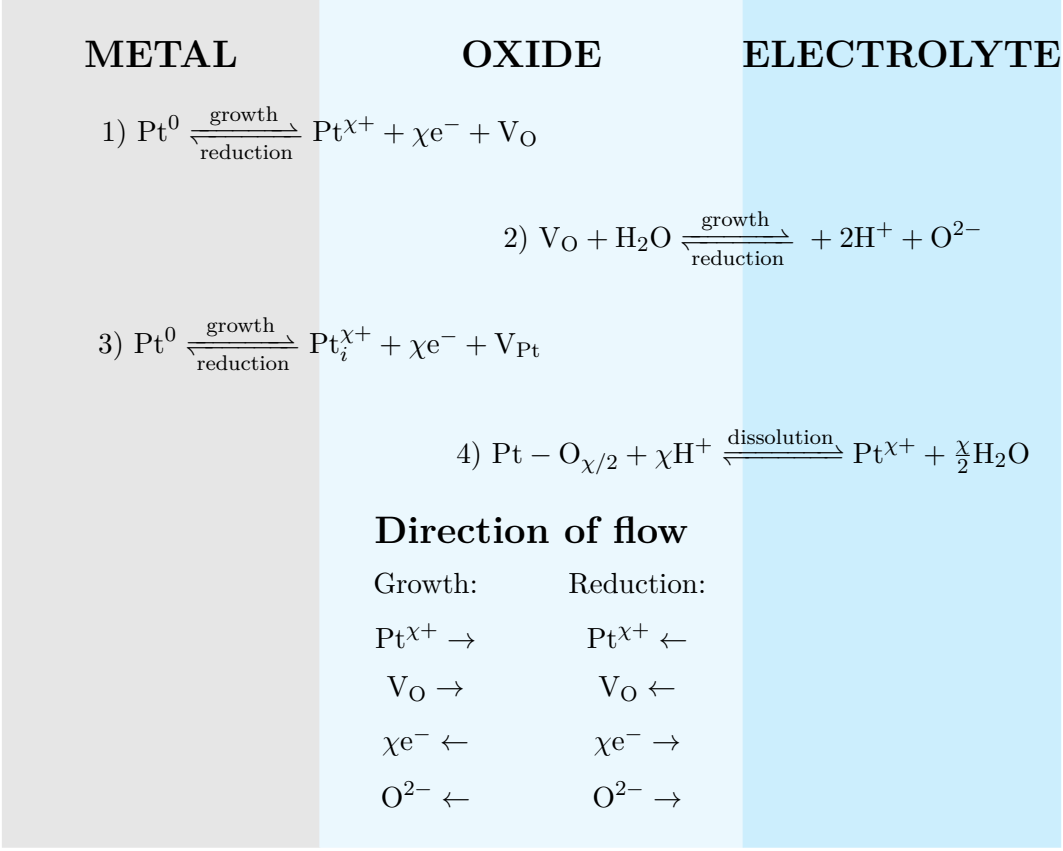

Figure 4.4: Species equations for growth, reduction, and dissolution

of the flux keeping in mind there is global charge neutrality. It is assumed the flux of the Pt interstitial defects through the lattice does not contribute to the growth or reduction of the oxide layer and thus Reaction 3 in Figure 4.4 is not considered initially in the model development.

4.3 Model Structure

For the purposes of our model, we assume an interface between the metal and oxide layer at x = 0 and an interface between the electrolyte and the oxide layer at x = L, shown in Figure 4.3. Our model does not account for the formation of a bilayer structure, but the geometry of the oxide layer is included in model parameters, such as the reaction rate and the expansion factor, which can be adapted for different structures or analyzed to determine probable oxide structures. The general assumptions of the model include: (i) the oxygen vacancy density is small; the ratio of the oxygen vacancy to total oxygen ranges from a fraction of a percent to several percent [69],

(ii) overall-homogenous composition across the film [116], (iii) a PtO oxide structure, (iv) an isothermal system, and (v) we only consider the x-components of the fluxes, i.e. 1D model.

Concerning the thickness regime, the model should allow for a consistent treatment of the transition from thin to thick oxide layer, as an effective interpolation scheme. In the limit of a thin oxide layer, the kinetics and structural sensitivity of the defect creation process at the interface controls the growth. In the limit of a thick oxide layer, diffusion and migration of species in the oxide layer will determine the growth rate. We employ a continuum transport model based on Poisson-Nernst-Planck equation for the latter case. Of course, this approach fails when the oxide layer is thin. However, since transport effects in the layer are insignificant in this thickness regime, the use of the continuum description remains without any impact.

Oxygen ion vacancies are generated at the M-O interface by the extraction of Pt atoms during growth. The rate of this process depends on the local composition of the interface, i.e., the amount of oxygen species, and the structure of the oxide. These aspects determine the local electric field and thus the energetics of the extraction process. The structural sensitivity of the rate of Pt atom extraction and of the simultaneous production of oxygen ion vacancies was studied in Ref. [105]. The challenge for oxide growth models is to cast these dependencies into a suitable mathematical form. The proposed functional relation will be discussed in Section 4.4.1. It represents a crucial component of our model.

4.4 Model Equations

We assume that transport in through-plane direction is dominant and transport in other directions is neglected reducing the model to one dimension. The continuity equation for oxygen ion vacancies is

$$\frac{\partial C(x,t)}{\partial t} = -\frac{\partial J(x,t)}{\partial x}, \tag{4.1}$$

where C is the oxygen ion vacancy concentration in the oxide layer, J denotes the flux, x is the position across the layer, and t time. The flux of the oxygen ion vacancies is described by the Nernst-Planck relation,

$$J(x,t) = -D\left(\frac{\partial C(x,t)}{\partial x} + \frac{zF}{RT}C(x,t)\frac{\partial \phi(x,t)}{\partial x}\right), \tag{4.2}$$

where D is the diffusion coefficient; F Faraday constant, R ideal gas constant, and T temperature. The charge number is denoted by z and ϕ is the electrostatic potential. Diffusion and migration contribute to oxygen ion vacancy flux across the layer facilitating the growth of the oxide layer. The Poisson equation accounts for the electric potential across the oxide layer for a given charge density, ρ,

$$\frac{\partial^2 \phi}{\partial x^2} = -\frac{\rho(x,t)}{\epsilon_0 \epsilon_r} \tag{4.3}$$

where

$$\rho(x,t) = zFC(x,t), \tag{4.4}$$

and ϵ_0 is the permittivity constant in a vacuum and ϵ_r the relative permittivity of platinum oxide. For the oxide system we consider charge contributions from oxygen vacancies. Figure 4.5 is a general schematic of the potential profile across the oxide layer. The electric field strength can be determined using

$$E(x,t) = -\frac{\partial \phi(x,t)}{\partial x}. \tag{4.5}$$

The current density as described by Cohen and Cooley [117] is,

$$I(x,t) = F \sum zJ(x,t) + \epsilon_0 \epsilon_r \frac{\partial E(x,t)}{\partial t} \tag{4.6}$$

with the last term being the displacement current. Equation 4.2 is combined with Equation 4.1 and Equation 4.5,

$$\frac{\partial C(x,t)}{\partial t} = D\frac{\partial^2 C(x,t)}{\partial x^2} - \frac{zFD}{RT}\frac{\partial C(x,t)}{\partial x}E(x,t). \tag{4.7}$$

The kinetic rate of the reaction at the M-O interface can be used to describe oxide growth or reduction over time,

$$\frac{dL(t)}{dt} = \kappa f_{1f} C(x) - \kappa_r f_{1r} C(x)|_{x=0}. \tag{4.8}$$

where f_{1f} and f_{1r} are the forward and reverse of the interfacial functions across the M-O interface and will be described in detail in the next section. The corresponding rate constants are κ for the forward reaction and κ_r for the reverse reaction.

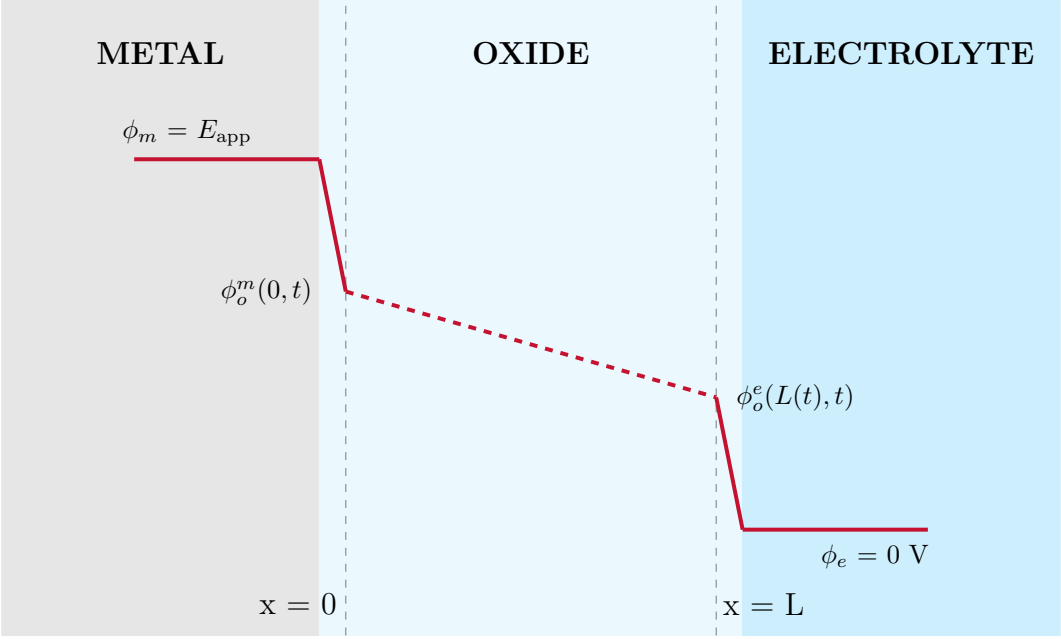

Figure 4.5: General schematic of the potential profile across the layers and boundary values. The dashed red line symbolized the potential distribution across the oxide layer which is not necessarily linear but will be determined using Eq. 4.3.

4.4.1 Interfacial Kinetic Functions

We define four interfacial kinetic functions that are designed to mathematically capture the exchange of species at each interface. Defining kinetic functions at the boundaries allows for a relationship between Pt extraction and oxygen vacancy concentration at the interface to be quantified. At the M-O interface we define the forward interfacial function as f_{1f} and the reverse as f_{1r}. These values are incorporated into the boundary conditions in Section 4.4.2. For the forward reaction, it is clear from the literature that there is a dependence of Pt atom extraction on oxygen coverage [106, 3, 118]. The exact shape of this dependence is unknown. However, we use a functional form that allows us to tune the steepness of the transition, which is related to the sensitivity of the reaction rate of platinum extraction on oxygen coverage. A practical way to incorporate this dependence is to use a tanh function,

$$f_{1f} = \frac{1}{2}\left(1 + \tanh\left(\Gamma\left(1 - \frac{C(0)}{C_0}\right)\right)\right), \tag{4.9}$$

where C_0 is the characteristic oxygen vacancy concentration required to promote Pt extraction. A phenomenological parameter, Γ, is introduced to quantify the sensitivity

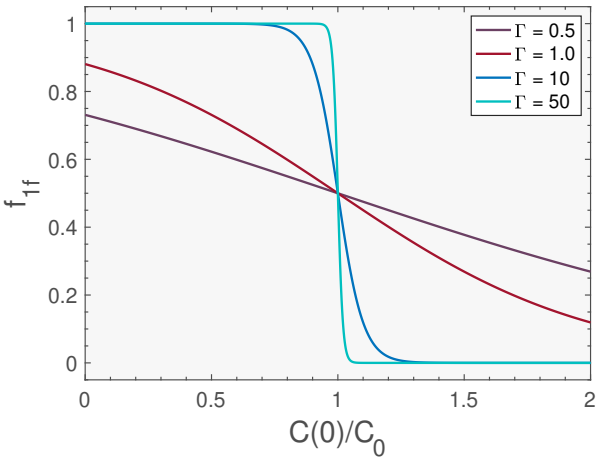

Figure 4.6: The interfacial kinetic function (f_{1f}) as a function of the normalized oxygen ion vacancy density at the M-O interface at varying Γ values.

of the dependence of Pt extraction on $C(0)$. Low Γ values show a gradual linear trend, representing a relatively weak dependence of Pt atom extraction to $C(0)$. A high value of Γ, i.e., $\Gamma \gg 10$, implies a strong step-like dependence. According to results in Ref. [105], the latter is the more realistic scenario. The plot of f_{1f} as a function of $C(0)$ for different Γ is shown in Figure 4.6.

A similar function is used to describe the reverse reaction across the M-O interface, f_{1r}. It is assumed a threshold is also needed to promote the reduction of the oxide,

$$f_{1r} = \frac{1}{2}\left(1 + \tanh\left(\Gamma\left(\frac{C(0)}{C_0} - 1\right)\right)\right), \tag{4.10}$$

which is represented in Figure 4.7. When the oxygen vacancy concentration goes above the threshold, the oxide layer will begin to decrease in thickness, below the threshold, the layer reduction will be slow. It is assumed that the rate limiting steps are the reactions across the M-O interface such that the interfacial functions at the O-E interface can be defined more simply. During growth it is assumed that any vacancy that makes it to the O-E interface will simply be filled at a sufficiently high rate, given by a simple equation is defined as,

$$f_{2f} = \frac{C(L)}{C_0}. \tag{4.11}$$

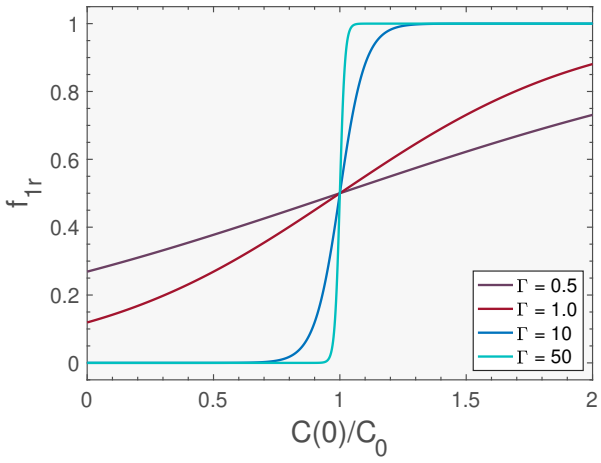

Figure 4.7: The interfacial kinetic function (f_{1r}) as a function of the normalized oxygen ion vacancy density at the M-O interface at varying Γ values.

The reverse reaction at the O-E interface where the reduction phenomena is dominant is dependent on the number of oxygen atoms at the surface,

$$f_{2r} = 1 - \frac{C(L)}{C_0}. \tag{4.12}$$

Equations 4.9 - 4.12 can be adapted to account for different processes that occur at each boundary. Incorporating material-specific kinetic reactions at each boundary is a key part of the model that distinguishes it from oxidation models in the literature.

4.4.2 Flux Boundary Conditions

The boundaries are defined at the M-O interface, shown in Figure 4.3 as $x = 0$, and at the O-E interface, $x = L$. Both boundaries are moving as the oxide grows and reduces; at the M-O interface the boundary shifts into the metal as oxygen species cross the interface during oxide growth. Initially we transform the computational domain to have a static boundary of the oxide layer at $x = 0$. This allows us to mathematically consider only one moving boundary. At $x = 0$ we have,

$$J\Big|_{x=0} = k_{1f} f_{1f}(C(0)) - k_{1r} f_{1r}(C(0)). \tag{4.13}$$

Equation 4.13 defines the rate of extraction of Pt atoms across the M-O interface, as the difference of, the forward reaction with rate constant k_{1f} minus the reverse

reaction of Pt atoms returning to the metal with the rate constant k_{1r}. The dominating rate constant will determine whether the oxide layer is in the growth or reduction phase. At $x = L(t)$, the boundary condition is

$$J\Big|_{x=L} = k_{2f} f_{2f}(C(L)) - k_{2r} f_{2r}(C(L)) \tag{4.14}$$

which defines the flux of oxygen ion vacancies across the O-E interface and corresponds to Reaction 2 in Figure 4.4. The recombination rate constant of an oxygen ion vacancy with an oxygen ion resulting in oxide layer growth is defined as k_{2f} and the creation rate constant of an oxygen ion vacancy by the release of an oxygen ion is k_{2r} resulting in the reduction of the oxide layer.

As shown in Figure 4.4, only reactions across the M-O interface are potential-dependent, i.e., involve an electron transfer. The reaction rates are defined as,

$$k_{1f} = k_{1f}^0 \exp\left(-\frac{\alpha F}{RT}(\phi_{m/o})\right) = k_{1f}^0 \exp\left(-\frac{\alpha F}{RT}(\phi_m - \phi(0))\right), \tag{4.15}$$

and

$$k_{1r} = k_{1r}^0 \exp\left(-\frac{\alpha F}{RT}(\phi_{o/m})\right) = k_{1r}^0 \exp\left(-\frac{\alpha F}{RT}(\phi(0) - \phi_m)\right), \tag{4.16}$$

where k_{1f}^0 and k_{1r}^0 are the forward and reverse rate constants, α the transfer coefficient, $\phi_{m/o}$ the forward potential difference from the metal to oxide at the M-O interface, and $\phi_{o/m}$ the reverse potential difference from the oxide to the metal at the M-O interface. For simplicity, we assume electrochemical kinetics of Butler Volmer-type with $\alpha = 0.5$. This assumption could be relaxed later to account for a multiple electron-transfer reaction or one where the energy transition state favours the reactants ($\alpha > 0.5$) or products ($\alpha < 0.5$) [119]. The reaction rates at the O-E interface are simply equal to their corresponding rate constant,

$$k_{2f} = k_{2f}^0, \tag{4.17}$$

for the forward reaction, and

$$k_{2r} = k_{2r}^0, \tag{4.18}$$

for the reverse reaction.

4.4.3 Potential Boundary Conditions

In order to solve Equation 4.3 we need to define the electric field at $x = 0$ and $x = L(t)$,

$$\left.\frac{\partial\phi(x,t)}{\partial x}\right|_{x=0} = -\frac{\sigma(0)}{\epsilon_r\epsilon_0} \tag{4.19}$$

where σ is the effective charge density at the M-O interface. Originally, we will assume this is a non-zero constant. In the future this assumption could be relaxed into a function of potential and time. At the O-E interface,

$$\left.\frac{\partial\phi(x,t)}{\partial x}\right|_{x=L} = -\frac{\sigma(L(t))}{\epsilon_r\epsilon_0} = 0. \tag{4.20}$$

4.5 Nondimensionalization

In order to simplify the mathematical formalism and determine the number of independent parameters, we nondimensionalize the model equations. This allows for a clear understanding and interpretation of the parametric effects seen in experimental data. We define a dimensionless time,

$$\tau = \frac{Dt}{L_0^2} \tag{4.21}$$

where L_0 is the thickness of a unit cell of the oxide with one layer of oxygen ions. The value of L_0 depends on the geometry of the oxide layer. For α-PtO_2, L_0 is 4.3 Å, and for PtO, L_0 is 2.7 Å [110]. The dimensionless thickness is,

$$\lambda = \frac{L}{L_0}, \tag{4.22}$$

and the position variable is

$$\xi = \frac{x}{L_0}. \tag{4.23}$$

The dimensionless oxygen ion vacancy concentration is,

$$\tilde{C} = \frac{C}{C_0}. \tag{4.24}$$

The dimensionless electric field is,

$$\tilde{E}(\xi,\tau) = \frac{zFE(x,t)}{RT} \tag{4.25}$$

and

$$Z = \frac{zFC_0L_0^2}{\epsilon_0\epsilon_r} \tag{4.26}$$

The dimensionless oxygen ion vacancy concentration is,

$$\tilde{C}(\xi,\tau) = \frac{C(x,t)}{C_0}. \tag{4.27}$$

The rate constants in nondimensional form are,

$$\tilde{k}_{1f} = \frac{k_{1f}^0 L_0}{D\tilde{C}_0} \exp\left(\frac{\alpha F\phi_{m/o}}{RT}\right), \tag{4.28}$$

$$\tilde{k}_{1r} = \frac{k_{1r}^0 L_0}{D\tilde{C}_0} \exp\left(\frac{\alpha F\phi_{o/m}}{RT}\right), \tag{4.29}$$

$$\tilde{k}_{2f} = \frac{k_{2f}^0 L_0}{D\tilde{C}_0}, \tag{4.30}$$

and

$$\tilde{k}_{2r} = \frac{k_{2r}^0 L_0}{D\tilde{C}_0}. \tag{4.31}$$

The dimensionless growth rate constant is,

$$\tilde{\kappa} = \frac{k_{1f}L_0}{D\epsilon}, \tag{4.32}$$

and the dimensionless reduction rate constant is,

$$\tilde{\kappa_r} = \frac{k_{1r}L_0}{D\epsilon}. \tag{4.33}$$

The model parameter Γ is non-dimensionalized but can be broken into dimensional components,

$$\Gamma = \frac{\gamma}{C_0}. \tag{4.34}$$

Using the above variables, Equation 4.1 and 4.2 become,

$$\frac{\partial\tilde{C}(\xi,\tau)}{\partial\tau} = -\frac{\tilde{J}(\xi,\tau)}{\partial\xi} \tag{4.35}$$

and

$$\tilde{J}(\xi,\tau) = -\frac{\partial\tilde{C}(\xi,\tau)}{\partial\xi} - \tilde{C}(\xi,\tau)\tilde{E}(\xi,\tau), \tag{4.36}$$

respectively. Inserting the above variables into Equation 4.7 gives,

$$\frac{\partial \tilde{C}(\xi,\tau)}{\partial \tau} = \frac{\partial^2 \tilde{C}(\xi,\tau)}{\partial \xi^2} - \frac{\partial \tilde{C}(\xi,\tau)}{\partial \xi}\tilde{E}(\xi,\tau) - \tilde{C}(\xi,\tau)\frac{\partial \tilde{E}(\xi,\tau)}{\partial \xi}. \tag{4.37}$$

Equation 4.3 becomes,

$$\frac{\partial \tilde{E}(\xi,\tau)}{\partial \xi} = Z\tilde{C}(\xi,\tau), \tag{4.38}$$

and Equation 4.8 is,

$$\frac{d\lambda(\tau)}{d\tau} = \tilde{\kappa}\tilde{f}_{1f}\tilde{C}(0) - \tilde{\kappa}_r\tilde{f}_{1r}\tilde{C}(0)). \tag{4.39}$$

After non-dimensionalization, the interfacial functions become,

$$\tilde{f}_{1f} = \frac{1}{2}(1 + \tanh(\Gamma(1 - \tilde{C}(0))), \tag{4.40}$$

$$\tilde{f}_{1r} = \frac{1}{2}(1 + \tanh(\Gamma(\tilde{C}(0) - 1)), \tag{4.41}$$

$$\tilde{f}_{2f} = \tilde{C}(\lambda), \tag{4.42}$$

and

$$\tilde{f}_{2r} = 1 - \tilde{C}(\lambda). \tag{4.43}$$

The boundary conditions must be non-dimensionalized as well. At $\xi = 0$,

$$\tilde{J}\Big|_{\xi=0} = \tilde{k}_{1f}\tilde{f}_{1f}(\tilde{C}(0)) - \tilde{k}_{1r}\tilde{f}_{1r}(\tilde{C}(0)) \tag{4.44}$$

At ξ=λ,

$$\tilde{J}\Big|_{\xi=\lambda} = \tilde{k}_{2f}\tilde{f}_{2f}(\tilde{C}(\lambda)) - \tilde{k}_{2r}\tilde{f}_{2r}(\tilde{C}(\lambda)) \tag{4.45}$$

We non-dimensionalize charge density as

$$\tilde{\sigma} = \frac{\sigma RT}{\epsilon_r \epsilon_0 F} \tag{4.46}$$

Thus equations 4.19 and 4.20 become

$$\tilde{E}(\xi,\tau)|_{\xi=0} = \tilde{\sigma}(0) \tag{4.47}$$

and

$$\tilde{E}(\xi,\tau)|_{\xi=\lambda} = \tilde{\sigma}(\lambda(\tau)) \tag{4.48}$$

4.6 Summary

This chapter presented a model for platinum oxide growth and reduction. The model is based on the diffusion and migration of oxygen vacancies to promote oxide thickness change. The main differences between this model and others in the literature are it explicitly applies a mathematical formalism to account for the interfacial reactions that occur, and the oxide growth and reduction of the layer are encompassed in a single model. In the next chapter, the model is solved in the quasi-steady state limit for only the oxide formation and growth phenomena. Chapter 6 incorporates the reduction process and presents an approach for the transient solution to the entire oxide growth and reduction modelling framework.

Chapter 5

Quasi-Steady State Solution and Results for Oxide Formation and Growth

H. A. Baroody, G. Jerkiewicz, M. H. Eikerling, Journal of Chemical Physics, 146: 144102, 2017. https://doi.org/10.1063/1.4979121

Material from this publication is used in this chapter with permission from AIP Publishing.

Author contribution: HB and ME developed the research question. HB performed the literature review and proposed the approach. ME refined the equations. HB solved the model and performed the parametric analysis and experimental comparison. GJ provided experimental results and insight. ME and HB analyzed and interpreted the results. HB and ME wrote the manuscript. ME and GJ reviewed the work.

5.1 Introduction

It is important in model development to start as simply as possible and then add complexities if necessary. Simple models offer vital mechanistic insights. As we have seen, oxide formation, growth, and reduction are not trivial processes and transcend many disciplines from solid state chemistry, electrochemistry, physics, mathematics, to name a few. Breaking the process into its key components and building from there affords the opportunity to understand exactly the impact each parameter has on the results of the model and what assumptions are reasonable.

In this chapter we limit the model developed in Chapter 4 to only describe the formation and growth of platinum oxide. This was a logical first step because there are many literature studies with quality experimental data that have isolated the growth phenomena to compare our model with. If we can develop a solid model that describes oxide formation and growth, we can then add the reduction component with more confidence where there is not as much available experimental data. The model assumptions are discussed with the corresponding changes to the equations and then the results are presented and discussed.

5.2 Model Equation Modifications

We consider growth at a fixed potential across the oxide layer and impose an assumption that the potential drops at the boundaries of the oxide layer are constant because their composition remains constant as the oxide layer grows [76, 79]. This assumption results in potential drops at the boundaries that are independent of the oxide layer thickness. With the assumption of constant composition, it follows that the potential gradient is constant across the layer and decreases as the oxide layer grows [120]. This assumption allows for the Poisson equation to be neglected and we define,

$$\frac{\partial \phi}{\partial x} = \frac{\phi_L - \phi_0}{L(t)}, \tag{5.1}$$

where ϕ_0 and ϕ_L are the potentials at the M-O and O-E interfaces, respectively. Assuming a constant diffusion coefficient, the above equation modifies Equation 4.2 to,

$$\frac{\partial C(x,t)}{\partial t} = D\frac{\partial^2 C(x,t)}{\partial x^2} + \frac{zFD}{RT}\left(\frac{\phi_L - \phi_0}{L(t)}\right)\frac{\partial C(x,t)}{\partial x}. \tag{5.2}$$

All reactions are assumed to occur at the boundaries of the oxide layer. Since we are only considering oxide formation and growth, reverse rate constants are set to zero. This reduces the boundary conditions to

$$J\Big|_{x=0} = k_{1f} f_{1f}(C(0)), \tag{5.3}$$

and

$$J\Big|_{x=L} = k_{2f} f_{2f}(C(L)). \tag{5.4}$$

The thickness equation omits the reduction component and becomes simply the oxide growth over time,

$$\frac{dL(t)}{dt} = \kappa f_{1f}(C(x))|_{x=0}, \tag{5.5}$$

where κ is the growth rate constant that is equal to the reaction rate constant k_1 (mol m^{-2} s^{-1}) divided by a Pt expansion factor, ϵ (mol cm^{-3}). The expansion factor is the number of oxygen ion vacancies needed to create one monolayer of oxide, divided by the thickness of a monolayer.

5.2.1 Non-dimensionalization

To consolidate the variables and simplify the math without compromising the solution we define a new dimensionless variable for the potential difference across the oxide layer,

$$\Phi = \frac{zF}{RT}(\phi_L - \phi_0). \tag{5.6}$$

The rate constants are simplified and converted to a non-dimensional form as,

$$\tilde{k}_{1f} = \frac{k_1 L_0}{DC_0} \quad \text{and} \quad \tilde{k}_{2f} = \frac{k_2 L_0}{DC_0}. \tag{5.7}$$

Inserting the above variables and the other necessary defined variables from Section 4.5 into Equation 4.7 gives,

$$\frac{\partial \tilde{C}(\xi,\tau)}{\partial \tau} = \frac{\partial^2 \tilde{C}(\xi,\tau)}{\partial \xi^2} + \frac{\Phi}{\lambda(\tau)}\frac{\partial \tilde{C}(\xi,\tau)}{\partial \xi}. \tag{5.8}$$

The thickness growth equation, Equation 5.5, becomes

$$\frac{d\lambda(\tau)}{d\tau} = \tilde{\kappa}\tilde{f}_{1f}(\tilde{C}(0)). \tag{5.9}$$

The boundary conditions must be non-dimensionalized as well. At $\xi = 0$,

$$\left.\frac{d\tilde{C}(\xi)}{d\xi}\right|_{\xi=0} + \frac{\Phi C(0)}{\lambda} = -\tilde{k}_{1f}\tilde{f}_{1f}(\tilde{C}(0)). \tag{5.10}$$

At ξ=λ,

$$\left.\frac{d\tilde{C}(\xi)}{d\xi}\right|_{\xi=\lambda} + \frac{\Phi C(0)}{\lambda} = -\tilde{k}_{2f}\tilde{f}_{2f}(\tilde{C}(\lambda)). \tag{5.11}$$

5.3 Model Solution

The transport model equation was solved in steady state approximation, i.e. assuming,

$$\frac{\partial \tilde{C}(\xi,\tau)}{\partial \tau} = \frac{\partial^2 \tilde{C}(\xi,\tau)}{\partial \xi^2} + \frac{\Phi}{\lambda}\frac{\partial \tilde{C}(\xi,\tau)}{\partial \xi} = 0. \tag{5.12}$$

Under steady state conditions, λ is treated as a parameter, giving the following general solution,

$$\tilde{C}(\xi) = \tilde{a}\exp\left(-\frac{\Phi\xi}{\lambda}\right) + \tilde{b}, \tag{5.13}$$

where $\tilde{a}$ and $\tilde{b}$ are constants that depend on λ. The integration constants in Equation 5.13 are obtained from using the boundary equations in Equation 4.13, which results in

$$\frac{2\Phi\tilde{b}}{\tilde{k}_{1f}\lambda} = 1 + \tanh\left(\Gamma\left(1 - \left(\tilde{a} + \tilde{b}\right)\right)\right), \tag{5.14}$$

and

$$\tilde{b} = -\frac{\tilde{k}_{2f}\tilde{a}\exp(-\Phi)}{\frac{\Phi}{\lambda} + \tilde{k}_{2f}}. \tag{5.15}$$

We can further simplify by regrouping parameters. Reducing the model to the minimum set of free parameters allows us to navigate the full range of solutions more easily. We define,

$$\alpha = -\frac{2\Phi}{\lambda\tilde{k}_{1f}}, \tag{5.16}$$

and

$$\beta = -\frac{\tilde{k}_{2f}\exp(-\Phi)}{\frac{\Phi}{\lambda} + \tilde{k}_{2f}}. \tag{5.17}$$

Now Equations 5.14 and 5.15 can be combined and simplified,

$$\alpha\beta\tilde{a} = 1 + \tanh(\Gamma(1 - \tilde{a}(1+\beta))). \tag{5.18}$$

A numerical solution for $\tilde{a}$ was found using Equation 5.18 and the results were determined and analyzed.

To determine the change in oxygen ion vacancy density at the M-O interface as the oxide layer grows, we consider Equation 5.13 at $\xi = 0$,

$$\tilde{C}(0) = \tilde{a} + \tilde{b}, \tag{5.19}$$

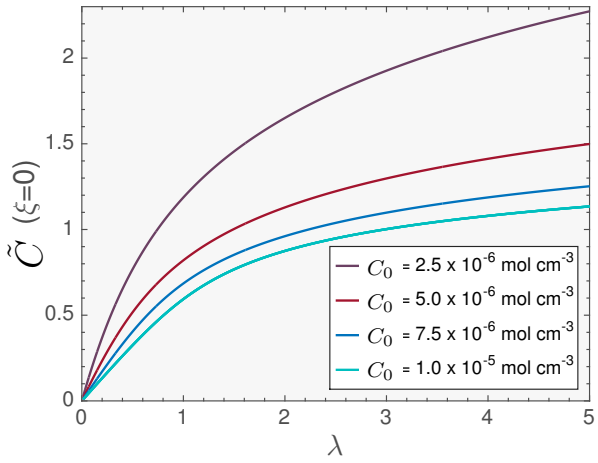

Figure 5.1: Oxygen ion vacancy density at the M-O interface as oxide layer thickness, λ, is increased at varying C_0 values.

We can eliminate $\tilde{b}$ by using Equation 5.15 and 5.17 in 5.19, giving,

$$\tilde{C}(0) = \tilde{a}(1 + \beta) \tag{5.20}$$

Equation 5.20 is plotted in Figure 5.1 and shows the change in oxygen ion vacancy density at the M/O interface as the oxide layer grows. It is seen that the oxygen ion vacancy density increases more rapidly in the thin film limit, below about one monolayer, but levels off as the film thickens.

Equation 5.20 is used to explore the relationship between $\tilde{C}(0)$ and λ, Γ, or Φ as illustrated in Figure 5.2. Figure 5.2a shows that as Φ decreases, $\tilde{C}(0)$ increases. A larger field across across the oxide layer will result in larger $\tilde{C}(0)$ values. As λ is decreased, there is less of a dependence seen in Figure 5.2b between $\tilde{C}$ and Φ.

5.4 Adding Dimensions

The reference thickness is $L_0 = 2.7 \times 10^{-8}$ cm. This was calculated by dividing the unit cell height of the PtO structure, 5.34 Å (Pt_2O_2), in two because there are two oxygen layers in one unit cell of the PtO structure [110]. We define a monolayer of the oxide to be the equivalent of the thickness of one unit cell. In order for the quasi-static approximation to be valid, the diffusion length must be large compared to oxide layer thickness. Thus we set the diffusion coefficient of oxygen ion vacancies to be, $D = 1.0$

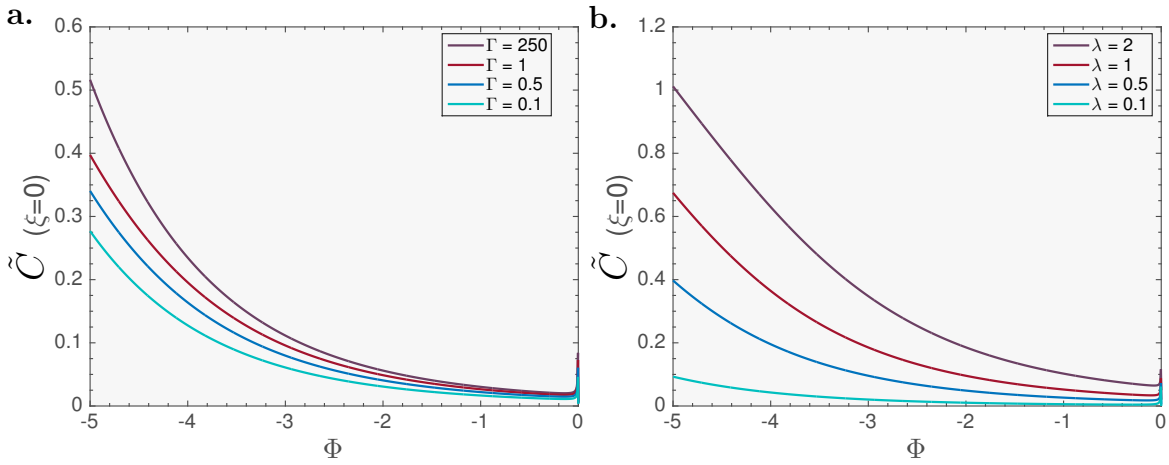

Figure 5.2: Oxygen ion vacancy density at the M-O interface as a function of Φ a.) $\lambda = 0.5$; b.) $\Gamma = 1$.

$\times\ 10^{-14}$ cm^2 s^{-1}. Using aforementioned L_0 and D, the time scale becomes,

$$t = 7.1 \times 10^{-2}\text{s} \times \tau \tag{5.21}$$

The potential difference, Φ, is determined using $z = 2$ and $\Delta\phi = \phi_L - \phi_0$ = -0.05 V [121],

$$\Phi = \frac{zF}{RT}(\phi_0 - \phi_L) = -3.9. \tag{5.22}$$

$\Delta\phi$ is assumed to be negative due to the potential drop across the layer from the M-O interface to the O-E interface. We use a value of $\Delta\phi = 0.05$ based on the work of Ref. [78] that uses a value of 0.1 and of Ref. [122] that discusses the relationship between potential across the oxide and oxide thickness applying Mott-Cabrera theory.

The relationship $\kappa = k_1\epsilon^{-1}$ explicitly accounts for the surface geometry in the model. The expansion factor, ϵ, directly relates to the structure of the oxide. For example, α-PtO_2 has a layered structure similar to CdI_2 [110]. The lattice parameters of the oxide are a = 4.34 Å, b = c = 3.11 Å with a volume of 42.1 Å^3 per two oxygen ions; for PtO the volume is 50.6 Å^3 per two oxygen ions [110]. The density of oxygen ions for α-PtO_2 is

$$\frac{2\text{ O atoms}}{4.21 \times 10^{-23}\text{ cm}^3} = 4.8 \times 10^{22}\text{ cm}^{-3} \tag{5.23}$$

and for the PtO,

$$\frac{2\text{ O atoms}}{5.058 \times 10^{-23}\text{ cm}^3} = 4.0 \times 10^{22}\text{ cm}^{-3}. \tag{5.24}$$

Converting to molar concentration gives,

$$\epsilon = \frac{4.8 \times 10^{22} \text{ O atoms cm}^{-3}}{N_A} = 7.9 \times 10^{-2} \text{ mol cm}^{-3} \tag{5.25}$$

for α-PtO_2 and,

$$\epsilon = \frac{4.0 \times 10^{22} \text{ O atoms cm}^{-3}}{N_A} = 6.6 \times 10^{-2} \text{ mol cm}^{-3} \tag{5.26}$$

for PtO. Hypothetically, if all model parameter values were known from experiment, the value of ϵ could be extracted from experiment by model fitting. The value C_0 is defined as the characteristic amount of surface coverage of oxygen ion vacancies needed to promote place exchange and is reported in units of mol cm^{-3}. By knowing the amount C that corresponds to a coverage of 1 ML of oxygen ion vacancies on the surface, C_0 can be determined by calculating the percent required to promote oxide growth presented in literature studies. The latter is calculated by determining the surface area of the metal and determining the number of oxygen ion vacancies per atom.

Several literature studies indicate a surface oxygen coverage far greater than 50% is needed to promote place exchange [105, 106, 3, 118]. Sun *et al.* determined the fraction of vacant sites across the entire oxide layer in the PtO lattice including interstitial sites to increase from 0.087 to 0.164 as the potential was increased from 1.14 to 1.39 V_{SHE} based on Mott-Schottky plot [69]. Unfortunately there is no data specifying the vacancy density at the interface or the amount necessary to promote place exchange.

It is to be noted that experimentally the thickness of the platinum oxide layer has not been measured directly. Most experimentalists apply a potential to a platinum electrode at a sufficiently high voltage to grow an oxide layer; then the potential is reversed and the current flowing during oxide reduction is recorded. The degree of oxidation is computed by integrating the oxidation current curve. From the results of the calculated charge, the thickness of the layer can be deduced provided the oxide layer formation is associated with charge flux and the thickness change per amount of charge is known, which is calculated from the amount of oxygen in the specific oxide structure. Here the problem arises that the exact structure of the oxide must be known in order to determine the thickness of the entire layer. Further issues arise if the structure of the oxide layer is not uniform across the thickness or if it involves different

layers or crystalline structures. This creates issues when attempting to convert charge to thickness without making assumptions about the architecture of the layer.

5.5 Parametric Analysis

A parametric analysis is performed. The black model lines in Figures 5.3-5.6 use the reference set of parameters in Table 5.1. In Figure 5.3a, the effect of the extraction rate constant k_{1f} is explored. It is seen that there is a delay in the oxide growth as k_{1f} decreases. Increasing k_{1f} increases λ. A similar trend is seen in Figure 5.3b, which shows the effect of k_{2f} when k_1 is 1×10^{-10} mol cm^{-2} s^{-1}. Increasing k_{2f} also increases λ until the growth law approaches an asymptotic limit for $k_{2f} > 1\times\ 10^{-11}$ mol cm^{-2} s^{-1}. This shows that above the specified value of k_{2f}, the rate of recombination is sufficiently rapid to not exert any impact on the overall rate of oxide growth. The assumption that the rate determining step is the extraction of Pt atoms across the M-O interface, requires $k_2 \gg k_1$ thus we set k_{2f} to 1 $\times 10^{-7}$ mol cm^{-2} s^{-1}, for the remainder of this chapter.

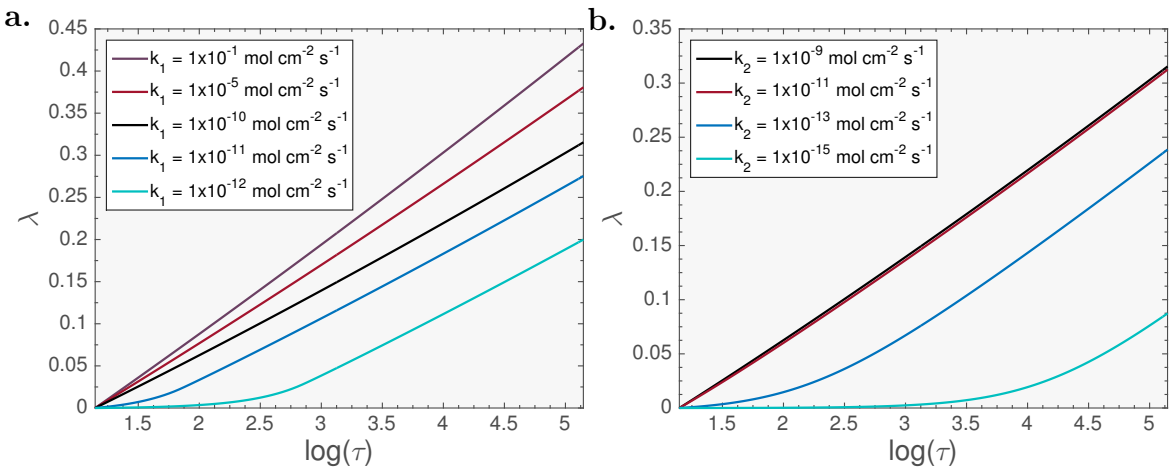

Figure 5.3: Parametric dependence of oxide growth upon varying the rate constant, a.) k_1 across the M-O interface, and b.) k_2 across the O-E interface.

Figure 5.4a shows the effect of varying Φ. The potential difference across the oxide layer and temperature are parameters coupled in Φ. Temperature can also affect many of the other parameters such as rate constants; thus when varying Φ, we only consider the effects of the potential across the oxide layer, ϕ_L-ϕ_0. It is seen in Figure 5.4a, as Φ becomes more negative, oxide growth increases; meaning a larger field across the

Symbol	Units	
T	K	298
$\Delta\phi$	V	-0.05
D	$cm^2\ s^{-1}$	1.0×10^{-14}
L_0	cm	2.7×10^{-8}
k_{1f}	$mol\ cm^{-2}\ s^{-1}$	1.0×10^{-10}
k_{2f}	$mol\ cm^{-2}\ s^{-1}$	1.0×10^{-9}
C_0	$mol\ cm^{-3}$	5.0×10^{-4}
γ	$cm^3\ mol^{-1}$	5.0×10^{4}
ϵ	$mol\ cm^{-3}$	0.066

Table 5.1: Table of general parameter values for Section 5.5.

oxide layer will accelerate the growth of the layer. Figure 5.4b shows the change in oxide growth if ϵ is varied. The oxide layer grows faster at smaller ϵ values.

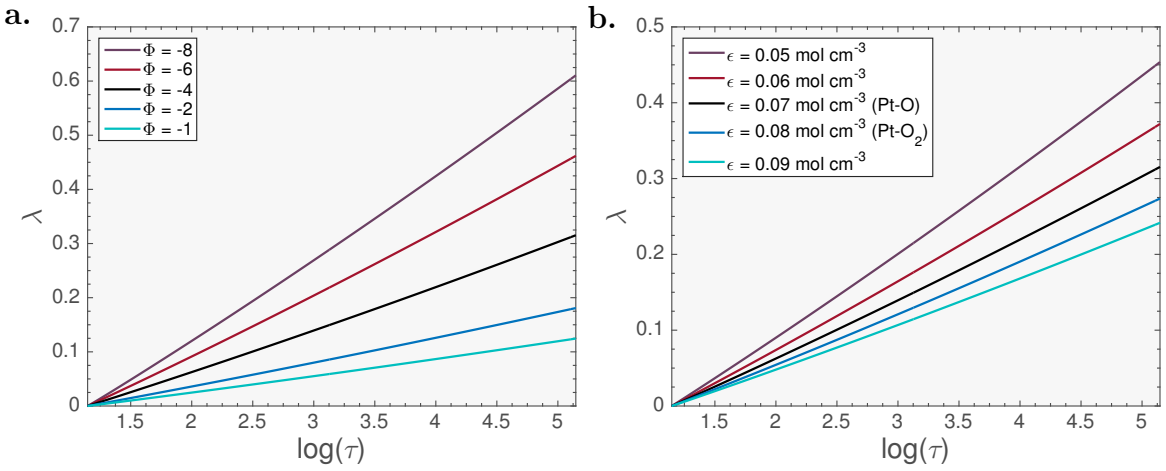

Figure 5.4: Parametric analysis of oxide growth upon varying a.) the non-dimensional parameter, Φ that includes the potential difference across the layer, and b.) the geometric parameter, ϵ, that relates to the density of the oxide layer.

The effect of varying C_0 is shown in Figure 5.5. More oxide growth is observed at higher C_0 values. That is the higher the number of oxygen ion vacancies required for Pt extraction, the faster the oxide film will grow. Figure 5.6 shows the influence of Γ on the oxide growth. At very high Γ values, when the transfer function at the M-O interface is step-like, the oxide growth rate is logarithmic. But as Γ is decreased and the steepness of f_{1f} is relaxed, the growth of the oxide layer diverges.

Understanding the direct parametric effect of potential and temperature is not trivial because there are many parameters that are affected when they are varied. As has been discussed, increasing applied potential changes the structure of the metal

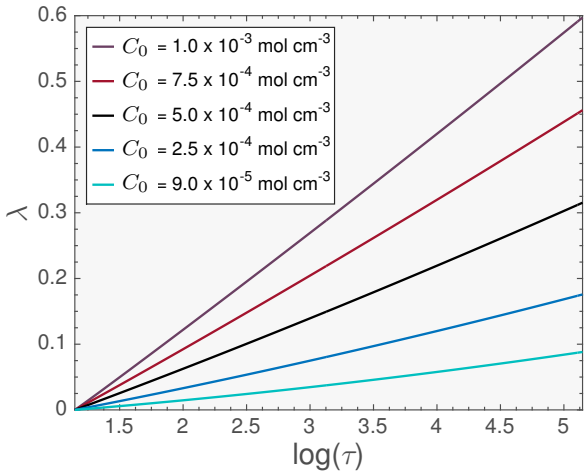

Figure 5.5: Effect of varying, C_0, the oxygen ion vacancy density at the metal boundary required to promote oxide growth.

surface and of the oxide, thus affecting kinetic and geometric parameters. Similar effects are seen with changing temperature. To dissect the parameters that are most affected by potential and temperature, experimental trends are analyzed.

5.6 Comparison with Experimental Data

The model is applied to various experimental data. Much of the oxide growth data published does not specify many of the parameters needed for the model, in part because it is difficult or not yet possible to measure certain parameters such as the extraction rate across the interface. We can make approximations based on logical assumptions, compare results, and analyze parametric effects.

In Figure 5.7a, the model is applied to data from Imai *et al.* [3]. The degree of oxidation of highly dispersed carbon-supported platinum nanoparticles was determined during a potential step experiment to 1.4 V_{RHE}. Imai *et al.* calculated the current contribution from double layer charging during CV scans and subtracted it from the total current to isolate in the oxidation current [3]. They integrated the oxidation current to give the charge and calculated the ratio of the oxide charge over the hydrogen charge. For comparison, both the axes have been converted to non-dimensional units defined in this article assuming the oxide layer is only PtO with charge contribution of 440 μC cm^{-2} per layer. This is the same assumption used in the published experimental work thus it is presented this way for consistency [5].

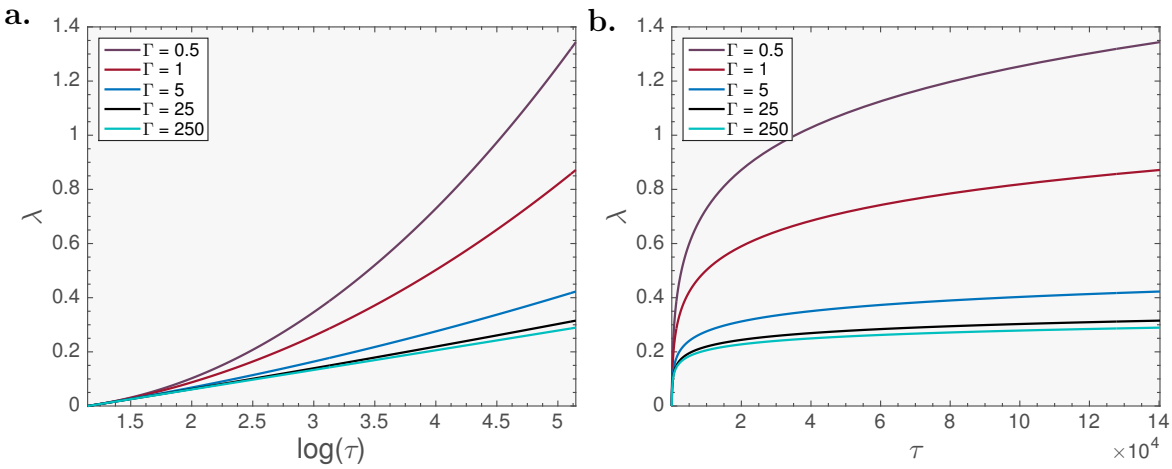

Figure 5.6: Dependence of oxide growth on Γ.

Symbol	Units	a.	b.
T	K	298	298
$\Delta\phi$	V	-0.05	-0.05
D	$cm^2\ s^{-1}$	1.0×10^{-14}	1.0×10^{-14}
L_0	cm	2.7×10^{-8}	2.7×10^{-8}
k_{1f}	$mol\ cm^{-2}\ s^{-1}$	1.8×10^{-10}	1.0×10^{-10}
k_{2f}	$mol\ cm^{-2}\ s^{-1}$	1.0×10^{-7}	1.0×10^{-7}
C_0	$mol\ cm^{-3}$	6.5×10^{-3}	2.1×10^{-2}
γ	$cm^3\ mol^{-1}$	9.0×10^3	9.0×10^3
ϵ	$mol\ cm^{-3}$	0.070	0.070

Table 5.2: Table of parameter values for Figure 5.7

Figure 5.7b shows the model applied to experimental data reported from Fromhold in Ref. [4] using similar assumptions. The oxide film was plasma-produced and is significantly thicker than recent experimental data for oxide formation. The model shows good agreement. Model parameters used in Figure 5.7 are listed in Table 5.2.

The model is applied to experimental data collected from Furuya *et al.* in Figure 5.8a and 5.8b [5]. The surface oxide was grown on a polycrystalline Pt electrode in CF_3SO_3H solution under potentiostatic conditions at a range of potentials and temperatures. The experimental oxide growth data is shifted to begin at zero at the onset of oxide growth. This corrects for the impact of other contributions, e.g., anion desorption, to the recorded current.

The parameters used for the model were taken from experimental data; they are presented in Table 5.3. The unit cell thickness, L_0, and the diffusion coefficient, D, are based on the discussion in Section 5.4. The reaction rate k_{1f} is determined based

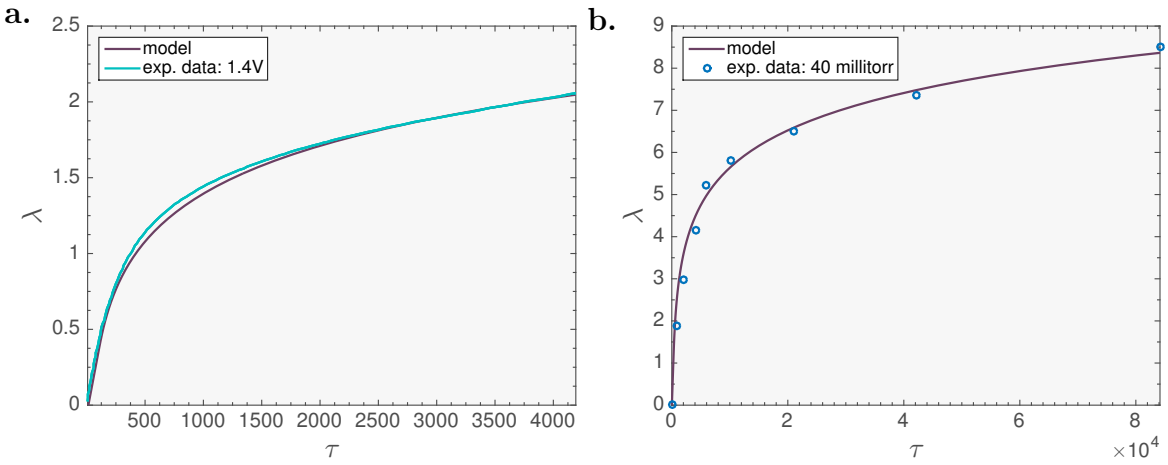

Figure 5.7: Model results applied to experimental data a.) reported at 1.4V from Imai *et al.* [3] and b.) from Fromhold *et al.* [4]. Parameters used are found in Table 5.2.

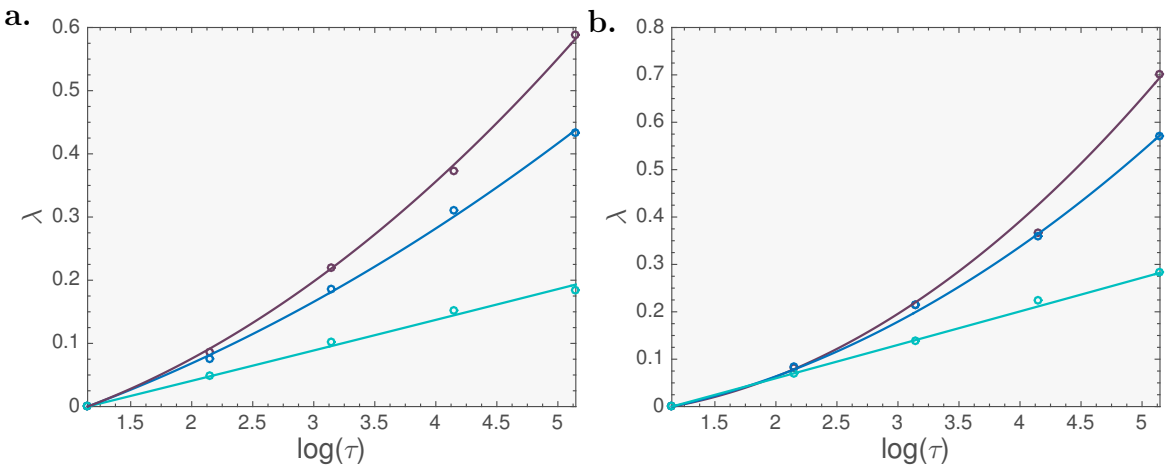

Figure 5.8: Model results applied to experimental data reported from Furuya *et al.* [5] for a.) 298 K and b.) 333 K at varying potentials: purple - 1.5V$_{SHE}$; blue - 1.3 V$_{\mathrm{SHE}}$; cyan - 1.1 V$_{\mathrm{SHE}}$. The model parameters are in Table 5.3.

Symbol	Unit	a. 1.1V$_{\mathrm{RHE}}$	a .1.3V$_{\mathrm{RHE}}$	a. 1.5V$_{\mathrm{RHE}}$	b. 1.1V$_{\mathrm{RHE}}$	b. 1.3V$_{\mathrm{RHE}}$	b. 1.5V$_{\mathrm{RHE}}$
T	K	298	298	298	333	333	333
$\Delta\phi$	V	-0.05	-0.05	-0.05	-0.05	-0.05	-0.05
D	cm^2 s^{-1}	1.0×10^{-14}	1.0×10^{-14}	1.0×10^{-14}	1.0×10^{-14}	1.0×10^{-14}	1.0×10^{-14}
L_0	cm	2.7×10^{-8}	2.7×10^{-8}	2.7×10^{-8}	2.7×10^{-8}	2.7×10^{-8}	2.7×10^{-8}
k_{1f}	mol cm^{-2} s^{-1}	1.0×10^{-10}	1.3×10^{-12}	5.6×10^{-13}	1.0×10^{-10}	6.5×10^{-13}	3.1×10^{-13}
k_{2f}	mol cm^{-2} s^{-1}	1.0×10^{-7}	1.0×10^{-7}	1.0×10^{-7}	1.0×10^{-7}	1.0×10^{-7}	1.0×10^{-7}
C_0	mol cm^{-3}	3.4×10^{-4}	1.0×10^{-5}	4.4×10^{-6}	5.0×10^{-4}	2.2×10^{-6}	1.5×10^{-6}
γ	cm^3 mol^{-1}	5.0×10^{5}	5.0×10^{5}	5.0×10^{5}	5.0×10^{5}	5.0×10^{5}	5.0×10^{5}
ϵ	mol cm^{-3}	0.070	0.070	0.070	0.070	0.070	0.070

Table 5.3: Table of parameter values for Figure 5.8

on the data set. As mentioned, k_{2f} is set to 1 $\times 10^{-7}$ mol cm^{-2} s^{-1} rendering the solution insensitive to this parameter.

The model reproduces the experimental data very closely in Figure 5.8. In analyzing the parameters listed in Table 5.3, there is a significant decrease in k_{1f} seen as the potential increases from 1.1 V_{RHE} to 1.3 V_{RHE}. A less pronounced decrease in k_{1f} is seen upon further increase of the growth potential to 1.5 V_{RHE}. This observation suggests that above 1.3 V_{RHE} there is a change in the extraction and growth mechanism that slows the Pt extraction rate across the M-O interface. The value of C_0 also decreases more significantly when the potential increases from 1.1 V_{RHE} to 1.3 V_{RHE} compared to 1.3 V_{RHE} to 1.5 V_{RHE}. According to previous literature on the topic, the potential range between 1.1 V_{RHE} and 1.3 V_{RHE} is a critical range, in which the oxide layer undergoes significant change that has been associated with the high-growth regime [51], irreversibility [98], and the onset of increased dissolution due to the oxide layer dynamics [46, 66]. From the model we can conclude that as the oxide layer grows, the rate of Pt extraction across the M-O interface decreases and the growth becomes less dependent on $\tilde{C}(0)$. According to this analysis, the geometric factor ϵ does not increase, which is in accord with results of Xing *et al.* who stated that the growth of a PtO_2 layer does not commence until above 1.6 V_{RHE} [51].

To demonstrate its versatility, the model is applied to the oxidation of Iron (Fe) and Nickel (Ni). Figure 5.9 shows the oxidation of Fe for different surface structures explored in Ref [6]. Single crystals of known orientation were produced in that work using a Ferrovac E iron by strain annealing. The iron was oxidized by first reducing the layer with hydrogen several times to clear the surface, then the specimen was reheated under continuous oxygen pressure of about 1.3 x $10^{-}2$ Torr. Reflection electron diffraction was used to identify the oxide phases present [6]. Experimental results were normalized and the y-axis was converted to monolayers of oxide for Fe_3O_4. The geometric parameters were calculated for Fe. The results show that different metal structures result in different rates of metal ion extraction across the interface.

Figure 5.10 shows the model applied to experimental data for β-$Ni(OH)_2$, with the corresponding parameters shown in Table 5.5 [7]. Nickel was oxidized in 0.5 aqueous M KOH using cyclic voltammetry. X-ray photoelectron spectroscopy (XPS) was used to determine the passive layer thickness [7]. More analysis is needed for other metals but these preliminary results are promising.

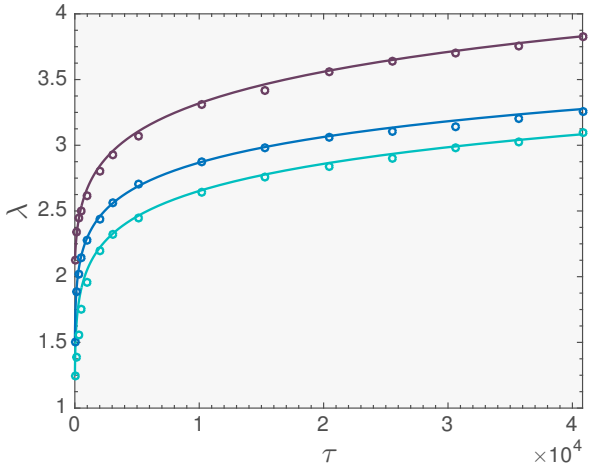

Figure 5.9: Model results applied to experimental data of the oxidation of polycrystalline (pc) [purple], (110) [blue], and (112) [cyan] iron surfaces at 100° C from Graham *et al.* [6]. The parameters for the model are listed in Table 5.4. The model was scaled to the start of the experimental data similar to above.

Symbol	Units	Fe(pc)	Fe(110)	Fe(112)
T	K	373	373	373
$\Delta\phi$	V	-0.05	-0.05	-0.05
D	$cm^2\ s^{-1}$	1.0×10^{-14}	1.0×10^{-14}	1.0×10^{-14}
L_0	cm	4.2×10^{-8}	4.2×10^{-8}	4.2×10^{-8}
k_{1f}	$mol\ cm^{-2}\ s^{-1}$	5.0×10^{-11}	3.3×10^{-10}	3.0×10^{-10}
k_{2f}	$mol\ cm^{-2}\ s^{-1}$	1.0×10^{-7}	1.0×10^{-7}	1.0×10^{-7}
C_0	$mol\ cm^{-3}$	2.5×10^{-3}	4.0×10^{-3}	3.8×10^{-3}
γ	$cm^3\ mol^{-1}$	400	400	400
ϵ	$mol\ cm^{-3}$	0.080	0.080	0.080

Table 5.4: Table of parameter values for Figure 5.9

Symbol	Units	0.7 V	1.1 V
T	K	295	295
$\Delta\phi$	V	-0.05	-0.05
D	$cm^2\ s^{-1}$	1.0×10^{-14}	1.0×10^{-14}
L_0	cm	2.3×10^{-8}	2.3×10^{-8}
k_{1f}	$mol\ cm^{-2}\ s^{-1}$	5.0×10^{-11}	1.0×10^{-10}
k_{2f}	$mol\ cm^{-2}\ s^{-1}$	1.0×10^{-7}	1.0×10^{-7}
C_0	$mol\ cm^{-3}$	5.0×10^{-3}	5.0×10^{-3}
γ	$cm^3\ mol^{-1}$	22	22
ϵ	$mol\ cm^{-3}$	0.074	0.074

Table 5.5: Table of parameter values for Figure 5.10

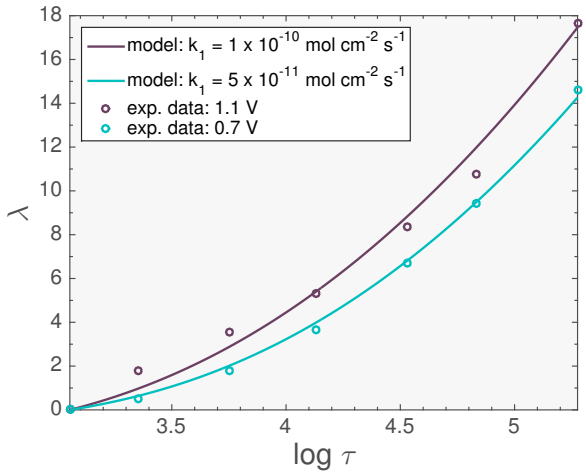

Figure 5.10: Model results applied to experimental data of the oxidation of β-Ni(OH)$_2$ using experimental results from Ref. [7]. The parameters for the model are listed in Table 5.5.

5.7 Summary and Outlook

A mathematical model was solved to derive laws of oxide growth phenomena on metal surfaces. The model is solved numerically in steady state approximation. The main conclusions are:

1. Oxide growth is sensitive to the oxygen ion vacancy concentration at the M-O interface and the rate of Pt ion extraction across this interface.

2. Good agreement is seen with a range of experimental data for different metals.

3. The model encompasses a wide range of growth laws displayed in experimental data from various studies.

4. Reasonable parameters can be extracted from the model that allow for insightful mechanistic interpretations.

The most noteworthy difference in the model presented compared to studies in the literature is that the boundary condition at the M-O (Pt-PtO) interface that incorporates the interfacial kinetics and controls the growth of the oxide. In comparison, the Point Defect Model and the Generalized Growth Model both account for reactions happening at the interface but they assume that growth is controlled by species transport across the layer and do not account for the threshold in O_{ad} density at the

M-O interface that seems necessary in order to promote oxide growth [78, 123]. We implemented a peculiar form of the M-O boundary conditions in Equations 4.9 and 4.10 to account for this limit. As far as the author is aware, this is the first time a single model of oxide growth has been compared to such a robust set of experimental data sets and metals.

The next step is to add the oxide reduction phenomena into the model. Initially a similar approach will be applied. The steady-state approximation used in this chapter proved to be a reasonable assumption as the model recreated experimental data reasonably well. In the next chapter the validity of the assumption will have to be revisited. Ultimately a solution in the non-steady state limitation would be ideal.

Chapter 6

Quasi-Steady State Solution and Results for Oxide Reduction

6.1 Introduction

It was seen in the last chapter that our model can be simplified to reproduce a variety of experimental data of oxide formation and growth showing the assumptions applied were reasonable. The goal of this chapter is to solve the model for the reduction of platinum oxide. First, we assess the quasi-steady state limit similar to Chapter 5. This limit is valid under the assumption that equilibrium of the reactions at each interface is established rapidly such that the relaxation time of the layer will be much less than the layer formation time [124]. For this limiting case, the model is either solved in the growth phase, or reduction phase and cannot incorporate both, that is the transition from one phase to the other. The transient solution is necessary to capture the transition phase. The main model assumptions are carried over from the oxide growth model. It is important to stress that the assumption that the defect density is small is crucial. For example, in the case that oxygen atoms leave the oxide layer much more rapidly than the platinum ions return to the bulk metal, a large defect density would result in moving reaction front that would potentially leave a fragile platinum skeleton layer in the extreme case. This skeleton layer would essentially collapse into a highly disorder surface. In the case of a large defect density, a different model would be necessary, such as a phase field model, because the layer thickness would no longer be determined by the simple transport and migration mechanics of the defect density.

After the model is solved, a parametric analysis is performed and the validity of the model assumptions are discussed. Then a transient solution approach is outlined.

Including oxide reduction to the growth model adds several levels of complexity to consider. For instance, as discussed in Section 2.4, during reduction the oxide layer undergoes structural changes. The structure relates directly to the electronics thus if the exact structure is unknown, how the electronics contributes to the process is then not known as well. We first explore the steady state limit in order to simplify the model and have a base to build on and relax assumptions if necessary.

6.2 Model Equation Modifications for the Steady State Limit

To add the platinum oxide reduction component, we apply the same approach as outlined in Chapter 5 but use the full boundary conditions and interfacial functions listed in Chapter 4. As a reminder, the non-dimensionalized transport equation for the quasi-steady state approach is

$$\frac{\partial \tilde{C}(\xi,\tau)}{\partial \tau} = \frac{\partial^2 \tilde{C}(\xi,\tau)}{\partial \xi^2} + \frac{\Phi}{\lambda}\frac{\partial \tilde{C}(\xi,\tau)}{\partial \xi} = 0, \tag{6.1}$$

with the boundary condition at $\xi = 0$,

$$\tilde{J}\Big|_{\xi=0} = \tilde{k}_{1f}\tilde{f}_{1f}(\tilde{C}(0)) - \tilde{k}_{1r}\tilde{f}_{1r}(\tilde{C}(0)), \tag{6.2}$$

and at $\xi{=}\lambda$,

$$\tilde{J}\Big|_{\xi=\lambda} = \tilde{k}_{2f}\tilde{f}_{2f}(\tilde{C}(\lambda)) - \tilde{k}_{2r}\tilde{f}_{2r}(\tilde{C}(\lambda)). \tag{6.3}$$

The rate constants in non-dimensional form are,

$$\tilde{k}_{1f} = \frac{k_{1f}^0 L_0}{DC_0}\exp\left(\frac{\alpha F \phi_{m/o}}{RT}\right), \tag{6.4}$$

$$\tilde{k}_{1r} = \frac{k_{1r}^0 L_0}{DC_0}\exp\left(\frac{\alpha F \phi_{o/m}}{RT}\right), \tag{6.5}$$

$$\tilde{k}_{2f} = \frac{k_{2f}^0 L_0}{DC_0}, \tag{6.6}$$

and

$$\tilde{k}_{2r} = \frac{k_{2r}^0 L_0}{DC_0}. \tag{6.7}$$

The forward (f) and reverse (r) interfacial kinetic functions at each interface are

$$\tilde{f}_{1f} = \frac{1}{2}(1 + \tanh(\Gamma(1 - \tilde{C}(0))), \tag{6.8}$$

and

$$\tilde{f}_{1r} = \frac{1}{2}(1 + \tanh(\Gamma(\tilde{C}(0) - 1)), \tag{6.9}$$

for the M-O interface, and

$$\tilde{f}_{2f} = \tilde{C}(\lambda), \tag{6.10}$$

and

$$\tilde{f}_{2r} = 1 - \tilde{C}(\lambda), \tag{6.11}$$

for the O-E interface. The oxide thickness equation is,

$$\frac{d\lambda(\tau)}{d\tau} = \tilde{\kappa}\tilde{f}_{1f}\tilde{C}(0) - \tilde{\kappa}_r\tilde{f}_{1r}\tilde{C}(0). \tag{6.12}$$

6.3 Model Solution

Since we are solving in the quasi-steady state limit, the same general solution to Equation 6.1 can be used as in the previous chapter,

$$\tilde{C}(\xi) = \tilde{a}\exp\left(-\frac{\Phi\xi}{\lambda}\right) + \tilde{b}, \tag{6.13}$$

where $\tilde{a}$ and $\tilde{b}$ are constants that depend on λ. Applying the full boundary conditions, the new equations for the integration constants are obtained,

$$-\frac{2\Phi\tilde{b}}{\lambda} = -\tilde{k}_{1f}\left(1 + \tanh\left(\Gamma\left(1 - \left(\tilde{a} + \tilde{b}\right)\right)\right)\right) + \tilde{k}_{1r}\left(1 + \tanh\left(\Gamma\left(\left(\tilde{a} + \tilde{b}\right) - 1\right)\right)\right), \tag{6.14}$$

and,

$$\tilde{b} = \frac{\tilde{k}_{2r} + (-\tilde{k}_{2f} - \tilde{k}_{2r})(\tilde{a}\exp(-\Phi)}{\frac{\Phi}{\lambda} + \tilde{k}_{2f} + \tilde{k}_{2r}}. \tag{6.15}$$

The integration constants are solved numerically at λ values from a defined layer thickness to zero as we are exploring the reduction case. The solution to the thickness

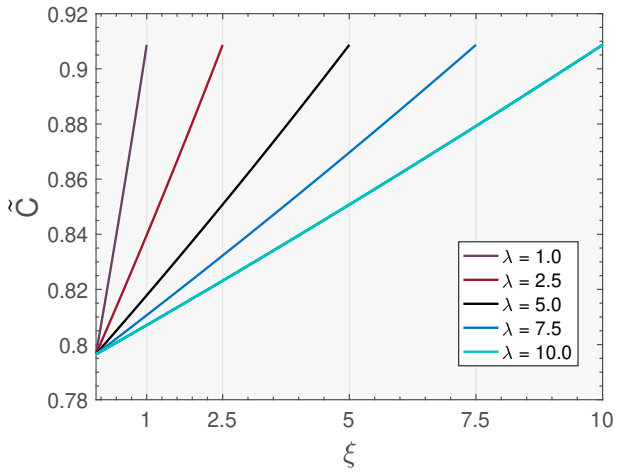

Figure 6.1: Oxygen vacancy concentration across the oxide layer as thickness is decreased. Parameters used are listed in Table 6.1.

of the oxide layer with time is solved using Equation 6.12 for λ and τ. This is done in MATLAB using the cumulative trapezoid numerical integration method.

6.3.1 Parametric Analysis

A parametric analysis was performed to explore the parameter space and analyze trends assessing the validity of the model assumptions. The same parameters were used as a starting point for each plot, as listed in Table 6.1. The model result indicated by the black line in the figures has the same parameter values across all figures and are the base values listed in Table 6.1. The same structural parameters were used as in Chapter 5. Figure 6.1 shows the variation of $\tilde{C}$ across the oxide layer as the layer is reduced. $\xi = 0$ represents the M-O interface whereas the value of $\xi = \lambda$ is at the O-E interface. It is clear the model is in the reduction phase because $\tilde{C}$ decreases from the O-E interface to the M-O interface. This is consistent with Figure 4.3; during reduction oxygen vacancies are created at the O-E interface, a surplus builds up, and the vacancies diffuse/migrate across the layer to the M-O interface where a platinum atom can be reduced. If k_{2r} is increased with the same rate of consumption, there is a higher concentration of defects and a steeper gradient across the layer as shown in Figure 6.2. As k_{2r} approaches k_{2f}, the gradient approaches zero indicating that the reaction across the O-E interface is in equilibrium with the oxygen vacancies being consumed and created.

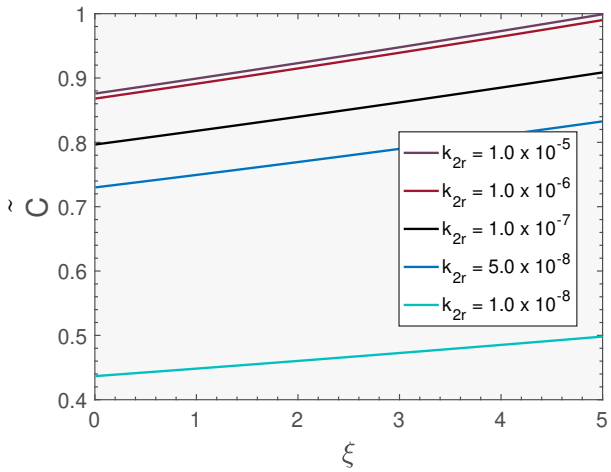

Figure 6.2: Oxygen vacancy concentration across the oxide layer as k_{2r} is increased. Parameters are listed in Table 6.1.

Figure 6.3 and Figure 6.4 shows the parametric effect of $\tilde{C}$ at the M-O interface as a function or λ. Figure 6.3a shows that $\tilde{C}$ at the M-O interface increases at a faster rate as λ is reduced and k_{1r} is increased indicating that a higher k_{1r} does indeed consume more $\tilde{C}$ at the M-O interface. Increasing k_{2r} does not have a significant effect on the consumption rate of $\tilde{C}$ at the M-O interface as the layer reduces as indicated by parallel lines in Figure 6.3. This is consistent with the assumption that the rate determining step is at the M-O interface. Figure 6.4 shows that as γ is increased, $\tilde{C}$ has a higher concentration at the M-O interface at the start of reduction and increases at slower rates as the layer is reduced. In the case of oxide growth, as was discussed in Section 4.4.1, the more realistic scenario is a very large γ value whereas in the case of reduction, it seems to be the opposite. Reduction occurs very rapidly compared to oxide growth, thus a steeper gradient of $\tilde{C}$ at the M-O interface vs thickness, as seen in Figure 6.4, will result in faster reduction kinetics.

Figure 6.5 shows how the oxide layer is reduced with varying rate constants across the M-O interface. The oxide layer reduces faster, taking less time to reach zero with a faster k_{1r} and reduces slower with faster k_{1f}. Figure 6.6 analyzes the reaction rates at the O-E interface. The first observation is that oxide reduction is less sensitive to changes in the rate across the O-E interface compared to changes in the rates across the M-O interface. For example, a four-order of magnitude increase of either the forward or reverse reaction rate across the O-E interface equates to only a 2000 time-step difference to reach zero thickness whereas in looking at the rates across

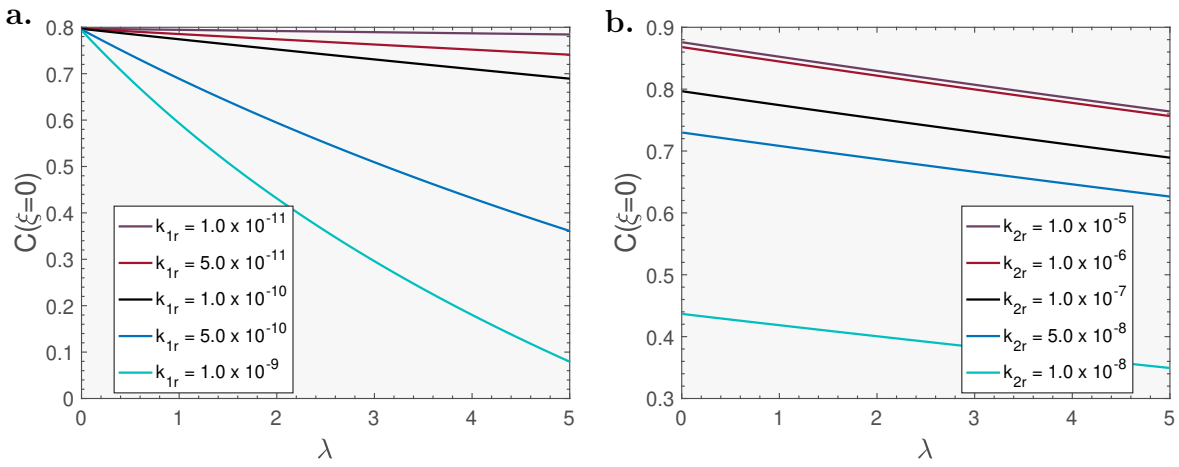

Figure 6.3: Oxygen vacancy concentration at the M-O interface as a.) k_{1r} and b.) k_{2r} is increased. Parameters are listed in Table 6.1.

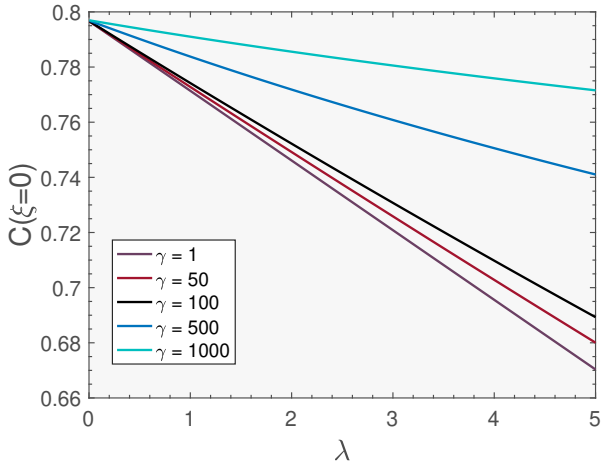

Figure 6.4: Oxygen vacancy concentration at the M-O interface as γ is increased. Parameters are listed in Table 6.1.

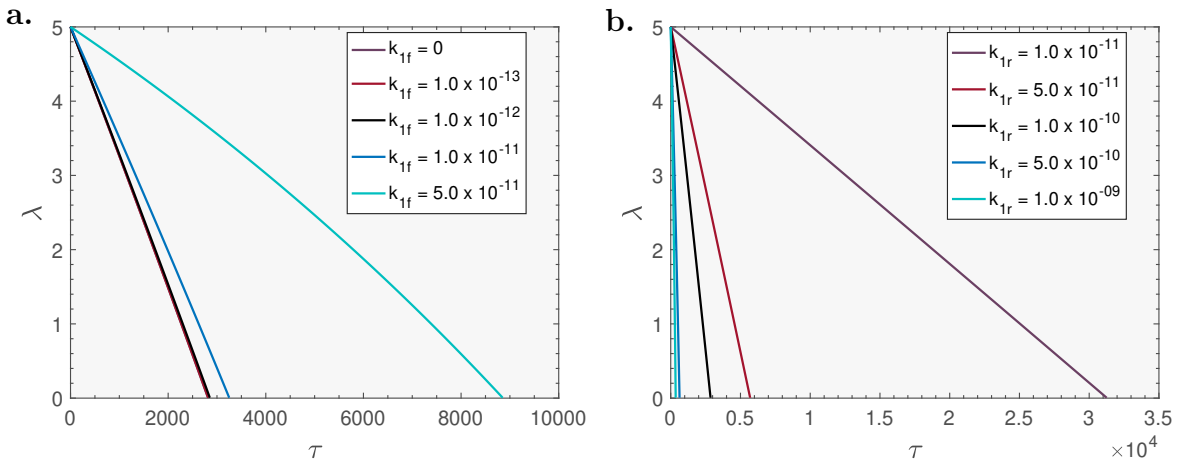

Figure 6.5: Parametric analysis of oxide layer thickness during reduction as a function of τ for a.) varied k_{1f} and b.) k_{1r}. Parameters are listed in Table 6.1.

the M-O interface, increasing the rates by even two-orders of magnitude results in over a 5000 time-step change for the forward reaction and roughly 3000 time-steps for the reverse. This is consistent with the reactions at the M-O interface to be rate determining because changes in k_{1f} and k_{1r} have a more significant effect on the overall rate of the reaction. There is an increase in the reduction time for decreasing k_{2r} as expected.

As previously discussed, one of the model assumptions was that the potential difference across the layer stays constant as the thickness changes and only the gradient of the potential changes. From Figure 6.7a, it is seen there is a measurable effect in the reduction time with changing $\Delta\phi$ across the layer. This shows relaxing this assumption may have an important effect on the overall oxide reduction time. Figure 6.7b shows that as γ is increased, the time to reduce the oxide layer increases.

6.3.2 Comparison to Experimental Data

For preliminary results, the model is compared to experimental data in Figure 6.9. This was a very rudimentary study simply to assess the trends thus it is stressed that the parameters can not be taken as absolutes. The experimental data in Figure 6.9a was taken from Ref. [8] and are based on the coordination number of Pt-O bonds. Thus the model assumes the number of Pt-O bonds is proportional to the thickness of the oxide layer. Tada *et al.* used time-gating quick X-ray adsorption fine structure spectroscopy (TG-QEXAFS) to monitor the chemical bonds directly [8]. The experimental data in Figure 6.9b was extracted from Ref. [9]. Allen *et al.* used a

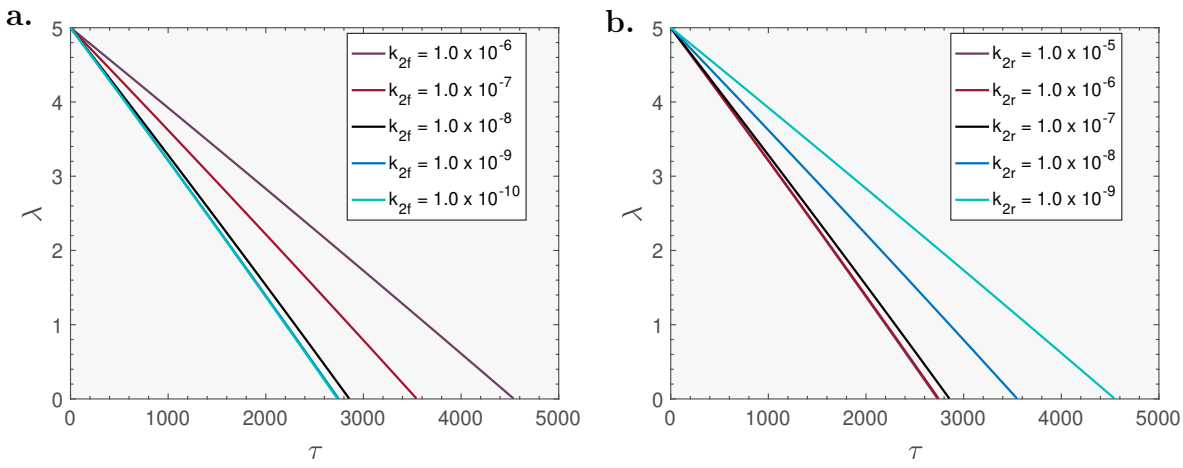

Figure 6.6: Parametric analysis of oxide layer thickness during reduction as a function of τ for a.) varied k_{2f} and b.) k_{2r}. Parameters are listed in Table 6.1.

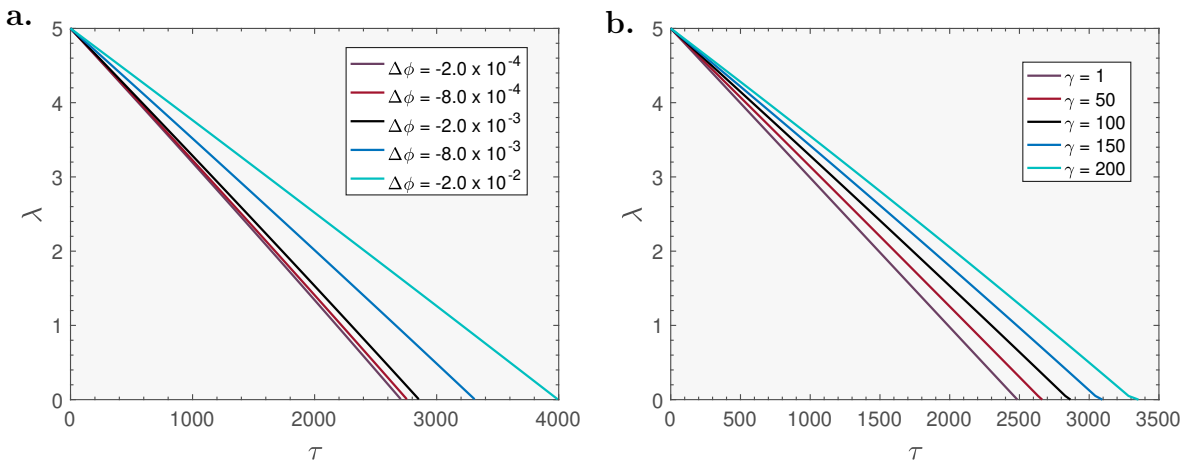

Figure 6.7: Parametric analysis of oxide layer thickness during reduction as a function of τ for a.) varied $\Delta\phi$ and b.) γ. Parameters are listed in Table 6.1.

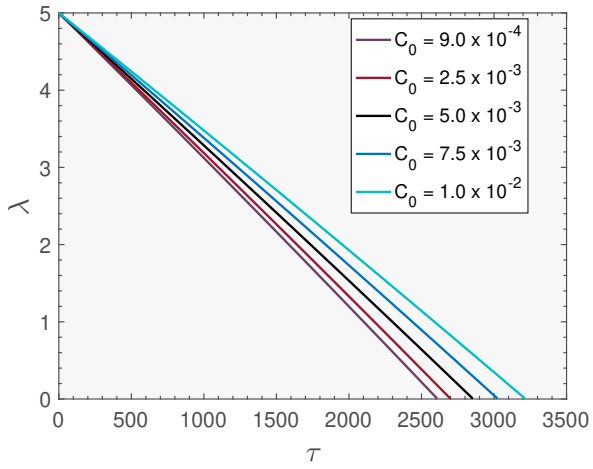

Figure 6.8: Parametric analysis of oxide layer thickness during reduction as a function of τ for varied C_0. Parameters are listed in Table 6.1.

Symbol	Units	
T	K	353
$\Delta\phi$	V	-0.002
D	$\text{cm}^2\ \text{s}^{-1}$	1.0×10^{-14}
L_0	cm	2.7×10^{-8}
k_{1f}	$\text{mol cm}^{-2}\ \text{s}^{-1}$	1.0×10^{-12}
k_{1r}	$\text{mol cm}^{-2}\ \text{s}^{-1}$	1.0×10^{-10}
k_{2f}	$\text{mol cm}^{-2}\ \text{s}^{-1}$	1.0×10^{-8}
k_{2r}	$\text{mol cm}^{-2}\ \text{s}^{-1}$	1.0×10^{-7}
C_0	mol cm^{-3}	5.0×10^{-3}
γ	$\text{cm}^3\ \text{mol}^{-1}$	100
ϵ	mol cm^{-3}	0.066

Table 6.1: Table of general parameter values for Section 6.3.1.

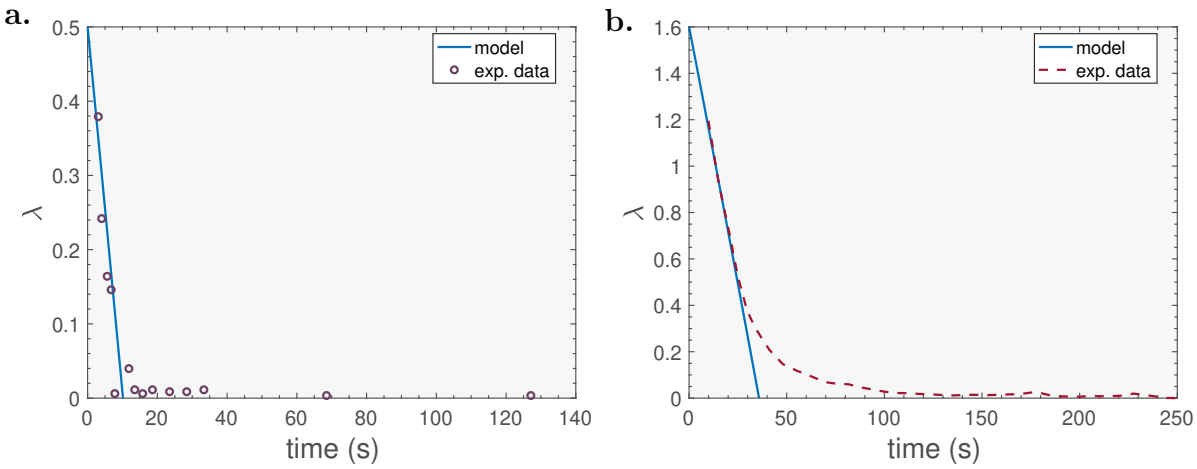

Figure 6.9: Model results applied to experimental data reported from a.) Ref. [8] and b.) Ref. [9]. The model parameters are listed in Table 6.2.

similar method as Tada *et al.* based on time-resolved X-ray absorption spectroscopy to determine the number of oxygen atoms with time. Table 6.2 presents the parameters for Figure 6.9 and shows the model can capture the two curves by simply changing k_{1r} and the starting thickness of the layer; this is expected as the experimental procedure and conditions were similar.

The presented reduction model captures the first part of the curve but fails as the oxide layer becomes very thin. The reason for this comes back to the assumption that the defect density is very small. As the oxide layer becomes highly depleted in oxygen, reduction kinetics will be limited by the amount of oxygen concentration still incorporated in the layer resulting in an exponential thickness decay.

6.4 Transient Solution

This section is intended to propose a possible route forward to solving the full transient solution to the coupled oxide growth and reduction model. Using the steady-state assumption, as well as the assumption that the potential difference across the layer is not a function of thickness, allowed for the general solution of the transport equation to be applied. There is no general solution to the transport equation if either of these assumptions are relaxed. However, using the finite difference method, a numerical solution is possible. Ref. [125] outlines an efficient procedure to solve the coupled Nernst-Planck and Poisson equation system using the finite difference approach. The approach was applied again in Ref. [126]. The method solves the transport equation

Symbol	Units	a. Ref. [8]	b. Ref. [9]
T	K	353	353
$\Delta\phi$	V	-0.002	-0.002
D	$cm^2\ s^{-1}$	1.0×10^{-14}	1.0×10^{-14}
L_0	cm	2.7×10^{-8}	2.7×10^{-8}
k_{1f}	$mol\ cm^{-2}\ s^{-1}$	1.0×10^{-12}	1.0×10^{-12}
k_{1r}	$mol\ cm^{-2}\ s^{-1}$	6.5×10^{-10}	6.0×10^{-10}
k_{2f}	$mol\ cm^{-2}\ s^{-1}$	1.0×10^{-8}	1.0×10^{-8}
k_{2r}	$mol\ cm^{-2}\ s^{-1}$	1.0×10^{-7}	1.0×10^{-7}
C_0	$mol\ cm^{-3}$	5.0×10^{-3}	5.0×10^{-3}
γ	$cm^3\ mol^{-1}$	100	100
ϵ	$mol\ cm^{-3}$	0.066	0.066

Table 6.2: Table of general parameter values for model comparison to experimental data for Figure 6.9.

coupled with the Poisson equation for a system with fixed boundaries. First the equations are outlined for a single thickness, then a way to expand the system of equations to include a moving boundary is discussed.

The implicit finite difference form of Equations 4.35, 4.36, and 4.38 are

$$\frac{\tilde{C}_i^{n+1}-\tilde{C}_i^n}{\Delta\tau} = -\frac{\tilde{J}_i^n-\tilde{J}_{i-1}^n}{(\xi_{i+1}-\xi_{i-1})/2}, \tag{6.16}$$

$$\tilde{J} = -\left(\frac{\tilde{C}_{i+1}^n-\tilde{C}_i^n}{\Delta\xi}\right) - \tilde{C}_i^n\tilde{E}_i^n, \tag{6.17}$$

and

$$\frac{\tilde{E}_{i+1}^n-\tilde{E}_i^n}{\Delta\xi} = -Z\tilde{C}_i^n, \tag{6.18}$$

where subscript i denotes distance grid point and superscript n denotes time level. Combining the flux and continuity and applying boundary conditions leads to the following solutions, for i = 1,

$$\frac{\tilde{C}_1^{n+1}-\tilde{C}_1^n}{\Delta\tau} = -\frac{1}{(\xi_2-\xi_0)/2}\left[\left(-\frac{\tilde{C}_2^n-\tilde{C}_1^n}{\xi_2-\xi_1} - \frac{\tilde{C}_2^n-\tilde{C}_1^n}{2}\tilde{E}_1^n\right) - \left(\tilde{J}_1^n\right)\right] \tag{6.19}$$

for $2 \leq i \leq N-1$,

$$\frac{\tilde{C}_i^{n+1} - \tilde{C}_i^n}{\Delta\tau} = -\frac{1}{(\xi_{i+1} - \xi_{i-1})/2} \left[\left(-\frac{\tilde{C}_{i+1}^n - \tilde{C}_i^n}{\xi_{i+1} - \xi_i} - \frac{\tilde{C}_{i+1}^n - \tilde{C}_i^n}{2} \tilde{E}_i^n \right) - \left(\frac{\tilde{C}_i^n - \tilde{C}_{i-1}^n}{\xi_{i+1} - \xi_i} - \frac{\tilde{C}_i^n - \tilde{C}_{i-1}^n}{2} \tilde{E}_{i-1}^n \right) \right] \quad (6.20)$$

for i = N,

$$\frac{\tilde{C}_N^{n+1} - \tilde{C}_N^n}{\Delta\tau} = -\frac{1}{(\xi_{N+1} - \xi_{N-1})/2} \left[\left(\tilde{J}_N^n \right) - \left(\frac{\tilde{C}_N^n - \tilde{C}_{N-1}^n}{\xi_{N+1} - \xi_N} - \frac{\tilde{C}_N^n - \tilde{C}_{N-1}^n}{2} \tilde{E}_{N-1}^n \right) \right] \quad (6.21)$$

And for the fields: for j = 0,

$$\frac{\tilde{E}_0^{n+1} - \tilde{E}_0^n}{\Delta\xi} = -\tilde{\alpha} \quad (6.22)$$

for $2 \leq j \leq N-1$,

$$\frac{\tilde{E}_j^{n+1} - \tilde{E}_j^n}{\Delta\xi} = -Z\tilde{C}_i^n \quad (6.23)$$

for j = N,

$$\frac{\tilde{E}_N^{n+1} - \tilde{E}_N^n}{\Delta\xi} = 0. \quad (6.24)$$

The boundary conditions in implicit form become, at $\xi = 0$,

$$\tilde{J}_1^n = -\tilde{k}_{1f}\frac{1}{2}(1 + \tanh(\Gamma(1 - \tilde{C}_1^n))) + \tilde{k}_{1r}\frac{1}{2}(1 + \tanh(\Gamma(\tilde{C}_1^n - 1))), \quad (6.25)$$

and at $\xi = \lambda$

$$\tilde{J}_N^n = -\tilde{k}_{2f}\tilde{C}_N^n + \tilde{k}_{2r}(1 - \tilde{C}_N^n). \quad (6.26)$$

The system of equations above can be implemented into a program and output the results for concentration change across a layer of defined thickness provided the initial condition is defined. The tricky part will be figuring out how to include the moving boundary condition. The idea is to set up an extensive matrix that defines space and time where the solution to a finite thickness begins somewhere in the middle of the first row. For example, have a matrix of i columns that define the space and n rows that define the time. Have the first section of columns zeros and define i = 100 as the initial M-O interface; this way the moving boundary can shift into the metal without having negative index values. There needs to be at initial oxygen vacancy

concentration across the layer at zero time, assumably a very thin layer with uniform concentration, as time proceeds, the oxygen vacancy concentration across the layer would change due to boundary conditions and the model equations, which would result in either growth or reduction and provide the initial inputs and boundary condition for the solution at the next time step. This is a theoretical procedure that has not been tested, but would allow the full transient model to be solved.

6.5 Summary and Outlook

In this chapter, a solution was presented for a steady state case of platinum oxide reduction. A parametric study was performed that successfully captured expected trends indicating that the model, albeit simple, captures crucial aspects of platinum reduction. It was shown that the model solution is more sensitive to the rate constants at the M-O interface compared to the O-E interface. The model was shown to capture experimental trends reasonably well at thicker layers when the concentration of oxygen vacancies is small and the reduction is controlled by diffusion. The model diverges from experimental trends at small thicknesses of the oxide layer.

The next step is to apply the outlined finite difference approach. As has been discussed, a significant amount of platinum dissolution occurs during oxide reduction. Although this has not yet been incorporated into the model, there has been progress made towards this inclusion. This would be the ultimate step to tie everything together.

Chapter 7

Conclusion

7.1 Overview of Main Results

Platinum stability in the cathode catalyst layer plays a vital role in guaranteeing sufficient lifetime standards of fuel cell vehicles in the ongoing commercialization efforts. This thesis provides mathematical models to aid the understanding of degradation mechanisms driving the deterioration of the catalyst layer. The thesis is broken into three parts to work towards this goal. Part one focuses on the degradation mechanisms; part two is on the platinum oxide layer formation and growth and part three incorporates platinum oxide reduction.

For part one, a step-wise algorithm is presented to analyze degradation data. The statistical physics-based model uses experimental inputs to determine a unique set of rate constants for the pertinent degradation mechanisms namely platinum dissolution and redeposition, coagulation, and detachment. Moreover, it includes the effluence of platinum into the membrane. Parameters are obtained by simultaneously fitting electrochemical active surface area loss, mean particle radius, and platinum-in-the-membrane loss. To obtain unique, unambiguous results, independent of the initial model guess, the algorithm proceeds in two stages. The intent of STAGE I is to survey the narrowed parameter space using Monte Carlo sampling. The outputs from STAGE I are then used as inputs for the optimization routine in STAGE II.

The experimental data compared consisted of varying potential cycling protocols and carbon support type. From the model results it is seen that the derived rate constants for dissolution and detachment increase with the upper potential limit of potential cycling, ϕ_{UPL}. The detachment rate constant increases with the surface area of the carbon support whereas the dissolution rate constant appears to be independent of the support. Dissolution/redeposition was seen to be the dominant degradation

mechanism at $\phi_{\mathrm{UPL}} = 1.0\ \mathrm{V_{RHE}}$ for Medium Surface Area Carbon whereas coagulation and detachment contribute more significantly at $\phi_{\mathrm{UPL}} = 1.3\ \mathrm{V_{RHE}}$. A similar trend is seen for Low Surface Area Carbon support except coagulation and are seen to contribute equally to dissolution/redeposition. More experimental data is needed to confidently determine if this is a coincidence or if a lower surface area support is more prone to coagulation at lower UPLs.

A mathematical model of oxide formation, growth, and reduction was developed to gain deeper insight into degradation via dissolution. A quasi-steady state model of oxide formation and growth was introduced. Although many oxide growth models have been developed over the last several decades, the presented model is new in that it uses a functional form for the interfacial kinetics that drives the growth mechanism. Moreover, it was applied to a diverse range of experimental studies, as well as various metals. It proved robust by successfully capturing the diverse range of growth laws presented in the literature.

It was seen that oxide growth is highly sensitive to the oxygen ion vacancy density at the metal-oxide interface. The reaction rate at the metal-oxide interface was shown to decrease as the UPL was increased, which is expected as the growth of the oxide layer slows the thicker it becomes.

The reduction of the platinum oxide layer is the key to understanding the fundamentals of the dissolution mechanism. But this is not a trivial task due to the complexity of the structural changes the oxide layer undergoes resulting in unpredictable electronic characteristics. The first attempt to add the reduction phenomena to the oxide formation and growth model was to add the reverse reaction to the boundary condition while keeping the quasi-steady state approach. It is expected that the oxide growth and reduction model would perform best in the limit of a thick oxide since the model framework is based on the Nernst-Planck equation. However, it also seems to perform seemingly well at thin (below one monolayer) oxide layers. This shows that in the thin layer limit, the oxidation or reduction kinetics are controlled by interfacial rates of reaction and the transport effects not captured by the model in this limit are insignificant.

Despite the robustness of the developed model on the oxidation and reduction of platinum, there are several limitations that must be noted. As was discussed throughout, the model is only valid in the limit of very low defect density. The model is not applicable at high defect density because the thickness is no longer simply controlled by transport and migration of the defects, but other mechanisms will have an effect such as a collapse of the platinum skeleton lattice. The diffusion coefficient must be

high in the steady state approximation such that the species cross the oxide layer rapidly compared to the rate of reaction at the M-O interface. Another limitation of the model is the assumption that potential difference across the layer does not change as the layer grows or reduces, as well as the potential gradient across the layer is a linear function of the thickness. Potential is known to have a significant effect on the oxidation and reduction phenomenon. The model incorporates a potential dependence in the reaction rates but the potential is not time or position dependent.

Solving a fully transient variant of the oxidation and reduction model would address some of the aforementioned limitations. An approach was outlined to obtain the transient solution to the coupled oxide growth and reduction model using a finite difference approach. This version of the model has not yet been fully solved.

7.2 Significant Contributions

Some of the specific contributions of this thesis to the scientific community are as follows:

1. We expanded the coupled model of the four degradation mechanisms (dissolution, redeposition, coagulation, and detachment) to include the effluence of platinum ions to the membrane.

2. An algorithm was developed that resolves the ambiguities in the mechanistic rate constants of the coupled degradation model previously published.

3. To the best of the author's knowledge, the step-wise degradation algorithm is the first attempt to fit such an extensive set of data with a statistical physics-based modelling approach by simultaneously fitting ECSA loss, mean particle radius, PITM loss, and catalyst layer thickness loss.

4. The oxide formation and growth model uses a novel interfacial kinetic rate function to describe a wide range of growth laws presented in the literature, as well as different metals.

5. A model of reduction was coupled to the model of oxide formation and growth to show which factors control oxide growth and oxide reduction.

With these tools, it is possible for R&D personnel in academia or industry to perform reliable assessments of degradation mechanisms under various operating condi-

tions and cycling protocols in order to understand how to mitigate or reduce degradation in PEFCs.

For example, being able to obtain precisely and uniquely defined parameters of different degradation mechanisms is the prerequisite for performing comparative analysis of different catalyst or support materials, as well as analyze sensitivities of materials stability to operating conditions. The ability to deconvolute degradation mechanisms and assess their relative contributions, enabled by the model-based analysis, is important in order to set priorities in terms of materials research, e.g., in view of the following questions: is it more important to find more stable catalysts or more stable supports?

7.3 Future Research Paths

For any good model there is always the question of needing more data or a better model. It is important to highlight the shortcomings of each and discuss potential future paths forward. More experimental data are needed to further resolve some inconclusiveness acquired in the analysis for the degradation model. For example, there is still not a clear trend to the redeposition rate, as well as it is unclear if there is a contribution from the coagulation mechanism at lower upper potential limit for Low Surface Area Carbon supports, while there is none for Medium Surface Area Carbon supports. Ideally, experimental studies on High Surface Area Carbon should be expanded such that we could include a full analysis to compare with Medium Surface Area Carbon and Low Surface Area Carbon. Most importantly, extending the experimental data to add more data intermediate points during the degradation testing for mean surface area, platinum loss to the membrane, and catalyst thickness for all data sets would allow for more confidence in the entire results compared to just the initial and final data point.

There are limitations of the degradation model that could be improved on as well. Two points are computational time and the lack of trend seen between several rate constants including platinum-loss-in-the-membrane and redeposition. A suggestion to solve these issues would be to develop a machine learning algorithm that implements a neural network. This would hypothetically reduce the computational time, but more experimental data would be needed to apply such an approach.

In the case of the platinum oxidation and reduction model, the major next step would be to solve the fully transient case. This would allow Poisson's equation to be included to account for time-dependent changes of the potential difference across the

layer that are coupled to the reactions at each interface. The steady state assumption could be relaxed relieving several of the restrictions including the requirement of a very small defect density. This would allow for broader oxidizing and reducing conditions to be explored, as well as a coupled solution that incorporates growth and reduction in a single run enabling the simulations of features seen in cyclic voltammetry.

The ultimate goal of the PhD work was to link the dissolution degradation mechanism to the platinum oxide formation, growth, and reduction phenomena. Although significant progress has been made towards understanding oxide layer growth and reduction, the link to dissolution of platinum is not established. A deeper understanding of the reduction process is necessary to develop a method to couple the process to the degradation rates. One idea to couple the models (once expanded) would be to correlate under-coordinated platinum atoms during the oxide reduction process to the rate of dissolution that is determined from the degradation model while accounting for the platinum mass balance. This would allow for interesting analysis of how the dissolution mechanism is directly effected by the growth and reduction of the oxide.

Bibliography

[1] Y. Sugawara, T. Okayasu, A. P. Yadav, A. Nishikata, and T. Tsuru, "Dissolution mechanism of platinum in sulfuric acid solution," *Journal of the Electrochemical Society*, vol. 159, pp. F779–F786, sep 2012.

[2] A. A. Topalov, I. Katsounaros, M. Auinger, S. Cherevko, J. C. Meier, S. O. Klemm, and K. J. J. Mayrhofer, "Dissolution of platinum: limits for the deployment of electrochemical energy conversion?," *Angewandte Chemie (International ed. in English)*, vol. 51, pp. 12613–5, dec 2012.

[3] H. Imai, K. Izumi, M. Matsumoto, Y. Kubo, K. Kato, and Y. Imai, "In situ and real-time monitoring of oxide growth in a few monolayers at surfaces of platinum nanoparticles in aqueous media.," *Journal of the American Chemical Society*, vol. 131, pp. 6293–300, May 2009.

[4] A. T. Fromhold, "Metal oxidation kinetics from the viewpoint of a physicist: The microscopic motion of charged defects through oxidest," *Langmuir*, vol. 3, pp. 886–896, 1987.

[5] Y. Furuya, T. Mashio, A. Ohma, N. Dale, K. Oshihara, and G. Jerkiewicz, "Surface oxide growth on platinum electrode in aqueous trifluoromethanesulfonic acid," *The Journal of Chemical Physics*, vol. 141, p. 164705, 2014.

[6] M. J. Graham, S. I. Ali, and M. Cohen, "Low temperaure oxdation (24° to 200°C) and Krypton Adsorption studies on polycrystalline and single crystal iron surfaces," *Journal of The Electrochemical Society*, vol. 117, no. 4, pp. 513–516, 1970.

[7] M. Alsabet, M. Grden, and G. Jerkiewicz, "Electrochemical Growth of Surface Oxides on Nickel . Part 2 : Formation of β -Ni (OH) 2 and NiO in Relation to the Polarization Potential , Polarization Time , and Temperature," *Electrocatalysis*, vol. 5, pp. 136–147, 2014.

[8] M. Tada, S. Murata, T. Asakoka, K. Hiroshima, K. Okumura, H. Tanida, T. Uruga, H. Nakanishi, S. I. Matsumoto, Y. Inada, M. Nomura, and Y. Iwasawa, "In situ time-resolved dynamic surface events on the Pt/C cathode in a fuel cell under operando conditions," *Angewandte Chemie - International Edition*, vol. 46, no. 23, pp. 4310–4315, 2007.

[9] P. G. Allen, S. D. Conradson, M. S. Wilson, S. Gottesfeld, I. D. Raistrick, J. Valerio, and M. Lovato, "Direct observation of surface oxide formation and reduction on platinum clusters by time-resolved X-ray absorption spectroscopy," *Journal of Electroanalytical Chemistry*, vol. 384, no. 1-2, pp. 99–103, 1995.

[10] British Petroleum, "BP statistical review of world energy 2017," *British Petroleum*, no. 66, pp. 1–52, 2017.

[11] S. Bilgen, "Structure and environmental impact of global energy consumption," *Renewable and Sustainable Energy Reviews*, vol. 38, pp. 890–902, 2014.

[12] M. Azhar Khan, M. Zahir Khan, K. Zaman, and L. Naz, "Global estimates of energy consumption and greenhouse gas emissions," *Renewable and Sustainable Energy Reviews*, vol. 29, pp. 336–344, 2014.

[13] B. Honisch, A. Ridgwell, D. N. Schmidt, E. Thomas, S. J. Gibbs, A. Sluijs, R. Zeebe, L. Kump, R. C. Martindale, S. E. Greene, W. Kiessling, J. Ries, J. C. Zachos, D. L. Royer, S. Barker, T. M. J. Marchitto, R. Moyer, C. Pelejero, P. Ziveri, G. L. Foster, and B. Williams, "The geological record of ocean acidification," *Science*, vol. 335, no. March, pp. 1058–1063, 2012.

[14] A. J. Cohen, M. Brauer, R. Burnett, H. R. Anderson, J. Frostad, K. Estep, K. Balakrishnan, B. Brunekreef, L. Dandona, R. Dandona, V. Feigin, G. Freedman, B. Hubbell, A. Jobling, H. Kan, L. Knibbs, Y. Liu, R. Martin, L. Morawska, C. A. Pope, H. Shin, K. Straif, G. Shaddick, M. Thomas, R. van Dingenen, A. van Donkelaar, T. Vos, C. J. L. Murray, and M. H. Forouzanfar, "Estimates and 25-year trends of the global burden of disease attributable to ambient air pollution: an analysis of data from the Global Burden of Diseases Study 2015," *The Lancet*, vol. 389, no. 10082, pp. 1907–1918, 2017.

[15] H. Hao, Y. Geng, and J. Sarkis, "Carbon footprint of global passenger cars: Scenarios through 2050," *Energy*, vol. 101, pp. 121–131, 2016.

[16] G. Collantes and D. Sperling, "The origin of California's zero emission vehicle mandate," *Transportation Research Part A: Policy and Practice*, vol. 42, no. 10, pp. 1302–1313, 2008.

[17] J. M. Andújar and F. Segura, "Fuel cells: History and updating. A walk along two centuries," *Renew Sust Energ Rev*, vol. 13, no. 9, pp. 2309–2322, 2009.

[18] U. Eberle, B. Müller, and R. von Helmolt, "Fuel cell electric vehicles and hydrogen infrastructure: status 2012," *Energ Environ Sci*, vol. 5, no. 10, pp. 8780–8798, 2012.

[19] S. Campanari, G. Manzolini, and F. Garcia de la Iglesia, "Energy analysis of electric vehicles using batteries or fuel cells through well-to-wheel driving cycle simulations," *Journal of Power Sources*, vol. 186, no. 2, pp. 464–477, 2009.

[20] R. Borup, J. Meyers, B. S. Pivovar, Y. S. Kim, R. Mukundan, N. Garland, D. Myers, M. Wilson, F. Garzon, D. Wood, P. Zelenay, K. More, K. Stroh, T. Zawodzinski, X. J. Boncella, J. E. Mcgrath, O. M. Inaba, K. Miyatake, M. Hori, K. Ota, Z. Ogumi, S. Miyata, A. Nishikata, Z. Siroma, Y. Uchimoto, K. Yasuda, K.-i. Kimijima, and N. Iwashita, "Scientific aspects of polymer electrolyte fuel cell durability and degradation," *Chem Rev*, no. 107, pp. 3904–3951, 2007.

[21] S. J. C. Cleghorn, D. K. Mayfield, D. A. Moore, J. C. Moore, G. Rusch, T. W. Sherman, N. T. Sisofo, and U. Beuscher, "A polymer electrolyte fuel cell life test: 3 years of continuous operation," *J Power Sources*, vol. 158, no. 1, pp. 446–454, 2006.

[22] S. Hirano and D. Papageorgopoulos, "Fuel cell technical team roadmap," *U. S. Drive Partnership*, no. June, pp. 1–26, 2013.

[23] V. McConnell, "Military UAVs claiming the skies with fuel cell power," *Fuel Cells Bulletin*, no. December, 2007.

[24] O. Z. Sharaf and M. F. Orhan, "An overview of fuel cell technology : Fundamentals and applications," *Renew Sust Energ Rev*, vol. 32, pp. 810–853, 2014.

[25] J. Wu, X. Z. Yuan, J. J. Martin, H. Wang, J. Zhang, J. Shen, S. Wu, and W. Merida, "A review of PEM fuel cell durability: Degradation mechanisms and mitigation strategies," *J Power Sources*, vol. 184, no. 1, pp. 104–119, 2008.

[26] E. P. A. 2016, *Light-duty automotive technology, carbon dioxide emissions, and fuel economy trends: 1975 through 2016*. EPA-420-R-16-010, Office of Transportation and Air Quality, November 2016.

[27] A. Alaswad, A. Baroutaji, H. Achour, J. Carton, A. Al Makky, and A. G. Olabi, "Developments in fuel cell technologies in the transport sector," *International Journal of Hydrogen Energy*, vol. 41, no. 37, pp. 16499–16508, 2015.

[28] M. Eikerling and A. Kulikovsky, *Polymer electrolyte fuel cells: physical principles of materials and operation*. Boca Raton: Taylor & Francis Group, 2015.

[29] E. Antolini, "Carbon supports for low-temperature fuel cell catalysts," *Applied Catalysis B: Environmental*, vol. 88, no. 1-2, pp. 1–24, 2009.

[30] M. Uchida, "Effects of microstructure of carbon support in the catalyst layer on the performance of polymer-electrolyte fuel cells," *Journal of The Electrochemical Society*, vol. 143, no. 7, p. 2245, 1996.

[31] T. Soboleva, X. Zhao, K. Malek, Z. Xie, T. Navessin, and S. Holdcroft, "On the micro-, meso-, and macroporous structures of polymer electrolyte membrane fuel cell catalyst layers," *ACS Applied Materials and Interfaces*, vol. 2, no. 2, pp. 375–384, 2010.

[32] A. Patel, K. Artyushkova, P. Atanassov, D. Harvey, M. Dutta, V. Colbow, and S. Wessel, "Effect of graphitic content on carbon supported catalyst performance," *ECS Transactions*, vol. 41, no. 1, pp. 845–852, 2011.

[33] S. Wessel and D. Harvey, "Development of micro-structural mitigation strategies for pem fuel cells: Morphological simulations and experimental approach," tech. rep., DOE's Offic of Scientific and Technical Information (OSTI), January 2013.

[34] X. Wang, W. Li, Z. Chen, M. Waje, and Y. Yan, "Durability investigation of carbon nanotube as catalyst support for proton exchange membrane fuel cell," *Journal of Power Sources*, vol. 158, no. 1, pp. 154–159, 2006.

[35] X. Yu and S. Ye, "Recent advances in activity and durability enhancement of Pt/C catalytic cathode in PEMFC," *Journal of Power Sources*, vol. 172, pp. 145–154, oct 2007.

[36] A. Patel, K. Artyushkova, A. Young, M. Dutta, Z. Ahmad, V. Colbow, S. Wessel, and S. Ye, "Structural and morphological properties of carbon supports: Effect on catalyst degradation," *ECS Transactions*, vol. 33, no. 1, pp. 425–431, 2010.

[37] A. J. Medford, A. Vojvodic, J. S. Hummelshøj, J. Voss, F. Abild-pedersen, F. Studt, T. Bligaard, A. Nilsson, and J. K. Nørskov, "From the Sabatier principle to a predictive theory of transition-metal heterogeneous catalysis," *Journal of Catalysis*, vol. 328, pp. 36–42, 2015.

[38] J. K. Nørskov, J. Rossmeisl, A. Logadottir, L. Lindqvist, and H. Jo, "Origin of the overpotential for oxygen reduction at a fuel-cell cathode," *Journal of Physical Chemistry B*, vol. 108, pp. 17886–17892, 2004.

[39] H. A. Gasteiger, S. S. Kocha, B. Sompalli, and F. T. Wagner, "Activity benchmarks and requirements for Pt, Pt-alloy, and non-Pt oxygen reduction catalysts for PEMFCs," *Applied Catalysis B: Environmental*, vol. 56, pp. 9–35, mar 2005.

[40] N. G. Moreno, M. C. Molina, D. Gervasio, and J. F. P. Robles, "Approaches to polymer electrolyte membrane fuel cells (PEMFCs) and their cost," *Renewable and Sustainable Energy Reviews*, vol. 52, pp. 897–906, 2015.

[41] O. Gröger, H. A. Gasteiger, and J.-P. Suchsland, "Review—electromobility: batteries or fuel cells?," *J Electrochem Soc*, vol. 162, no. 14, pp. A2605–A2622, 2015.

[42] J. C. Meier, C. Galeano, I. Katsounaros, J. Witte, H. J. Bongard, A. A. Topalov, C. Baldizzone, S. Mezzavilla, F. Schuth, and K. J. J. Mayrhofer, "Design criteria for stable Pt/C fuel cell catalysts," *Beilstein J Nanotech*, vol. 5, no. 1, pp. 44–67, 2014.

[43] F. Ettingshausen, J. Kleemann, A. Marcu, G. Toth, H. Fuess, and C. Roth, "Dissolution and migration of platinum in PEMFCs investigated for start / stop cycling and high potential degradation," *Fuel Cells*, no. 2, pp. 238–245, 2011.

[44] S. Cherevko, N. Kulyk, and K. J. J. Mayrhofer, "Durability of platinum-based fuel cell electrocatalysts: Dissolution of bulk and nanoscale platinum," *Nano Energy*, vol. 29, pp. 275–298, 2016.

[45] Y. Furuya, T. Mashio, A. Ohma, M. Tian, F. Kaveh, D. Beauchemin, and G. Jerkiewicz, "Influence of electrolyte composition and pH on platinum electrochemical and/or chemical dissolution in aqueous acidic media," *ACS Catal*, vol. 5, no. 4, pp. 2605–2614, 2015.

[46] A. A. Topalov, S. Cherevko, A. R. Zeradjanin, J. C. Meier, I. Katsounaros, and K. J. J. Mayrhofer, "Towards a comprehensive understanding of platinum dissolution in acidic media," *Chemical Science*, vol. 5, no. 2, p. 631, 2014.

[47] P. Urchaga, T. Kadyk, S. G. Rinaldo, A. O. Pistono, J. Hu, W. Lee, C. Richards, M. H. Eikerling, and C. A. Rice, "Catalyst degradation in fuel cell electrodes: Accelerated stress tests and model-based analysis," *Electrochimica Acta*, vol. 176, pp. 1500–1510, 2015.

[48] X. Wang, R. Kumar, and D. J. Myers, "Effect of voltage on platinum dissolution," *Electrochem Solid St*, vol. 9, no. 5, pp. A225–A227, 2006.

[49] J. Monzó, D. F. van der Vliet, A. Yanson, and P. Rodriguez, "Elucidating the degradation mechanism of the cathode catalyst of PEFCs by a combination of electrochemical methods and X-ray fluorescence spectroscopy," *Phys Chem Chem Phys*, vol. 18, no. 32, pp. 22407–22415, 2016.

[50] Y. Shao-Horn, W. C. Sheng, S. Chen, P. J. Ferreira, E. F. Holby, and D. Morgan, "Instability of supported platinum nanoparticles in low-temperature fuel cells," *Top Catal*, vol. 46, no. 3-4, pp. 285–305, 2007.

[51] L. Xing, M. A. Hossain, M. Tian, D. Beauchemin, K. Adjemian, and G. Jerkiewicz, "Platinum electro-dissolution in acidic media upon potential cycling," *Electrocatalysis*, vol. 5, pp. 96–112, Nov. 2013.

[52] S. G. Rinaldo, W. Lee, J. Stumper, and M. Eikerling, "Nonmonotonic dynamics in Lifshitz-Slyozov-Wagner theory: Ostwald ripening in nanoparticle catalysts," *Physical Review E*, vol. 86, p. 041601, oct 2012.

[53] K. J. J. Mayrhofer, J. C. Meier, S. J. Ashton, G. K. H. Wiberg, F. Kraus, M. Hanzlik, and M. Arenz, "Fuel cell catalyst degradation on the nanoscale," *Electrochem Comm*, vol. 10, no. 8, pp. 1144–1147, 2008.

[54] Y. Sugawara, A. P. Yadav, A. Nishikata, and T. Tsuru, "Dissolution and surface area loss of platinum nanoparticles under potential cycling," *J Electroanal Chem*, vol. 662, no. 2, pp. 379–383, 2011.

[55] R. K. Ahluwalia, S. Arisetty, X. Wang, X. Wang, R. Subbaraman, S. C. Ball, S. DeCrane, and D. J. Myers, "Thermodynamics and kinetics of platinum dissolution from carbon-supported electrocatalysts in aqueous media under potentiostatic and potentiodynamic conditions," *J Electrochem Soc*, vol. 160, no. 4, pp. F447–F455, 2013.

[56] Y. Onochi, M. Nakamura, and N. Hoshi, "Atomic force microscopy of the dissolution of cubic and tetrahedral Pt nanoparticles in electrochemical environments," *J Phys Chem C*, vol. 116, no. 28, pp. 15134–15140, 2012.

[57] H. Yano, M. Watanabe, A. Iiyama, and H. Uchida, "Particle-size effect of Pt cathode catalysts on durability in fuel cells," *Nano Energy*, vol. 29, pp. 323–333, 2016.

[58] S. Mukerjee, "Particle size and structural effects in platinum electrocatalysis," *J Appl Electrochem*, vol. 20, no. 4, pp. 537–548, 1990.

[59] A. V. Virkar and Y. Zhou, "Mechanism of catalyst degradation in proton exchange membrane fuel cells," *J Electrochem Soc*, vol. 154, no. 6, pp. B540–B547, 2007.

[60] J. C. Meier, I. Katsounaros, C. Galeano, H. J. Bongard, A. A. Topalov, A. Kostka, A. Karschin, F. Schüth, and K. J. J. Mayrhofer, "Stability investigations of electrocatalysts on the nanoscale," *Energ Environ Sci*, vol. 5, no. 11, p. 9319, 2012.

[61] P. J. Ferreira, G. J. la O', Y. Shao-Horn, D. Morgan, R. Makharia, S. Kocha, and H. A. Gasteiger, "Instability of Pt/C electrocatalysts in proton exchange membrane fuel cells," *J Electrochem Soc*, vol. 152, no. 11, p. A2256, 2005.

[62] L. Kim, C. G. Chung, Y. W. Sung, and J. S. Chung, "Dissolution and migration of platinum after long-term operation of a polymer electrolyte fuel cell under various conditions," *J Power Sources*, vol. 183, no. 2, pp. 524–532, 2008.

[63] S. G. Rinaldo, J. Stumper, and M. Eikerling, "Physical theory of platinum nanoparticle dissolution in polymer electrolyte fuel cells," *J Phys Chem C*, no. 114, pp. 5773–5785, 2010.

[64] S. G. Rinaldo, W. Lee, J. Stumper, and M. Eikerling, "Model- and theory-based evaluation of Pt dissolution for supported Pt nanoparticle distributions under potential cycling," *Electrochem Solid St*, vol. 14, no. 5, pp. B47–B49, 2011.

[65] S. G. Rinaldo, W. Lee, J. Stumper, and M. Eikerling, "Catalyst degradation: Nanoparticle population dynamics and kinetic processes," *ECS Transactions*, vol. 50, no. 2, pp. 1505–1513, 2013.

[66] S. G. Rinaldo, P. Urchaga, J. Hu, W. Lee, J. Stumper, C. Rice, and M. Eikerling, "Theoretical analysis of electrochemical surface-area loss in supported nanoparticle catalysts.," *Physical chemistry chemical physics : PCCP*, vol. 16, no. 48, pp. 26876–86, 2014.

[67] L. Tang, X. Li, and R. C. Cammarata, "Electrochemical stability of elemental metal nanoparticles," *J Am Chem Soc*, no. 132, pp. 11722–11726, 2010.

[68] G. Jerkiewicz, G. Vatankhah, J. Lessard, M. P. Soriaga, and Y.-S. Park, "Surface-oxide growth at platinum electrodes in aqueous H2SO4," *Electrochimica Acta*, vol. 49, pp. 1451–1459, apr 2004.

[69] A. Sun, J. Franc, and D. D. Macdonald, "Growth and properties of oxide films on platinum," *Journal Of The Electrochemical Society*, vol. 153, no. 7, pp. B260–B277, 2006.

[70] S. Schuldiner and R. M. Roe, "Transition from hydrogen ionization to oxygen evolution on a platinum electrode," *Journal of The Electrochemical Society*, vol. 110, no. 4, pp. 332–338, 1963.

[71] B. E. Conway and T. C. Liu, "Characterization of electrocatalysis in the oxygen evolution reaction at platinum by evaluation of behavior of surface intermediate states at the oxide film," *Langmuir*, vol. 6, no. 1, pp. 268–276, 1990.

[72] P. P. Lopes, D. Strmcnik, D. Tripkovic, J. G. Connell, V. Stamenkovic, and N. M. Markovic, "Relationships between Atomic Level Surface Structure and Stability/Activity of Platinum Surface Atoms in Aqueous Environments," *ACS Catalysis*, vol. 6, no. 4, pp. 2536–2544, 2016.

[73] P. P. Lopes, D. Tripkovic, P. F. Martins, D. Strmcnik, E. A. Ticianelli, V. R. Stamenkovic, and N. M. Markovic, "Dynamics of electrochemical Pt dissolution at atomic and molecular levels," *Journal of Electroanalytical Chemistry*, vol. 819, no. July 2017, pp. 123–129, 2018.

[74] L. Su, W. Jia, C.-m. Li, and Y. Lei, "Mechanisms for Enhanced Performance of Platinum-Based Electrocatalysts in Proton Exchange Membrane Fuel Cells," *ChemSusChem*, pp. 361–378, 2014.

[75] R. Jinnouchi, K. Kodama, T. Suzuki, and Y. Morimoto, "Kinetically induced irreversibility in electro-oxidation and reduction of Pt surface," *Journal of Chemical Physics*, vol. 142, no. 18, 2015.

[76] N. Cabrera and N. F. Mott, "Theory of the oxidation of metals," *Reports on progress in physics*, vol. 12, pp. 163–184, 1949.

[77] B. E. Conway, "Electrochemical oxide film formation at noble metals as a surface-chemical process," *Progress in Surface Science*, vol. 49, no. 4, pp. 331–452, 1995.

[78] K. Leistner, C. Toulemonde, B. Diawara, a. Seyeux, and P. Marcus, "Oxide film growth kinetics on metals and alloys: II. Numerical simulation of transient behavior," *Journal of the Electrochemical Society*, vol. 160, pp. C197–C205, mar 2013.

[79] D. D. Macdonald and S. I. Smedley, "An electrochemical impedance analysis of passive films on nickle(111) in phosphate buffer solutions," *Electrochimica Acta*, vol. 35, no. 11/12, pp. 1949–1956, 1990.

[80] N. B. Pilling and R. E. Bedworth, "The oxidation of metals at high tempertures," *Journal of the Institute of Metals*, vol. 29, pp. 529–582, 1923.

[81] A. Seyeux, V. Maurice, and P. Marcus, "Oxide film growth kinetics on metals and alloys: I. Physical model," *Journal of the Electrochemical Society*, vol. 160, pp. C189–C196, mar 2013.

[82] N. F. Mott, "The theory of the formation of protective oxide films on metals-III," *Trans. Faraday Soc.*, vol. 43, pp. 429–434, 1947.

[83] M. Shibata, "Conductance measurement of thin oxide films on a platinum anode," *Electrochimica Acta*, vol. 22, no. 2, pp. 175–179, 1977.

[84] D. Landolt, *Corrosion and Surface Chemistry of Metals*. CRC Press, 2007.

[85] J. C. Meyer, C. O. Girit, M. F. Crommie, and A. Zettl, "Imaging and dynamics of light atoms and molecules on graphene," *Nature*, vol. 454, no. July, pp. 319–322, 2008.

[86] S. W. Feldberg, C. G. Enke, and C. E. Bricker, "Formation and dissolution of platinum oxide Film: Mechanism and kinetics," *Journal of The Electrochemical Society*, vol. 110, no. 7, pp. 826–834, 1963.

[87] K. J. Vetter and J. W. Schulze, "The kinetics of the electrochemical formation and reduction of monomolecular oxide layers on platinum in 0.5M H_2SO_4 Part I: Potentiostatic pulse measurements," *Journal of Electroanalytical Chemistry and Interfacial Electrochemistry*, vol. 34, pp. 131–139, 1972.

[88] K. J. Vetter and J. W. Schulze, "The kinetics of the electrochemical formation and reduction of monomolecular oxide layers on platinum in 0.5M H_2SO_4 Part II: Galvanostatic pulse measurements and the model of oxide growth," *Journal of Electroanalytical Chemistry and Interfacial Electrochemistry*, vol. 34, pp. 141–158, 1972.

[89] K. Sasaki, N. Marinkovic, H. S. Isaacs, and R. R. Adzic, "Synchrotron-based in situ characterization of carbon-supported platinum and platinum monolayer electrocatalysts," *ACS Catalysis*, vol. 6, pp. 69–76, 2016.

[90] H. Angerstein-Kozlowska, B. E. Conway, and W. B. A. Sharp, "The real condition of oxidized pt electrodes: Part iii. kinetic theory of formation and reduction of surface oxides," *Journal of Electroanalytical Chemistry*, vol. 43, no. 9, 1973.

[91] B. E. Conway, B. Barnett, H. Angerstein-Kozlowska, and B. V. Tilak, "A surface-electrochemical basis for the direct logarithmic growth law for initial stages of extension of anodic oxide films formed at noble metals," *The Journal of Chemical Physics*, vol. 93, no. 11, pp. 8361–8373, 1990.

[92] M. W. Breiter, "Reduction mechanism of chemisorbed oxygen on platinum electrodes by molecular hydrogen," *Journal of The Electrochemical Society*, vol. 109, p. 425, 1962.

[93] J. Drnec, M. Ruge, F. Reikowski, B. Rahn, F. Carla, R. Felici, J. Stettner, O. M. Magnussen, and D. A. Harrington, "Initial stages of Pt(111) electrooxidation: dynamic and structural studies by surface X-ray diffraction," *Electrochimica Acta*, vol. 224, pp. 220–227, 2017.

[94] M. Ruge, J. Drnec, B. Rahn, F. Reikowski, D. A. Harrington, F. Carla, R. Felici, J. Stettner, and O. M. Magnussen, "Structural reorganization of Pt(111) electrodes by electrochemical oxidation and reduction," *Journal of the American Chemical Society*, vol. 139, no. 12, pp. 4532–4539, 2017.

[95] S. Tahmasebi, A. A. McMath, J. van Drunen, and G. Jerkiewicz, "Catalytic duality of platinum surface oxides in the oxygen reduction and hydrogen oxidation reactions," *Electrocatalysis*, vol. 8, no. 4, pp. 301–310, 2017.

[96] V. I. Birss, M. Chang, and J. Segal, "Platinum oxide film formation - reduction: an in-situ mass measurement study," *Journal of Electroanalytical Chemistry*, vol. 355, pp. 181–191, 1993.

[97] B. E. Conway, G. Tremiliosi-Filho, and G. Jerkiewicz, "Independence of formation and reduction of monolayer surface oxide on Pt from presence of thicker phase-oxide layers," *Journal of Electroanalytical Chemistry*, vol. 297, pp. 435–443, 1991.

[98] A. M. Gómez-Marín and J. M. Feliu, "Pt(111) surface disorder kinetics in perchloric acid solutions and the influence of specific anion adsorption," *Electrochimica Acta*, vol. 82, pp. 558–569, Nov. 2012.

[99] D. Gilroy and B. E. Conway, "Surface oxidation and reduction of platinum electrodes: Coverage, kinetic and hysteresis studies," *Canadian Journal of Chemistry*, vol. 46, no. 6, pp. 875–890, 1968.

[100] J. J. Scholz and M. A. Langell, "Kinetic analysis of surface reduction in transition metal oxide single crystals," *Surface Science*, vol. 164, no. 2-3, pp. 543–557, 1985.

[101] D. Talapin, A. L. Rogach, M. Haase, and H. Weller, "Evolution of an ensemble of nanoparticles in a colloidal solution: Theoretical study," *Journal of Physical Chemistry B*, vol. 105, no. 49, pp. 12278–12285, 2001.

[102] S. Cherevko, G. P. Keeley, S. Geiger, A. R. Zeradjanin, N. Hodnik, N. Kulyk, and K. J. Mayrhofer, "Dissolution of platinum in the operational range of fuel cells," *ChemElectroChem*, vol. 2, no. 10, pp. 1471–1478, 2015.

[103] K. Yasuda, A. Taniguchi, T. Akita, T. Ioroi, and Z. Siroma, "Platinum dissolution and deposition in the polymer electrolyte membrane of a PEM fuel cell as studied by potential cycling.," *Phys Chem Chem Phys*, vol. 8, no. 6, pp. 746–752, 2006.

[104] D. Fantauzzi, J. E. Mueller, L. Sabo, A. C. T. Van Duin, and T. Jacob, "Surface buckling and subsurface oxygen: Atomistic insights into the surface oxidation of Pt(111)," *ChemPhysChem*, vol. 16, pp. 2797–2802, 2015.

[105] M. J. Eslamibidgoli and M. H. Eikerling, "Atomistic mechanism of pt extraction at oxidized surfaces: Insights from dft," *Electrocatalysis*, vol. 7, pp. 345–354, 2016.

[106] E. F. Holby, J. Greeley, and D. Morgan, "Thermodynamics and hysteresis of oxide formation and removal on platinum (111) surfaces," *The Journal of Physical Chemistry C*, vol. 116, pp. 9942–9946, May 2012.

[107] H. A. Baroody, G. Jerkiewicz, and M. H. Eikerling, "Modelling oxide formation and growth on platinum," *Journal of Chemical Physics*, vol. 146, p. 144102, 2017.

[108] G. Tremiliosi-Filho, G. Jerkiewicz, and B. E. Conway, "Characterization and significance of the sequence of stages of oxide film formation at platinum generated by strong anodic polarization," *Langmuir*, no. 8, pp. 658–667, 1992.

[109] T. M. Pedersen, W. Xue Li, and B. Hammer, "Structure and activity of oxidized Pt(110) and alpha-PtO2.," *Physical chemistry chemical physics : PCCP*, vol. 8, no. 110, pp. 1566–1574, 2006.

[110] J. R. Mcbride, G. W. Graham, C. R. Peters, and W. H. Weber, "Growth and characterization platinum oxides of reactively sputtered thin-film," *Journal of Applied Physics*, vol. 69, pp. 1596–1604, 1991.

[111] D. Fantauzzi, J. Bandlow, L. Sabo, J. E. Mueller, A. C. T. van Duin, and T. Jacob, "Development of a ReaxFF potential for Pt-O systems describing the energetics and dynamics of Pt-oxide formation.," *Physical chemistry chemical physics : PCCP*, vol. 16, no. 111, pp. 23118–33, 2014.

[112] N. Seriani, Z. Jin, W. Pompe, and L. Ciacchi, "Density functional theory study of platinum oxides: From infinite crystals to nanoscopic particles," *Physical Review B*, vol. 76, p. 155421, oct 2007.

[113] B. E. Conway and S. Gottesfeld, "Real condition of oxidized platinum electrodes: Part II. Resolution of reversible and irreversible processes by optical and impedence studies," *J. Chem. Soc. Farad T 1*, vol. 69, no. 0, p. 1090, 1972.

[114] G. Qile, *Platinum oxide reduction kinetics on polycrystalline platinum electrodes by platinum oxide reduction kinetics on polycrystalline Platinum Electrodes*. PhD thesis, University of Victoria, 2016.

[115] M. Alsabet, M. Grden, and G. Jerkiewicz, "Comprehensive study of the growth of thin oxide layers on Pt electrodes under well-defined temperature, potential, and time conditions," *Journal of Electroanalytical Chemistry*, vol. 589, pp. 120–127, apr 2006.

[116] M. Momeni and J. C. Wren, "A mechanistic model for oxide growth and dissolution during corrosion of Cr-containing alloys," *Faraday Discuss.*, vol. 180, pp. 1–23, 2015.

[117] H. Cohen and J. W. Cooley, "The Numerical Solution of the time-dependent nernst-planck equation," *Biophysical Journal*, vol. 5, pp. 145–162, 1965.

[118] S. P. Devarajan, J. A. Hinojosa, and J. F. Weaver, "STM study of high-coverage structures of atomic oxygen on Pt(111): p(2x1) and Pt oxide chain structures," *Surface Science*, vol. 602, pp. 3116–3124, Oct. 2008.

[119] J. O. Bockris and Z. Nagy, "Symmetry Factor and Transfer Coefficient," *Journal of Chemical Education*, vol. 50, no. 12, pp. 839–843, 1973.

[120] M. Vankeerberghen, "1D steady-state finite-element modelling of a bi-carrier one-layer oxide film," *Corrosion Science*, vol. 48, no. 11, pp. 3609–3628, 2006.

[121] T. L. Cheng, Y. H. Wen, and J. A. Hawk, "Diffuse-interface modeling and multiscale-relay simulation of metal oxidation kinetics with revisit on Wagner's theory," *The Journal of Physical Chemistry*, vol. 118, pp. 1269–1284, 2014.

[122] G. Jerkiewicz and J. J. Borodzinski, "Studies of Formation of Very Thin Oxide Films on Polycrystalline Rhodium Electrodes : Application of the Mott-Cabrera Theory," *Langmuir*, no. 23, pp. 2202–2209, 1993.

[123] C. Y. Chao, L. F. Lin, and D. D. Macdonald, "A point defect model for anodic passive films I. Growth kinetics," *Journal of The Electrochemical Society*, vol. 128, no. 6, 1981.

[124] A. T. Fromhold, *Theory of metal oxidation volume 1 - Fundamentals*, vol. 9 of *Defects in Crystalline Solids*. North-Holland Publishing Company, 1976.

[125] T. R. Brumleve and R. P. Buck, "Numerical solution of the Nernst-Planck and poisson equation system with applications to membrane electrochemistry and solid state physics," *Journal of Electroanalytical Chemistry*, vol. 90, no. 1, pp. 1–31, 1978.

[126] T. Sokalski, P. Lingelfelter, and A. Lewenstam, "Numerical solution of the coupled Nernst-Planck and Poisson equations for liquid junction and ion selective membrane potentials," *Journal of Physical Chemistry B*, vol. 107, no. 11, pp. 2443–2452, 2003.

Appendix A

Supporting Information

		start points						Optimized points					
ϕ_{UPL} $\mathrm{V_{RHE}}$	γ_{Pt} J $\mathrm{m^{-2}}$	log $k_{\mathrm{dis}}C^{\mathrm{ref}}$ mol $\mathrm{m^{-2}s^{-1}}$	log k_{rdp} m $\mathrm{s^{-1}}$	log k_{cgl} $\mathrm{s^{-1}}$	log k_{det} $\mathrm{s^{-1}}$	log k_{pitm} $\mathrm{m^3\ s^{-1}}$	goodness of fit	log k_{dis} mol $\mathrm{m^{-2}s^{-1}}$	log k_{rdp} $\mathrm{m^{-2}\ s^{-1}}$	log k_{cgl} $\mathrm{s^{-1}}$	log k_{det} $\mathrm{s^{-1}}$	log k_{pitm} $\mathrm{m^3\ s^{-1}}$	goodness of fit
1.0	2.27	-9.31	-10.3	6.18	-4.67	-35.0	$3.06\text{x}10^{-2}$	-8.79	-11.7	6.16	-	-36.0	$7.90\text{x}10^{-3}$
1.1	1.13	-8.16	-13.2	6.18	-8.34	-35.6	$5.45\text{x}10^{-2}$	-7.99	-10.2	6.01	-	-36.1	$3.19\text{x}10^{-2}$
1.2	0.50	-8.31	-13.1	6.29	-4.55	-25.7	$6.03\text{x}10^{-2}$	-7.33	-9.64	6.06	-9.00	-36.1	$1.65\text{x}10^{-2}$
1.2*	0.48	-8.42	-12.8	6.15	-4.73	-28.8	$8.69\text{x}10^{-2}$	-7.26	-9.50	6.20	-8.99	-35.9	$3.63\text{x}10^{-2}$
1.3	0.47	-8.32	-8.93	6.70	-3.57	-26.8	$5.57\text{x}10^{-2}$	-8.03	-12.4	6.56	-3.81	-27.4	$4.01\text{x}10^{-2}$

Table A.1: Comparison of start values obtained at STAGE I vs. optimized values after STAGE II for Low Surface Area Carbon (LSAC) that correlates to Figure 3.3. [*] indicates parameters of extended experimental data set shown in Figure 3.4.

ϕ_{UPL} V_{RHE}	γ_{Pt} J m^{-2}	start points log $k_{dis}C^{ref}$ mol $m^{-2}s^{-1}$	log k_{rdp} m s^{-1}	log k_{cgl} s^{-1}	log k_{det} s^{-1}	log k_{pitm} m^3 s^{-1}	goodness of fit	Optimized points log k_{dis} mol $m^{-2}s^{-1}$	log k_{rdp} m^{-2} s^{-1}	log k_{cgl} s^{-1}	log k_{det} s^{-1}	log k_{pitm} m^3 s^{-1}	goodness of fit
0.9*	4.57	-9.85	-12.0	-	-	-	-	-11.2	-12.0	-	-	-	$8.13x10^{-5}$
0.9	2.62	-9.97	-5.67	3.12	-4.47	-32.7	$2.90x10^{-2}$	-9.85	-6.01	-	-	-32.7	$2.71x10^{-2}$
1.0	2.62	-9.12	-7.07	3.04	-6.36	-34.4	$1.79x10^{-2}$	-9.12	-12.0	-	-	-34.4	$1.11x10^{-2}$
1.1	2.23	-9.01	-12.8	4.15	-6.77	-35.9	$4.78x10^{-2}$	-8.90	-10.1	-	-	-36.4	$7.75x10^{-3}$
1.2	0.99	-8.75	-14.0	6.54	-5.19	-32.0	$2.90x10^{-2}$	-8.00	-9.92	6.20	-4.76	-36.1	$6.15x10^{-3}$
1.3	0.51	-8.12	-13.3	6.78	-3.56	-27.9	$1.45x10^{-2}$	-7.94	-14.0	6.88	-3.61	-35.5	$1.00x10^{-2}$

Table A.2: Comparison of start values obtained in STAGE I vs. optimized values after STAGE II for Medium Surface Area Carbon (MSAC) that correlates to Figure 3.6. [*] is the model results only including the dissolution/redeposition mechanism.

		start points						Optimized points					
ϕ_{UPL} $\mathrm{V_{RHE}}$	γ_{Pt} J $\mathrm{m^{-2}}$	log $k_{\mathrm{dis}}C^{\mathrm{ref}}$ mol $\mathrm{m^{-2}s^{-1}}$	log k_{rdp} m $\mathrm{s^{-1}}$	log k_{cgl} $\mathrm{s^{-1}}$	log k_{det} $\mathrm{s^{-1}}$	log k_{pitm} $\mathrm{m^3\ s^{-1}}$	goodness of fit	log k_{dis} mol $\mathrm{m^{-2}s^{-1}}$	log k_{rdp} $\mathrm{m^{-2}\ s^{-1}}$	log k_{cgl} $\mathrm{s^{-1}}$	log k_{det} $\mathrm{s^{-1}}$	log k_{pitm} $\mathrm{m^3\ s^{-1}}$	goodness of fit
1.2	0.20	-7.999	-13.1	6.9	-5.03	-29.4	$1.31\text{x}10^{-1}$	-7.84	-6.25	7.31	-4.04	-31.4	$1.12\text{x}10^{-2}$

Table A.3: Comparison of start values obtained in STAGE I vs. optimized values after STAGE II for High Surface Area Carbon (HSAC) that correlates to Figure 3.8.

Appendix B

Platinum Degradation Code for Chapter 3

B.1 The Monte Carlo Simulation for STAGE I

```
% Monte Carlo MATLAB Code for Stage I for Chapter 3
% function degradation_main_pitm

%% Load experimental data
% for example: MSAC data
load USDOE_13M_data.mat
run = 'MSAC 1.3V';
file = 'MSAC_13V-1';


%% load parameters
p=degradation_parameters_pitm;

%% integrator options
tspan = data.cycle;
options=odeset('Stats','on', 'RelTol',1e-3,'AbsTol',1e-5);

%% Monte Carlo Simulation

LB = [1E-9 -15 -15 3 -6 -34];
UB = [4E-9 -5 -5 9 -3 -29];
nsim = 50; %number of simulations
r = zeros(nsim,6);
error = zeros(nsim,1);
```

```
25
26 for i = 1:nsim
27     r(i,:) = rand(1,6).*(UB-LB)+LB;
28 p.R0 = r(i,1);
29 p.k_dis = 10^r(i,2);
30 p.k_rdp = 10^r(i,3);
31 p.k_cgl = 10^r(i,4);
32 p.k_det = 10^r(i,5);
33 p.k_pitm = 10^r(i,6);
34
35 %% call integrator
36 [t,x,te]=ode15s_limit(@degradation_pitm,tspan,p.x0,options,p)
       ;
37
38 %% post processing
39 %% split the state vector
40 f    = x(:,1:p.n);
41 c_Pt = x(:,p.n+1);
42 pitm = x(:,p.n+2);
43
44  if nsteps == 12500
45      error(i) = 1E99;
46  elseif sum(sum(f<0)) <= 0
47
48 %% calculation of the moments
49
50 for lv=1:length(t)
51 PN(lv)   = trapz(p.r_m, f(lv,:))/p.PN_0;
52 rN(lv)   = trapz(p.r_m, p.r_m'.*f(lv,:))*p.PN_0/(trapz(p.r_m,
       f(lv,:))*p.rN_0);
53 SN(lv)   = trapz(p.r_m, p.r_squared'.*f(lv,:))/p.SN_0;
54 MN(lv)   = trapz(p.r_m, p.r_cubed'.*f(lv,:))/p.MN_0;
55 h=degradation_help_pitm(t,f(lv,:)',p);
56 J_p(lv,:) = h.J_p;
57 J_m(lv,:) = h.J_m;
58 r_mean(lv)   = trapz(p.r_m, p.r_m'.*f(lv,1:p.n))/(trapz(p.r_m
       ,f(lv,1:p.n)));
59 end
60
61 MN_detach = 1-MN'-c_Pt/p.m_V__M_Pt;
62
63 %% error calculation
64 w_epsa = 1/length(data.ECSA);
65 scale_epsa = 1;
```

```
w_rad = 1/length(data.r_mean);
scale_rad = data.r_mean(1);
w_pitm = 1/length(data.pitm);
scale_pitm = 1;
w_thick = 0.5;
scale_thick = 1;

error(i) = sum(((SN' - data.ECSA)./scale_epsa).^2)...
        + sum(((r_mean(end)' - data.r_mean(end))./scale_rad)
            .^2)...
        + sum(((pitm(end)-data.pitm(end))./scale_pitm).^2)...
        + w_thick*sum(((MN_detach(end)-data.EOT_thick)./
            scale_thick).^2);
else
    error(i) = 1E99;
 end
 end

FID = fopen([datestr(now,'yymmddHHMM'),'MC_results_full_',
    file,'.csv'],'w');
ii = find(error~=1E99);
for i = 1:length(ii)
    fprintf(FID,'%i, %f, %f, %f, %f, %f, %f, %f\n',[ii(i); r(
        ii(i),1)*1e9; r(ii(i),2:end)'; error(ii(i))]);
end
fclose(FID);

save([datestr(now,'yymmddHHMM'),'full_mc_results_nocgl_',
    file,'.mat']);

%% Plot Results: All Fits
figure
subplot(2,2,1)
hold on
plot(t,SN, 'color', [0.42,0.25,0.39],'linewidth', 1.5);
plot(data.cycle,data.ECSA, 'o','color',[0,0.45,0.74],'
    linewidth', 1.5);
xlabel({'cycles'},'FontSize',15)
ylabel({'ECSA'},'FontSize',15)
title(error,'FontSize',20)

subplot(2,2,2)
hold on
plot(t, r_mean, 'color', [0.42,0.25,0.39],'linewidth', 1.5);
```

```
plot(data.cycle,data.r_mean, 'o','color',[0,0.45,0.74],'
    linewidth', 1.5);
xlabel({'cycles'},'FontSize',15)
ylabel({'mean radius'},'FontSize',15)

subplot(2,2,3)
hold on
plot(t, pitm, 'color', [0.42,0.25,0.39],'linewidth', 1.5);
plot(data.cycle,data.pitm, 'o','color',[0,0.45,0.74],'
    linewidth', 1.5);
xlabel({'cycles'},'FontSize',15)
ylabel({'PITM'},'FontSize',15)

subplot(2,2,4)
hold on
plot(t,MN_detach, 'color', [0.42,0.25,0.39],'linewidth', 1.5)
    ;
plot(data.cycle(end),data.EOT_thick, 'o','color'
    ,[0,0.45,0.74],'linewidth', 1.5);
xlabel({'cycles'},'FontSize',15)
ylabel({'thickness'},'FontSize',15)
```

B.2 The Optimization Routine for STAGE II

```
% Optimization MATLAB Code for Stage II for Chapter 3
% function degradation_main_pitm

%% Load experimental data
% for example: MSAC data
load USDOE_12M_data.mat
source = '1.2 V MSAC - full';
file = 'M12-full';

%%% parameter optimization
tic
p=degradation_parameters_pitm;

%% set start point

p.p0_log = [p.k_dis_log p.k_rdp_log p.k_cgl_log p.k_det_log p
    .k_pitm_log];

LB = [-20 -20 0 -10 -37];
```

```
19 UB = [-10  -10  7  -03  -26];
20
21 options_ps = psoptimset('Display','iter','PlotFcn',
       @psplotbestf);
22 format short e;
23 [pfit,fval,exitflag] = patternsearch(@(fp)
       errorfunction_pitm_conpos(fp,data,p),p.p0_log,[],[],[],[],
       LB,UB,[],options_ps);
24
25
26 computingtime=toc;
27
28 p.k_dis = 10^pfit(1);
29 p.k_rdp = 10^pfit(2);
30 p.k_cgl = 10^pfit(3);
31 p.k_det = 10^pfit(4);
32 p.k_pitm = 10^pfit(5);
33
34 %%%% calculation of model results for given parameters
       %%%%%
35 %% integrator options %%%%%%%%%%%%%%%%%%%%%%%%%%%%%%%%%%%%%%%%
36 tspan=data.cycle;
37 % integrator options
38 options_ODE=odeset('Stats','on', 'RelTol',1e-3,'AbsTol',1e-5)
       ;
39
40 %%% call integrator
       %%%%%%%%%%%%%%%%%%%%%%%%%%%%%%%%%%%%%%%%%%%%%%%%
41 % profile on; profile clear;
42 [t,x]=ode15s(@degradation_pitm,tspan,p.x0,options_ODE,p);
43 % profile report;
44
45 %%% post processing
       %%%%%%%%%%%%%%%%%%%%%%%%%%%%%%%%%%%%%%%%%%%%%%%%
46 %% split the state vector
47 f    = x(:,1:p.n);
48 c_Pt = x(:,p.n+1);
49 pitm = x(:,p.n+2);
50
51 for lv=1:length(t)
52 PN(lv)   = trapz(p.r_m, f(lv,:))/p.PN_0;    % Eq. 2.8
       denominator
53 rN(lv)   = trapz(p.r_m, p.r_m'.*f(lv,:))*p.PN_0/(trapz(p.r_m,
       f(lv,:))*p.rN_0);    % Eq. 2.9
```

```
54 SN(lv)    = trapz(p.r_m, p.r_squared'.*f(lv,:))/p.SN_0;    % Eq
       . 2.10
55 MN(lv)    = trapz(p.r_m, p.r_cubed'.*f(lv,:))/p.MN_0;    % Eq.
       2.11
56 h=degradation_help_pitm(t,f(lv,:)',p);
57 %c_Pt(lv) = h.c_Pt;
58 J_p(lv,:) = h.J_p;
59 J_m(lv,:) = h.J_m;
60 old_c_Pt(lv) = p.m_V__M_Pt*(1-MN(lv));
61 r_mean(lv)    = trapz(p.r_m, p.r_m'.*f(lv,1:p.n))/(trapz(p.r_m
       ,f(lv,1:p.n)));
62 end
63 MN_detach = 1-MN'-pitm-c_Pt/p.m_V__M_Pt;
64
65 %% final error calculation
66 w_epsa = 1/length(data.ECSA);
67 scale_epsa = 1;
68 w_rad = 1/length(data.r_mean);
69 scale_rad = data.r_mean(1);
70 w_pitm = 1/length(data.pitm);
71 scale_pitm = 1;
72 w_thick = 0.5;
73 scale_thick = 1;
74
75 error = w_epsa*sum(((SN' - data.ECSA)./scale_epsa).^2)...
76         + sum(((r_mean(end)' - data.r_mean(end))./scale_rad)
               .^2)...
77         + sum(((pitm(end)-data.pitm(end))./scale_pitm).^2)...
78         + w_thick*sum(((MN_detach(end)-data.EOT_thick)./
               scale_thick).^2);
79
80
81 save([datestr(now,'yymmddHHMM'),file,'
       fullmodel_pitm_fitresults.mat']);
82
83
84 %% Results All fits
85 figure
86 subplot(2,2,1)
87 hold on
88 plot(t,SN, 'color', [0.42,0.25,0.39],'linewidth', 1.5);
89 plot(data.cycle,data.ECSA, 'o','color',[0,0.45,0.74],'
       linewidth', 1.5);
90 xlabel({'cycles'},'FontSize',15)
```

```
ylabel({'ECSA'},'FontSize',15)
title(error,'FontSize',20)

subplot(2,2,2)
hold on
plot(t, r_mean, 'color', [0.42,0.25,0.39],'linewidth', 1.5);
plot(data.cycle(end),data.r_mean(end), 'o','color'
    ,[0,0.45,0.74],'linewidth', 1.5);
xlabel({'cycles'},'FontSize',15)
ylabel({'mean radius'},'FontSize',15)

subplot(2,2,3)
hold on
plot(t, pitm, 'color', [0.42,0.25,0.39],'linewidth', 1.5);
plot(data.cycle(end),data.pitm(end), 'o','color'
    ,[0,0.45,0.74],'linewidth', 1.5);
xlabel({'cycles'},'FontSize',15)
ylabel({'% PITM'},'FontSize',15)

subplot(2,2,4)
hold on
plot(t,MN_detach, 'color', [0.42,0.25,0.39],'linewidth', 1.5)
    ;
plot(data.cycle(end),data.EOT_thick(end), 'o','color'
    ,[0,0.45,0.74],'linewidth', 1.5);
xlabel({'cycles'},'FontSize',15)
ylabel({'% thickness reduction'},'FontSize',15)
savefig([datestr(now,'yymmddHHMM'),file,'subplot.fig'])
```

B.3 Files

B.3.1 degradation_pitm.m

```
function dxdt=degradation_pitm(t,x,p)

%% split the state vector
f = x(1:p.n);
c = x(p.n+1);
%pitm = x(p.n+2);

%% calculate help variables

h = degradation_help_pitm(t,x,p);
```

```
11
12 %% time derivatives
13 % full model
14 drdt = p.Vm_Pt*p.k_rdp.*c.*exp(-p.R0./p.r_m) - p.Vm_Pt*p.
       k_dis.*exp(p.R0./p.r_m);
15 dfdt = - gradient( f.*drdt,p.dr)+ h.J_p - h.J_m- p.k_det*f;
16 dmdt = 4*pi*p.rho_Pt*p.r_m.^2.*drdt;
17 dMdt = trapz(p.r_m, f.*dmdt);
18 dcdt = p.I_V*p.m_V__M_Pt*(-dMdt-(p.k_pitm.*c.*p.M_Pt))/p.M_0;
19 dpitmdt = (p.k_pitm*c*p.M_Pt)/p.M_0;
20 %% output vector
21 dxdt = [dfdt; dcdt; dpitmdt];
```

B.3.2 degradation_help_pitm.m

```
1  function h=degradation_help_pitm(t,x,p)
2
3  %% split the state vector
4  f = x(1:p.n);
5  %c = x(p.n+1);
6
7  %% numerically integrated
8  h.J_m = p.k_cgl*f.*trapz(p.r_m,f);
9
10 %% numerically integrated using rectangular approximation, i.
       e. in
11 %% the intervall r0...r1
12
13 % pre-allocation for faster running time
14 J_p = zeros(p.n,1);
15
16 for lv=2:p.n  % loop over all radii
17
18   rng=1:(lv-1);      % for r~ = r the integrand would become
       infinity ( r^3-r~^3)->infinity for r~->r
19                      % Fix: last element is omitted.
20   r_1 = (p.r_cubed(lv)-p.r_cubed(rng)).^(1/3);  % radius of
       the second merging particle
21
22   J_p(lv,1) =  p.k_cgl/2*p.dr*sum(p.r_squared(lv)./((p.
       r_cubed(lv)-p.r_cubed(rng)).^(2/3)).*interp1q(p.r_m,f,
       r_1).*f(rng));
23
24 end
```

```
h.J_p = J_p;
```

B.3.3 degradation_parameters_pitm.m

```
function p=degradation_parameters_pitm

%% physical and chemical constants %%%%%%%%%%%%%%%%%%%%%%%%%%%%%%%%%%%%%%%%
p.Vm_Pt = 9.09e-6;      % [m3/mol]
p.M_Pt  = 195.0849;     % [g/mol]
M_Pt  = 195.0849;     % [g/mol]
p.rho_Pt = 21450000; %[g/m3]
%% geometry %%%%%%%%%%%%%%%%%%%%%%%%%%%%%%%%%%%%%%%%%%%%%%%%%%%%%%%%%%%%%%%

%% Finite Volume Method with equidistant elements
p.r_max = 30.1e-9;                          % [m] maximum radius of PRD

p.n = 301;                                 % number of elements of FVM

p.dr = p.r_max/p.n;                        % [m] length of elements, equidistant
p.r = linspace(1e-10,p.r_max,p.n+1)';     % [m] boundaries of elements
p.r_m = p.r(1:p.n)+p.dr/2;                 % [m] center of elements

p.V   = 4/3*pi*p.r.^3;
p.dV  = p.V(2:end)-p.V(1:end-1);
p.V_m = 4/3*pi*p.r_m.^3;

%% initial conditions %%%%%%%%%%%%%%%%%%%%%%%%%%%%%%%%%%%%%%%%%%%%%%%%%%%%%

% S = 0.314; %LSAC
% M = 0.944; %LSAC
%
S = 0.460; %MSAC
M = 0.612; %MSAC
%
% S = 0.323; %HSAC
% M = 0.478; %HSAC

```

```
33 p.f0 = 1./(S.*sqrt(2.*pi).*p.r_m*1e9).*exp((-(log(p.r_m*1e9)-
       M).^2)./(2.*S.^2));
34 p.f0(1) = 0;
35
36 p.c0 = 0;
37 p.pitm0 = 0;
38
39 p.x0 = [p.f0; p.c0; p.pitm0];
40
41 %% kinetic parameters
42
43 p.R0      = 1.001892e-09;
44 p.k_dis_log  = -8.247704;
45 p.k_rdp_log  = -11.106991;
46 p.k_cgl_log  = 6.365476;
47 p.k_det_log  = -4.285574;
48 p.k_pitm_log = -25.363878;
49
50 p.k_dis  = 10^p.k_dis_log;
51 p.k_rdp  = 10^p.k_rdp_log;
52 p.k_cgl  = 10^p.k_cgl_log;
53 p.k_det  = 10^p.k_det_log;
54 p.k_pitm = 10^p.k_pitm_log;
55
56 p.m_V__M_Pt = 0.33333e6/M_Pt;      % m_V/M_Pt, mass loading /
       molecular weight; prefactor of Eq. 2.5
57 % estimated: thickness of CL=12e-6m, loading 4mg/cm2
58
59 p.r_squared = p.r_m.^2; % [m^2] squares of the radius (center
       of elements)
60 p.r_cubed   = p.r_m.^3; % [m^3] cubes of the radius (center
       of elements)
61 p.MN_0 = trapz(p.r_m, p.r_cubed.*p.f0);
62 p.SN_0 = trapz(p.r_m, p.r_squared.*p.f0);
63 p.rN_0 = trapz(p.r_m, p.r_m.*p.f0);
64 p.PN_0 = trapz(p.r_m, p.f0);
65 p.M_0 = 4/3*pi*p.rho_Pt*p.MN_0;
66 p.I_V = 1; %ionomer volume fraction in the catalyst layer
```

Appendix C

Platinum Oxide Growth and Reduction Code for Chapter 4

C.1 Main

```
%% Reduction Model solution main
% September 2018
%% Parameters
fullOxideModel_parameters;

%% define zero matrix
m=1000; %L/c note: for some unknown reason L/c stop working
    so I enter this manually now
rho = zeros(1,m);
t_a = zeros(1,m);
b = zeros(1,m);

%% Numerical solve for integration constants


for i = 1:L/c

        Lambdaspace = logspace(log10(L),log10(s),L/c);
        %Lambdaspace = linspace(L,s,L/c);

        Lambda1 = Lambdaspace(i);
```

```
21
22      t_a(i) = fzero(@(t_a) soln_to_a(t_a,Lambda1),5); %
            solution to integration constant 'a'
23      b(i) = (k2r+(-k2f-k2r)*(t_a(i)*exp(-Phi)))/((Phi/Lambda1)
            +k2f+k2r); %Eq 48 integration constant 'b'
24      rho(i) = t_a(i)+b(i); %O vacancy concentration at m/o
            interface (xi=0)
25  end
26
27  rho_full = t_a(1,end).*exp(-Phi*Lambdaspace/L)+b(1,end); %Eq
        46 - O at Lambda
28
29  f1f = (0.5*(1+tanh(Gamma.*(1-rho)))); %Eq 36
30  f1r = (0.5*(1+tanh(-Gamma.*(1-rho)))); %Eq 37
31  dLdt = (kappa.*f1f)-(kappar.*f1r);
32  %% integrate
33
34  tau = cumtrapz(Lambdaspace, 1./dLdt);
35
36  time=tau;
37  %% Plots
38
39
40  %% plot oxide layer thickness as a function of time
41
42  figure
43  hold on;
44  %plot(time,Lambdaspace, 'color',[0.42,0.25,0.39], '
        LineWidth', 2);
45  %plot(time,Lambdaspace,'color',[0.64,0.08,0.18], 'LineWidth
        ', 2);
46  %plot(time,Lambdaspace, 'color','k', 'LineWidth', 2);
47  plot(time,Lambdaspace, 'color',[0,0.45,0.74], 'LineWidth',
        2);
48  %plot(time,Lambdaspace, 'color',[0,0.75,0.75], 'LineWidth',
         2);
49
50  set(gca,...
51      'Color'         , [0.97,0.97,0.97],...
52      'Box'           , 'on'      , ...
53      'visible'       , 'on'      , ...
54      'TickDir'       , 'in'      , ...
55      'TickLength'    , [.01 .01] , ...
56      'XMinorTick'    , 'on'      , ...
```

```
    'YMinorTick'   , 'on'        , ...
    'YGrid'        , 'off'       , ...
    'XColor'       , [.3 .3 .3], ...
    'YColor'       , [.3 .3 .3], ...
    'LineWidth'    , 1           , ...
    'fontsize'     , 18);

xlabel({'time (s)'},'FontSize',25)
ylabel({'\lambda'},'FontSize',25)

h=legend('\gamma = 1',...
         '\gamma = 50',...
         '\gamma = 100',...
         '\gamma = 150',...
         '\gamma = 200', 'Location', 'best');

set(h,'Color','w');
```

C.2 Files

C.2.1 soln_to_a.m

```
%% Function to solve a using fzero
% main: fullOxideModel_main.m
% September 2018

function f_a = soln_to_a(t_a, Lambda1)
    fullOxideModel_parameters;

    b = (k2r+(-k2f-k2r)*(t_a*exp(-Phi)))/((Phi/Lambda1)+k2f+
        k2r); %Eq 48
    f_a = 2.*Phi.*b./(Lambda1)-(k1f.*(1+tanh(Gamma.*(1-(t_a+b
        ))))+(k1r.*(1+tanh(-Gamma.*(1-(t_a+b))))); %Eq 47

end
```

C.2.2 fullOxideModel_parameters.m

```

deltaphi = -0.002;
D = 1E-14; %cm^2s^-1 %Diffusion constant
F = 96485; %C mol^-1 Faraday Constant
R = 8.314; %J K^-1 mol^-1 Gas Constant
```

```
T = 353; %K Temperature
Phi =  2*F*deltaphi/(R*T); %non dimensionalize potential
    parameter
L_0 = 2.67E-8; %cm characteristic thickness
k11f = 1E-12; %forward reaction rate across mo interface
k11r = 1E-10; %reverse reaction rate across mo interface
k22f = 1E-8; %forward reaction rate across oe interface
k22r = 1E-8; %reverse reaction rate across oe interface
rho_0 = 0.005; %mol cm^-3 reference concentration
EF = 0.0656; %(0.0789-0.0656) mol cm^-3 expansion factor
alpha = 0.5;
phi_mo = 0.0001; %forward potential across the mo interface
phi_om = 0.0001; %reverse potential across the mo interface
k1f = k11f*L_0/D/rho_0*exp(alpha*F*phi_mo/(R*T)); %Eq 27
k1r = k11r*L_0/D/rho_0*exp(alpha*F*phi_om/(R*T)); %Eq 28
k2f = k22f*L_0/D/rho_0; %Eq 29
k2r = k22r*L_0/D/rho_0; %Eq 30
kappa = k11f*L_0/D/EF;
kappar = k11r*L_0/D/EF;

t_gamma = 100;
Gamma = t_gamma*rho_0;


dt = 1;%713; %dimensionalize time constant
z = 0; %shift
L = 5/dt; %dimensionless length (end point)
c = 0.005/dt; %counts
s = 0.005/dt; %start point
```